CONTROL ALLOCATION FOR A MULTI-ROTOR E-VTOL AIRCRAFT USING BLENDED-INVERSE

A THESIS SUBMITTED TO
THE GRADUATE SCHOOL OF NATURAL AND APPLIED SCIENCES
OF
MIDDLE EAST TECHNICAL UNIVERSITY

BY

EMRE AKSOY

IN PARTIAL FULFILLMENT OF THE REQUIREMENTS
FOR
THE DEGREE OF MASTER OF SCIENCE
IN
AEROSPACE ENGINEERING

FEBRUARY 2021

Approval of the thesis:

CONTROL ALLOCATION FOR A MULTI-ROTOR E-VTOL AIRCRAFT USING BLENDED-INVERSE

submitted by **EMRE AKSOY** in partial fulfillment of the requirements for the degree of **Master of Science in Aerospace Engineering Department, Middle East Technical University** by,

Prof. Dr. Halil Kalıpçılar
Dean, Graduate School of **Natural and Applied Sciences** ________________

Prof. Dr. İsmail Hakkı Tuncer
Head of Department, **Aerospace Engineering** ________________

Assoc. Prof. Dr. İlkay Yavrucuk
Supervisor, **Aerospace Engineering, METU** ________________

Examining Committee Members:

Prof. Dr. Ozan Tekinalp
Aerospace Engineering, METU ________________

Assoc. Prof. Dr. İlkay Yavrucuk
Aerospace Engineering, METU ________________

Prof. Dr. Kemal Leblebicioğlu
Electrical and Electronics Engineering, METU ________________

Prof. Dr. Metin Uymaz Salamcı
Mechanical Engineering, Gazi University ________________

Assist. Prof. Dr. Ali Türker Kutay
Aerospace Engineering, METU ________________

Date:

I hereby declare that all information in this document has been obtained and presented in accordance with academic rules and ethical conduct. I also declare that, as required by these rules and conduct, I have fully cited and referenced all material and results that are not original to this work.

Name, Surname: Emre Aksoy

Signature :

ABSTRACT

CONTROL ALLOCATION FOR A MULTI-ROTOR E-VTOL AIRCRAFT USING BLENDED-INVERSE

Aksoy, Emre
M.S., Department of Aerospace Engineering
Supervisor: Assoc. Prof. Dr. İlkay Yavrucuk

February 2021, 114 pages

In this thesis, the control allocation problem in a flight control system design for a multi-rotor eVTOL (electric Vertical Takeoff and Landing) aircraft is proposed. The vehicle consists of 20 identical rotors that are used as flight control actuators. The dynamic system is a MIMO (Multi Input Multi Output) system with more inputs than outputs, i.e. there are many solutions of the control problem. The objective is to find an efficient and redundant control solution that provides sufficient flight performance, handling quality, and power consumption. Developed control system algorithms are applied to a simulation model of the conceptual aircraft consisting of advanced and nonlinear dynamic components. By using this model, simulation based flight tests are conducted and the results are presented and evaluated. Also, redundancy of the control system is considered for flight safety. Therefore, various simulator based rotor failure scenarios are tested on the aircraft and the proposed method is also evaluated from a redundancy point of view. It is shown that robust and efficient control re-distribution can be achieved using the proposed solution under challenging failure conditions.

Keywords: Multi-Rotor, e-VTOL, Control Allocation, Over-actuated System, Blended-Inverse

ÖZ

KAVRAMSAL ÇOK PERVANELİ BİR E-VTOL HAVA ARACI İÇİN BLENDED-INVERSE KULLANARAK KONTROL DAĞITIMI

Aksoy, Emre
Yüksek Lisans, Havacılık ve Uzay Mühendisliği Bölümü
Tez Yöneticisi: Doç. Dr. İlkay Yavrucuk

Şubat 2021 , 114 sayfa

Bu tezde çok pervaneli bir eVTOL (Elektrik Gücü ile Dikey İniş Kalkış) hava aracı için uçuş kontrol sistemi tasarımı içindeki kontrol dağıtımı anlatılmaktadır. Bu araçta uçuş eyleyicisi olarak birbiriyle aynı 20 eş pervane bulunmaktadır. Dinamik sistem çoklu girdi çoklu çıktılı bir sistemdir ve girdiler çıktılardan daha fazladır. Bunun sonucunda birçok kontrol çözümü bulunabilmektedir. Hedef yeterli uçuş performansı, kumanda kabiliyeti ve güç tüketimini sağlayacak olan, verimli ve yedekli bir kontrol çözümü bulmaktır. Geliştirilen kontrol sistemi algoritması, gelişmiş ve doğrusal olmayan kavramsal hava aracının benzetim modeli üzerinde uygulanmıştır. Bu modeli kullanarak benzetim tabanlı uçuş testleri gerçekleştirilmiş ve bunların sonuçları sunularak değerlendirilmiştir. Ayrıca, bu kontrol sisteminin hata toleransı uçuş güvenliği için ele alınmıştır. Bunun için çeşitli pervane arıza senaryoları benzetim ortamında test edilmiş ve geliştirilen yöntem hata toleransı açısından da değerlendirilmiştir. Bu tezde anlatılan kontrol çözümü kullanılarak zorlayıcı arıza durumlarında kontrollerin verimli ve gürbüz bir şekilde yeniden dağıtımının elde edilebildiği gösterilmiştir.

Anahtar Kelimeler: Çoklu Rotor, e-VTOL, Kontrol Dağıtımı, Yedekli Sistem, Blended-Inverse

To limitless world of aviation...

ACKNOWLEDGMENTS

First and foremost, I would like to express my sincere gratitude to my thesis supervisor Dr. Ilkay Yavrucuk for his guidance and support. I always regard him and appreciate his ideas in my university education and engineering life. The completion of this study will not be possible without his aid which is very critical for my motivation.

I also thanks to my colleagues from "Aerotim", especially to Gönenç Gürsoy and Onur Tarımcı for their valuable suggestions.

I am particularly grateful to my friend Zeynep Ünal for helping along the way of thesis progression steps.

I would like to thank all of my family members for their patience and support throughout the whole time of my master education.

And, my special thanks is for my dear wife Beyzanur. She always shares my stress and happiness along the way of this study although we were still in our first lovely months of marriage.

TABLE OF CONTENTS

LIST OF TABLES

TABLES

LIST OF FIGURES

FIGURES

LIST OF ABBREVIATIONS

ABBREVIATIONS	
VTOL	Vertical Takeoff and Landing
CG	Center of Gravity
PID	Proportional Integral Derivative
PI	Proportional Integral
RPM	Revolutions per minute
ft	Feet
kts	Knots
fpm	Feet per minute
ref	Reference

CHAPTER 1

INTRODUCTION

1.1 Problem Definition and Focus

Electric Vertical Takeoff and Landing (eVTOL) aircraft are becoming increasingly popular in civil transportation due to their wide range of operational envelope. It also provides cost-effective and easy operation. Besides having many advantages, eVTOL aircraft have still problems that need to be addressed. One of them is the low flight range because of the limited power source. Rotors require rapid power during manoeuvring and batteries are exposed to high discharge rate to provide this power. Although batteries of recent technology can have high capacity, high discharge rates drain them so quickly [6].

Another issue that must be addressed is the fail safe and reliable operation, since eVTOL aircraft are designed to be used at urban area. It should overcome a failure that occurs in air and controllability should be maintained.
A current research topic in the rotorcraft community is a reliable control system design with low consumed power. Such control systems are achievable with redundant rotors or control surfaces to increase safety when single or multiple of these rotors fail during flight. Then the question is how control inputs are distributed between redundant rotors to satisfy the safety and efficiency criteria. This thesis focuses on the control allocation problem of such multi-rotor vehicles during normal operations and rotor failure cases.

1.2 Control Allocation in Literature

There are various types of control allocation methods in literature for over-actuated fixed and rotary wing aircraft. A common approach of these studies is to calculate the inverse of the control matrix [3, 8, 10, 14, 12]. Control system of a redundantly designed plant is an over-actuated system, which means that there are more actuators than the systems' degrees-of-freedom. Therefore, there are many solutions to the control problem. In [8, 4], specific constraints are applied to control inputs such as maximum deflection angle of a control surface or maximum rotational speed of a rotor, and the outputs are bound so that a finite physical solution can be obtained. The goal of the control allocation method in [8] is to generate high moments in the body-axes while considering constraints on the controls. Mapping between constrained control subset and the corresponding attainable moment subset is proposed.

Another method is the daisy-chaining solution [5]. This method, breaks the problem into smaller problems by grouping the controls. The main drawback of daisy-chaining is that, although it performs well inside each group, all attainable moments cannot be accessed when the solutions are united. Later, dynamic allocation methods are considered. In [9], constrained quadratic programming algorithm is developed. The main advantage of it is the automatic redistribution of controls when one actuator saturates to its limits or fails. However, it is mentioned that quadratic programming is quite a complex method to be used in practical applications.

Control allocation strategies are applied on various multi-rotor platforms in the literature [11, 15]. If control constraints are not considered, quite often the minimum-norm solution the Moore-Penrose (MP) pseudoinverse technique is used [13]. It is augmenting the control matrix to make it invertible. MP-pseudoinverse yields minimum control energy, but it does not yield good performance. Also, a common problem are the singularities during the inversion process. In [14], the singularities are removed by introducing a method called Blended-Inverse and applied to the attitude control problem for a satellite. As a rotorcraft application, this method is used in [12] to find optimum control allocation strategies for a compound helicopter. In those references, a continuous update on the control allocation strategy is demonstrated without any singularities in the calculations.

In multi-rotor eVTOL design, surviving from rotor failures is also important. In [2], arbitrary single rotor failure scenarios are considered for an octocopter in hover and forward flight conditions. Post failure trim analysis is done and the power requirement for various control modes are compared. In [3], rotor failures are addressed for a simple VTOL octorotor model. Here, a method based on control matrix dimension reduction [10] is applied in case of rotor failures,i.e. successive on-line redistribution of controls is achieved. Also an iterative control solution, called Redistributed Pseudo Inverse, is proposed in [10]. This method is applied on MP-pseudoinverse allocation and it prevents actuators from reaching its limits.

1.3 Objective of the Thesis

In this thesis, the methods of [14, 12, 3, 10] are used to form a redundant control allocation system for a 20 rotor eVTOL concept vehicle. The vehicle is similar to the one in Ref.[1]. The control system is designed in order to re-distribute the control law in case of arbitrary single or multiple rotor failure. The control system also considers the physical rotational speed limits of the rotors. It calculates the re-distribution that provides the best performance while keeping rotors away from saturation. The proposed control method is tested on a 6 Degrees-of-freedom simulation environment for several flight conditions and rotor failure scenarios. Simulation results of the scenarios are evaluated by considering power consumption, flight performance, flight safety and handling quality.

1.4 Organization

In Chapter-2 the proposed flight control system algorithm is explained. Control allocation matrix formation in [3], Blended-Inverse in [14], actuator saturation prevention and control matrix dimension reduction technique in [10] are presented. Explanations on the proposed on-line dynamic control allocation algorithm is also presented in this chapter. In Chapter-3, initially mathematical nonlinear model of the conceptual multi-rotor eVTOL aircraft is described. Then, 6 degrees-of-freedom flight simulator environment is explained. In Chapter-4 specific flight manoeuvres and various combinations of rotor failure scenarios are defined for simulation tests. These tests are conducted by using the conceptual aircraft model that the proposed flight control system algorithm is implemented. Finally, simulation results are shown and discussed. In the final chapter, Chapter-5, conclusions of the overall thesis are explained.

CHAPTER 2

METHODOLOGY

2.1 Introduction

This chapter consists of three sections. First, in Section-2.2 control allocation algorithm with Blended-Inverse is explained. Control allocation matrix formation, details of the Blended-Inverse logic and its implementation are explained. In Section-2.3, two approaches that prevent rotor saturations are described. Finally, in Section-2.4 control allocation with matrix dimension reduction method is explained in case of rotor failure.

2.2 Control Allocation with Blended-Inverse

The rotational speed of the rotors in electric powered Vertical Takeoff and Landing (vTOL) aircraft are often controlled independently by engine control units that provide necessary torque in order to keep the rotational speed of the rotor at a reference point. These reference values are assigned by the flight control system and they can be thought as the inputs given to the open loop dynamics. The multi-rotor aircraft is controlled with this reference inputs. By considering this information, the open loop plant dynamics can be represented with a nonlinear state equation as the following:

$$\dot{\boldsymbol{x}} = f(\boldsymbol{x}, \Omega_{ref}) \tag{2.1}$$

where "Ω_{ref}" is the rotational speed command vector generated by the flight control system for the engine control units.

The state vector ($\boldsymbol{x}$) in Eq. (2.1) is given as,

$$\boldsymbol{x} = [u \; v \; w \; p \; q \; r \; \phi \; \theta \; \Omega_1 \; \Omega_2 \; \Omega_3 \; ... \; \Omega_n]^T \tag{2.2}$$

where "u", "v", "w" are the translational body-frame velocities, p,q,r are the rotational body-frame velocities, "ϕ", "θ" are roll and pitch attitudes, "Ω" terms represent the rotational speed values of the rotors.

In Eq. (2.2), "n" is the number of rotors and each rotor speed is considered as a state because each rotor has independent dynamics. Details of rotor dynamics are explained in Chapter-3. In this study, the method is applied to a vehicle which has 20 rotors, then "$\mathrm{n} = 20$" (see Fig. 2.1).

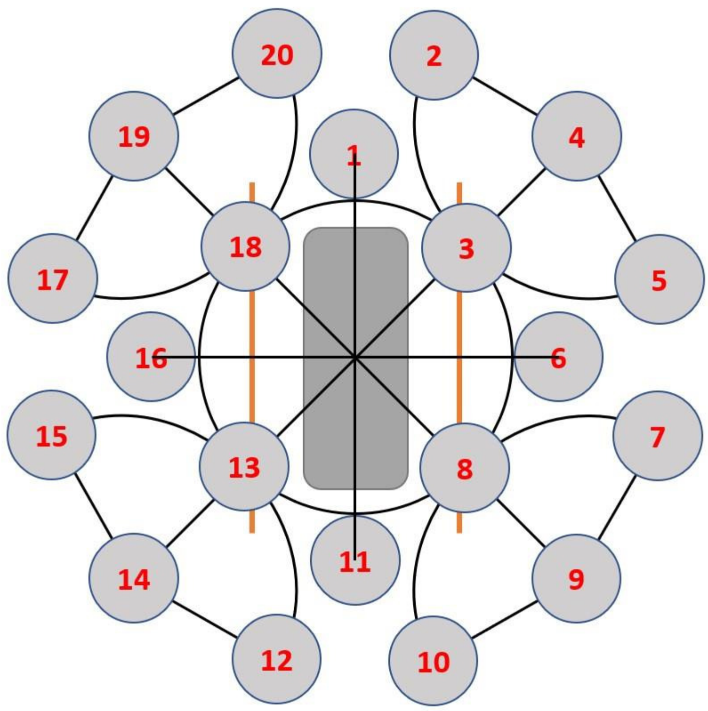

Figure 2.1: Concept eVTOL aircraft with 20 rotors

There are redundant controls in Eq. (2.1) because there are 20 rotors, thus 20 control inputs, correspond to 4 control inputs provided by the pilot: collective, pitch cyclic, roll cyclic and pedal (details are explained in Chapter-3). The main issue here is that how to find optimum combinations of "Ω_{ref}" for important design criteria such as low power consumption, sufficient handling qualities or in case of rotor failure. This yields to a control allocation problem that will be solved in this thesis.

2.2.1 Control Allocation Structure

Control allocation calculation is based on linearly relating inputs and outputs of the system. This relation is defined with the matrix which is known as the control allocation matrix. According to the state equation defined in the previous section (Eq. (2.1)), input vector is "$\Omega_{\text{ref}} \in \Re^{20}$" and it is defined in Eq. (2.3).

$$\Omega_{ref} = [\Omega_{ref_1}\ \Omega_{ref_2}\ \Omega_{ref_3}\ ...\ \Omega_{ref_{20}}]^T \tag{2.3}$$

Desired output vector "$\text{D} \in \Re^4$" can be defined as the following:

$$D = [T_D\ M_{xD}\ M_{y_D}\ M_{zD}]^T \tag{2.4}$$

where the elements are the desired thrust and moments in three directions of the body-axis frame.

Linear relation of "Ω_{ref}" and "D" is not meaningful because aerodynamic force changes quadratically with the effective velocity of a lifting surface ($\text{F}_{\text{aero}} \approx \text{V}_\infty{}^2$). Then, a virtual input vector can be defined to be used in the allocation formulation as following:

$$\Omega'_{ref} = [\Omega^2_{ref_1}\ \Omega^2_{ref_2}\ ...\ \Omega^2_{ref_{20}}]^T \tag{2.5}$$

By using Eq. (2.4) as the output and Eq. (2.5) as the input, the following linear relation is defined (Ref. [3]):

$$R\Omega'_{ref} = D \tag{2.6}$$

where "R $\in \Re^{4\times20}$" is the control allocation matrix representing the physical relation between rotor rotational speeds and the desired outputs.

Eq. (2.6) implies that the output force and moments are linearly proportional with the square of rotational speed inputs of rotors. This linear relation is defined by the control allocation matrix "R" and its elements are given by Eq. (2.7).

$$R = \begin{bmatrix} C_T & C_T & ... & C_T \\ C_T l_{y_1} & C_T l_{y_2} & ... & C_T l_{y20} \\ C_T l_{x_1} & C_T l_{x_2} & ... & C_T l_{x20} \\ C_Q \tau_1 & C_Q \tau_2 & ... & C_Q \tau_{20} \end{bmatrix} \tag{2.7}$$

Parameters of "R" matrix are explained below:

- C_T: Thrust coefficient
- C_Q: Torque coefficient
- l_{xn}: Longitudinal moment arm of $\mathrm{n^{th}}$ rotor with respect to C.G. of the aircraft (Fig. 2.2)
- l_{y_n}: Lateral moment arm of $\mathrm{n^{th}}$ rotor with respect to C.G. of the aircraft (Fig. 2.2)
- τ_n: Rotation direction of $\mathrm{n^{th}}$ rotor. ($\tau = 1$): clockwise rotation, ($\tau = -1$): counter-clockwise rotation

Thrust coefficient ($\mathrm{C_T}$) and torque coefficient ($\mathrm{C_Q}$) are constant values obtained from isolated single-rotor analysis but they change with the flight condition for more accurate aerodynamic response. The details are explained and the values are tabulated in the Appendix-A.3.

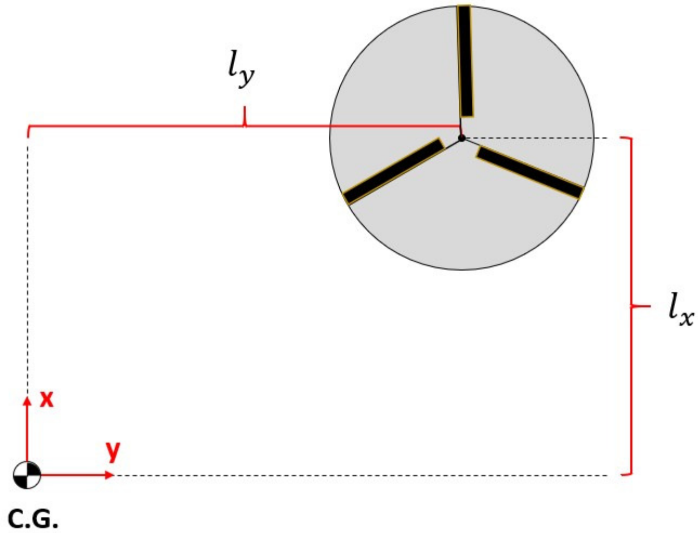

Figure 2.2: Rotor moment arms

In the control allocation matrix (Eq. (2.7)), each column represents single rotor aerodynamics, i.e. total of 20 columns represent 20 rotors. If rows are considered, 4 rows represent thrust sharing, roll moment sharing, pitch moment sharing and yaw moment sharing, respectively. In the light of this explanation, control allocation expressed in Eq. (2.6) is written below in explicit form, for convenience.

Thrust sharing (1^{st} row of "R"):

$$C_T \Omega'_{ref_1} + C_T \Omega'_{ref_2} + \ \ldots \ + C_T \Omega'_{ref_{20}} = T_D \tag{2.8}$$

Roll moment sharing (2^{nd} row of "R"):

$$C_T l_{y_1} \Omega'_{ref_1} + C_T l_{y_2} \Omega'_{ref_2} + \ \ldots \ + C_T l_{y_{20}} \Omega'_{ref_{20}} = M_{xD} \tag{2.9}$$

Pitch moment sharing (3^{rd} row of "R"):

$$C_T l_{x_1} \Omega'_{ref_1} + C_T l_{x_2} \Omega'_{ref_2} + \ \ldots \ + C_T l_{x_{20}} \Omega'_{ref_{20}} = M_{yD} \tag{2.10}$$

Yaw moment sharing (4^{th} row of "R"):

$$C_Q \tau_1 \Omega'_{ref_1} + C_Q \tau_2 \Omega'_{ref_2} + \ ... \ + C_Q \tau_{20} \Omega'_{ref_{20}} = M_{zD} \tag{2.11}$$

Using the relation in Eq. (2.6), reference rotational speeds "Ω_{ref}" mentioned in Eq. (2.3) can be calculated by following the steps below:

$$\Omega'_{ref} = R^{-1} D \tag{2.12}$$

$$\Omega_{ref} = \sqrt{\Omega'_{ref}} \tag{2.13}$$

The inversion in Eq. (2.12) is not possible because "$\mathrm{R} \in \Re^{4\times 20}$" is a non-square matrix. The successful inversion of the control allocation matrix "R" is achieved by using the Blended-Inverse (Ref. [14]) which is explained in the following section.

2.2.2 Inversion with Blended-Inverse

A non-square matrix is inverted commonly by using the minimum-norm solution, which is known as the pseudo-inverse. A major drawback of this method is the fact that it does not handle singularities. In addition, it does not give the best performance solution (Ref. [12]). To overcome the singularity issue and obtain the best manoeuvring performance with minimum energy consumption, the Blended-Inverse technique (Ref. [14]) is used. The method is adapted to the multi-rotor control problem which is the proposed method of this thesis, and described below.

According to [14], the minimization problem for the control system is defined as following:

$$\min_{\Omega'_{ref}} \frac{1}{2} \{ \Omega'^{T}_{ref_e} Q \, \Omega'_{ref_e} + {D_e}^T F D_e \} \tag{2.14}$$

where "$\mathrm{Q} \in \Re^{20\times 20}$" and "$\mathrm{F} \in \Re^{4\times 4}$" are the square weight matrices of input and desired output respectively, and "e" represents the errors.

Weight matrices are used to give importance to the corresponding parameter. Increasing weight matrix elements will increase the error term multiplied by the matrix. This yields to a smaller value of the corresponding parameter in the final solution. Then, if one wants not to change a parameter in the minimization equation (Eq. (2.14)) much, its related weight matrix should be increased. Selection of weight matrices "Q" and "F" for the study of this thesis is described in Appendix-A.6.

Error terms are defined as:

$$\Omega'_{ref_e} = \Omega'_{ref} - \Omega'_{ref_d} \tag{2.15}$$

$$D_e = R\Omega'_{ref} - D \tag{2.16}$$

where subscript "d" denotes "desired" variables and "$\Omega'_{\mathrm{ref\,d}} \in \Re^{20}$".

In Eq. (2.15), the following relation is held:

$$\Omega'_{ref_d} = \Omega^2_{ref_d}$$

In the above relation, elements of "$\Omega_{\mathrm{ref_d}}$" vector are specified by using hover trim condition of the aircraft. The purpose of defining such a desired vector is to keep rotor rotational speeds around the trim values as much as possible. With this approach efficient distribution of inputs will be obtained. Details of estimating trim values and the related calculations are shown in Appendix-A.4.

In Eq. (2.16), desired thrust and moments vector "D" (Eq. (2.4)) is specified by linear mapping of the pilot controls in 4 axes:

- $f(\delta_{coll}) = T_D$
- $f(\delta_{roll}) = M_{xd}$
- $f(\delta_{pitch}) = M_{y_d}$

- $f(\delta_{yaw}) = M_{zd}$

Definition of the pilot controls are described in Chapter-3, and the mapping functions above are explained in Appendix-A.5.

Solution of Eq. (2.14) is the Blended-Inverse solution which is given by:

$$\Omega'_{ref} = [Q + R^T F R]^{-1} [Q \Omega'_{ref_d} + R^T F D] \tag{2.17}$$

The overall control system block diagram is shown in Fig. 2.3.

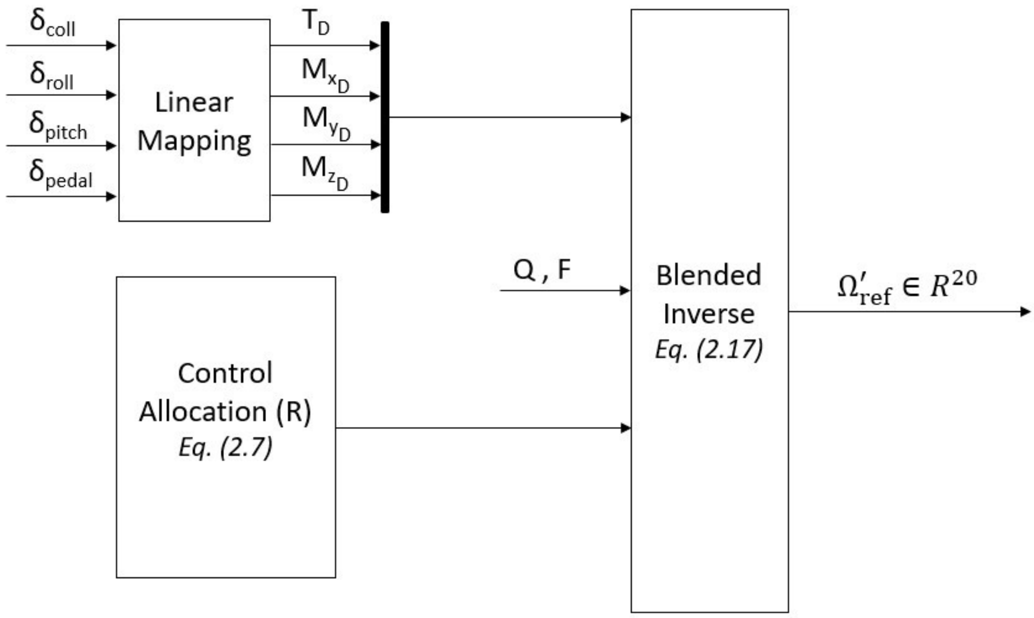

Figure 2.3: Flight control system block diagram

2.3 Rotor Saturation Avoidance Algorithm

Actuator saturation is always taken into account while designing flight control systems in engineering. This is a limiting factor because a saturated actuator cannot generate further control force if greater command is demanded. For example, a lifting surface at its maximum deflected position cannot produce much more lift. As a result, a vehicle becomes uncontrollable with a saturated actuator. To avoid actuator saturation, control systems are designed such that preventive actions are activated if any saturation in controls is detected. In this study, control inputs are rotor rotational speeds of the multi-rotor aircraft and it is physically limited to a maximum amount.

Two methods are proposed to prevent rotor saturation and they are explained in the following sections (Section-2.3.1 and 2.3.2).

2.3.1 Saturation Avoidance Using Weight Matrices

In this section, rotor saturations are avoided by modifying the weight matrices. Increasing the value in the weight matrix increases importance of the corresponding input or output term in the cost function (Eq. (2.14)). Therefore, variation of that term is reduced. By using this approach, the weight matrix is successively modified in Ref. [12]. With a similar way, the input weight matrix "Q" of Eq. (2.17) is modified using the following formulation:

$$Q = diag(q\sigma_i)$$

where "q" is the blending coefficient (taken as a scalar: "$\mathrm{q} = 0.01$"), "σ" is the variation parameter, and subscript "i" represents individual rotor.

Details of selection of "q" is explained in Appendix-A.6.

Variation parameter (σ) is calculated from the following equations for each rotor denoted by "i":

$$\sigma_i = \frac{\Delta_{max}}{\Delta_i}$$

$$\Delta_i = \Omega'_{sat} - \Omega'_{ref_i}$$

$$\Delta_{max} = max(\Delta_i)$$

$$\Omega'_{sat} = \Omega^2_{sat}$$

$$\Omega'_{ref_i} = \Omega^2_{ref_i}$$

where "Ω_{sat}" is the rotor saturation limit and "$\Omega_{\mathrm{ref_i}}$" is the reference rotor speed of individual rotor provided by the flight control system.

2.3.2 Saturation Avoidance by Modifying Blended-Inverse

The control system described in Section. 2.2 is improved in this section so that generated rotational speed reference of rotors will not exceed the limit value (physical saturation).

An iterative solution is applied in [10] over Moore-Penrose pseudo-inverse calculation. This solution is adapted to the Blended-Inverse and the formulation is explained in this section.

The basic is that, if a rotor rotational speed beyond the upper limit is demanded by the control system, the corresponding rotor reference is fixed to the limit value and the remaining effect is obtained from the other rotors by input re-distribution. After the updated distribution, if there is no other saturation in rotors, the current input combination is passed forward. However if a new saturation exists, the corresponding rotor speeds are fixed to the upper limit and inputs are re-distributed again. This iteration (Fig. 2.4) is maintained until any of the rotor reference exceeds the upper limit.

For the modification of the Blended-Inverse formulation (Eq. (2.17)), firstly, offset vector "$\mathrm{c} \in \Re^{20}$" is defined. If a rotor is saturated, its corresponding element in "c" is assigned the upper limit value. If no rotor is saturated, all elements of "c" are zero.

By using "c", the modified version of Eq. (2.17) is written as following:

$$\Omega'_{ref} = [Q + R^T_{mod} F R_{mod}]^{-1} [Q \Omega'_{ref_d} + R^T_{mod} F (D - Rc)] \tag{2.18}$$

"$\mathrm{R_{mod}}$" in Eq. (2.18) is the modified control allocation matrix where its columns correspond to saturated rotors are zeroed out in order to eliminate their effect from the solution. If no rotor is saturated, "$\mathrm{R_{mod}}$" matrix is same as the original "R".

One final step is needed to complete the solution. Elements of "$\Omega'_{\mathrm{ref\,d}}$" vector which are related to saturated rotors should be assigned to the upper limit of rotational speed. The zeroing out process during "$\mathrm{R_{mod}}$" calculation (explained previously) is required because the saturated rotors are already assigned to the upper limit in the "$\Omega'_{\mathrm{ref\,d}}$" vector.

Considering an example saturation case for convenience.

Sample Calculation

Let's say the control system demands for rotor-2 and rotor-4 to be rotated beyond the upper limit of a single rotor rotational speed. Then, "$\mathrm{R_{mod}}$" should be like,

$$R_{mod} = \begin{bmatrix} C_T & 0 & C_T & 0 & C_T & \dots & C_T \\ C_T l_{y_1} & 0 & C_T l_{y_3} & 0 & C_T l_{y_5} & \dots & C_T l_{y_{20}} \\ C_T l_{x_1} & 0 & C_T l_{x_3} & 0 & C_T l_{x_5} & \dots & C_T l_{x_{20}} \\ C_Q \tau_1 & 0 & C_Q \tau_3 & 0 & C_Q \tau_5 & \dots & C_Q \tau_{20} \end{bmatrix}$$

The offset vector "c" will be,

$$c = [0 \ \Omega'_{ref_{max}} \ 0 \ \Omega'_{ref_{max}} \ 0 \dots 0]^T$$

The desired virtual input vector will be,

$$\Omega'_{ref_d} = [\Omega'_{ref_{d_1}} \ \Omega'_{ref_{max}} \ \Omega'_{ref_{d_3}} \ \Omega'_{ref_{max}} \ \Omega'_{ref_{d_5}} \dots \Omega'_{ref_{d_{20}}}]^T$$

Also, flow chart of the proposed iterative solution is shown in Fig. 2.4.

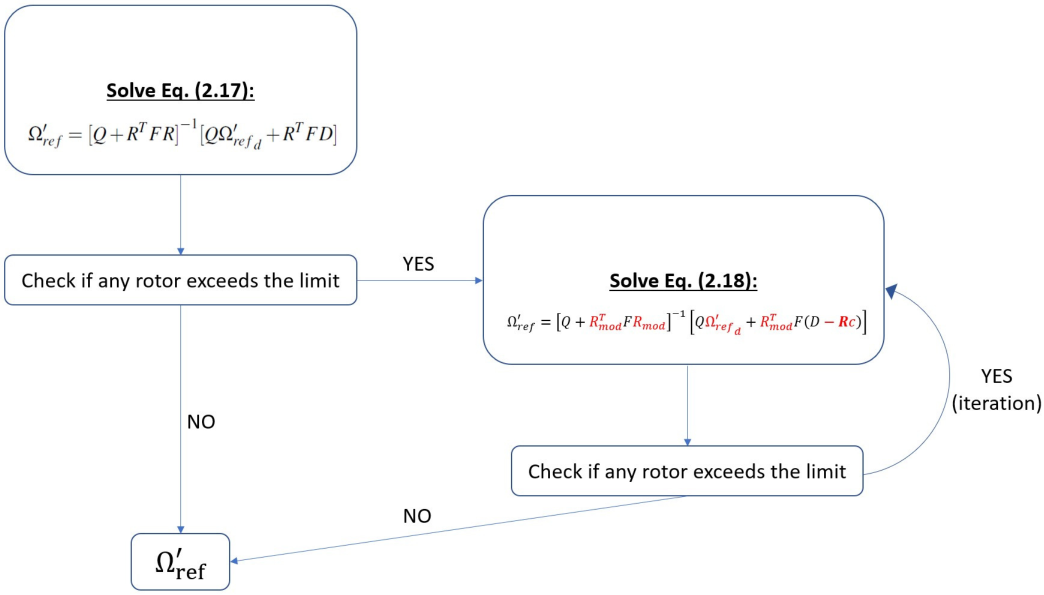

Figure 2.4: Flow chart of rotor saturation avoidance algorithm

2.4 On-line re-distribution in Rotor Failure

Flight safety is a major issue in designing an aircraft. From the control point of view, aircraft can be designed with redundant control actuators where the overall system yields to an "over-actuated system". In this thesis, the application plant is also an over-actuated system in which there are 20 rotors operating under the effect of 4 pilot control inputs. In control system design, the proper input re-distribution is required in case of rotor failure for the flight safety.

Control allocation with Blended-Inverse provides a solution that the total thrust is shared between all rotors in order to achieve the desired lift and moments. In [10], "Redistributed Pseudo Inverse" method is proposed for the rotor failure solution. In this study, the Blended-Inverse equation is used instead of the pseudo-inverse.

If a rotor fails, dimension of the control allocation matrix in Eq. (2.7) is reduced such that its corresponding column is removed. As a result, the failed rotor will not be included in the control allocation. The same desired thrust and moments are shared between only the operating rotors. The same dimension reduction should be applied to the weight matrix "Q" in Eq. (2.17), the desired virtual input vector "$\Omega'_{\mathrm{ref\,d}}$" in Eq. (2.17) and the offset vector "c" in Eq. (2.18) in order to solve the control allocation problem correctly.

For instance, if the number of failed rotors is "f", then the parameters of the Blended-Inverse equation become as the following:

- **Control allocation matrix**: $\mathrm{R} \in \Re^{4\times(20-\mathrm{f})}$
- **Input weight matrix**: $\mathrm{Q} \in \Re^{(20-\mathrm{f})\times(20-\mathrm{f})}$
- **Desired virtual input vector**: $\Omega'_{\mathrm{ref\,d}} \in \Re^{20-\mathrm{f}}$
- **Input offset vector**: $\mathrm{c} \in \Re^{20-\mathrm{f}}$

The on-line re-distribution method by dimension reduction technique, which is explained above, is able to work simultaneously with the "rotor saturation avoidance algorithm" explained in Section-2.3.2. Complete work flow chart of the flight control system is shown in Fig. 2.5.

Firstly, the control system checks to see if a rotor failure exists. If so, the dimension reduction technique is applied to necessary matrices and vectors, and a re-distribution is obtained along the remaining operating rotors. Otherwise, only the basic Blended-Inverse equation (Eq. (2.17)) is executed. There is no detection system for rotor failure. It is assumed that the proposed system knows if a failure happens and which rotors are failed, if so.

After rotor failure compensation, the "rotor saturation avoidance algorithm" is executed and a re-distribution iteration is performed with no rotor saturation. Since failed rotors are excluded from the allocation in the first step via dimension reduction, the "rotor speed limit avoidance system" prevents actuator saturation of only the operating rotors. With this step, final input distribution is obtained on-line.

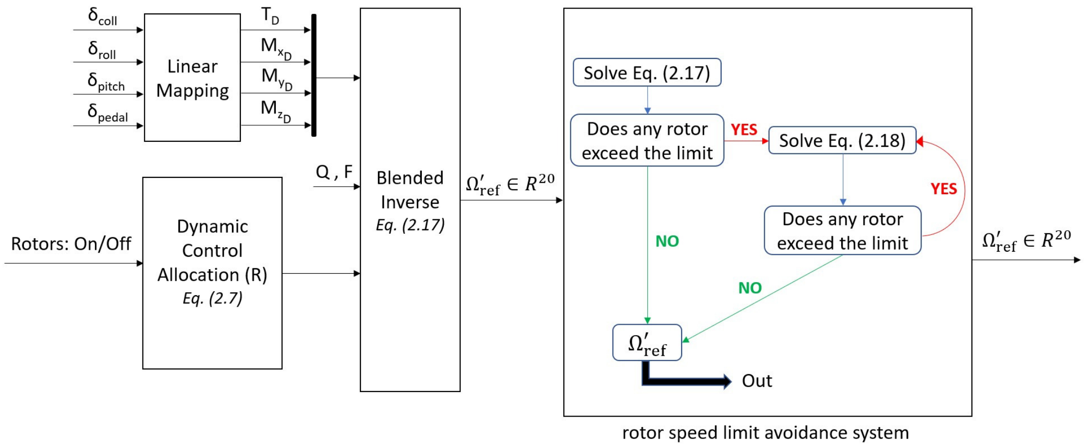

Figure 2.5: Flow chart of final form of the flight control system

CHAPTER 3

SIMULATION ENVIRONMENT

3.1 Introduction

In this chapter details of the simulation structure is explained in which the proposed method described in Chapter-2 is implemented. In Section-3.2, development steps of mathematical model of the conceptual eVTOL aircraft is described in details. Also, complementary simulation components that are necessary to obtain accurate test results are explained. These components consist of three parts: atmosphere model, 6-degrees-of-freedom equations of motion, and autopilot controller. These models are used for simulation tests conducted in Chapter-4.

3.2 Mathematical Model of the Concept Multi-Rotor eVTOL Aircraft

The conceptual aircraft is a multi-rotor eVTOL concept and its top view is shown in Fig. 3.1. Also, its dimensions are shown in Fig. 3.2. Its mathematical model is nonlinear and consists of 20 rotors with electric motors, fuselage and landing gear. The vehicle can be controlled by only changing the rotational speed of rotors. Flight control system determines the necessary rotor speed distribution and it sends rotational speed commands to each rotor. This command is received by the electric motors with electronic speed controller that provides required torque in order to match the rotational speed of rotors with the command.
The aircraft is designed to be controlled by a pilot and the pilot control inputs are defined as collective, cyclic and pedal. Collective input provides control in the vertical axis,i.e. it increases or decreases the overall lift force. Cyclic inputs consists of

two parts: longitudinal cyclic and lateral cyclic. They provide control in pitch axis and roll axis, respectively. Finally, pedal is used to control the yaw behaviour of the aircraft.

Mathematical models of the aircraft's main components are explained in detail in the following sections.

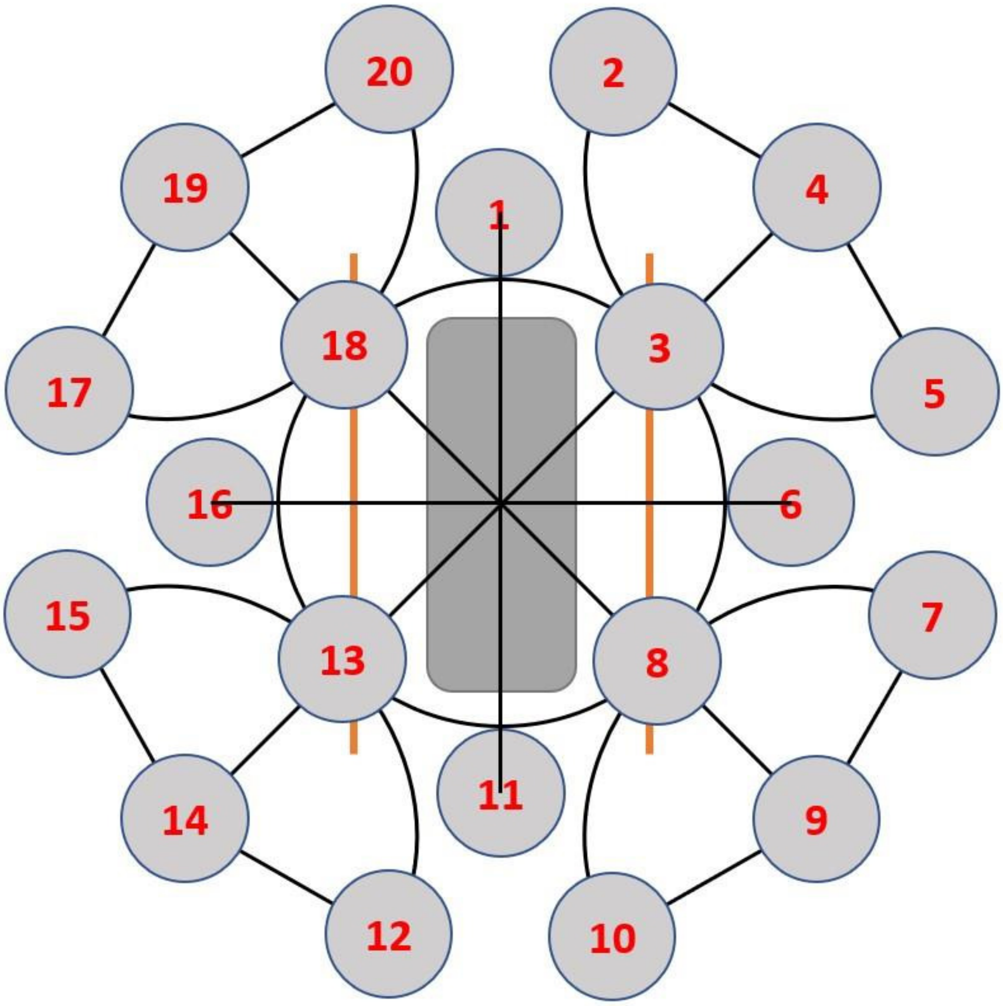

Figure 3.1: Concept eVTOL aircraft with 20 rotors

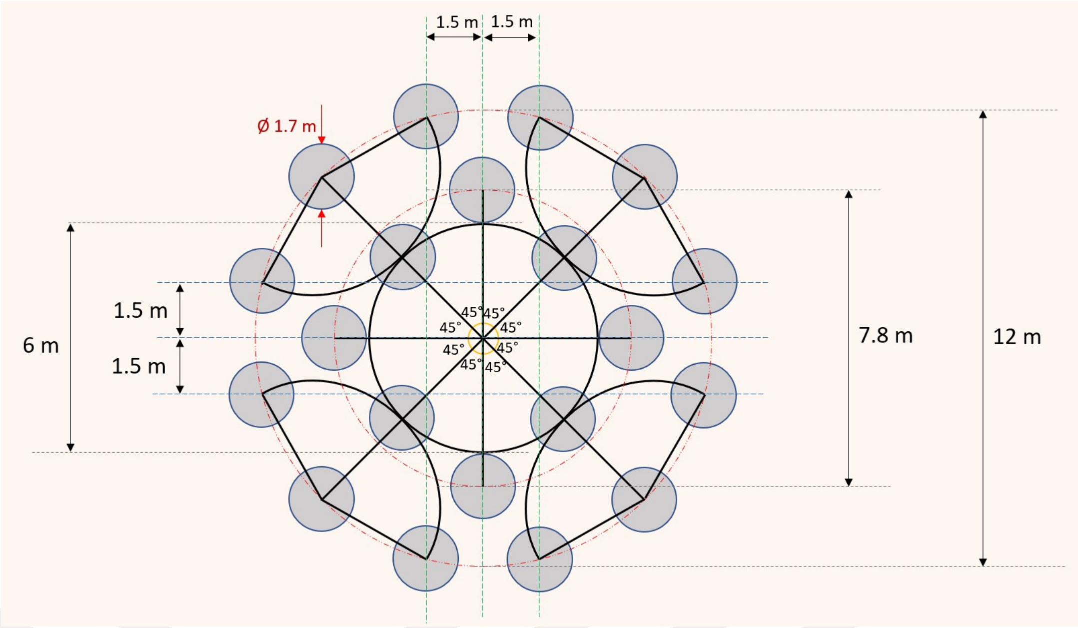

Figure 3.2: Concept eVTOL aircraft dimensions

3.2.1 Rotor Model

All rotors are modelled identically. A single rotor properties are listed in Table 3.1.

Parameter	**Value**	**Variable Name**
Blade number	3	N
Rotor radius (m)	0.85	R
Rotational inertia ($\mathrm{kg.m^2}$)	1.45	$\mathrm{I_z}$

Table 3.1: Rotor Properties

Rotor rotational inertia is approximated using the geometry.

All rotors are numbered for identification. Rotors with odd number rotate in clockwise direction and, even numbered rotors rotate in counter-clockwise direction. Then, yaw balance is obtained when all rotors are working.

For modelling, Blade Element Theory with 1-state dynamic mean inflow is used. In the aircraft, spacing between rotors is large enough so that rotors' inflow do not affect each other. Therefore, aerodynamic interactions between rotors are neglected.

3.2.1.1 Reference Frame and Coordinate System Definitions

Before getting into the equations, reference frames and coordinate systems used in calculations will be defined.

- *Body-Frame:* Reference frame that is attached to the C.G. of the aircraft (Fig. 3.3). It moves and rotates with it.
- *Hub-Frame:* Non-rotating frame that is attached to the rotor hub (Fig. 3.4).
- *Rotor-Frame:* Reference frame that is attached to the root of a single blade and rotates with it (Fig. 3.5).

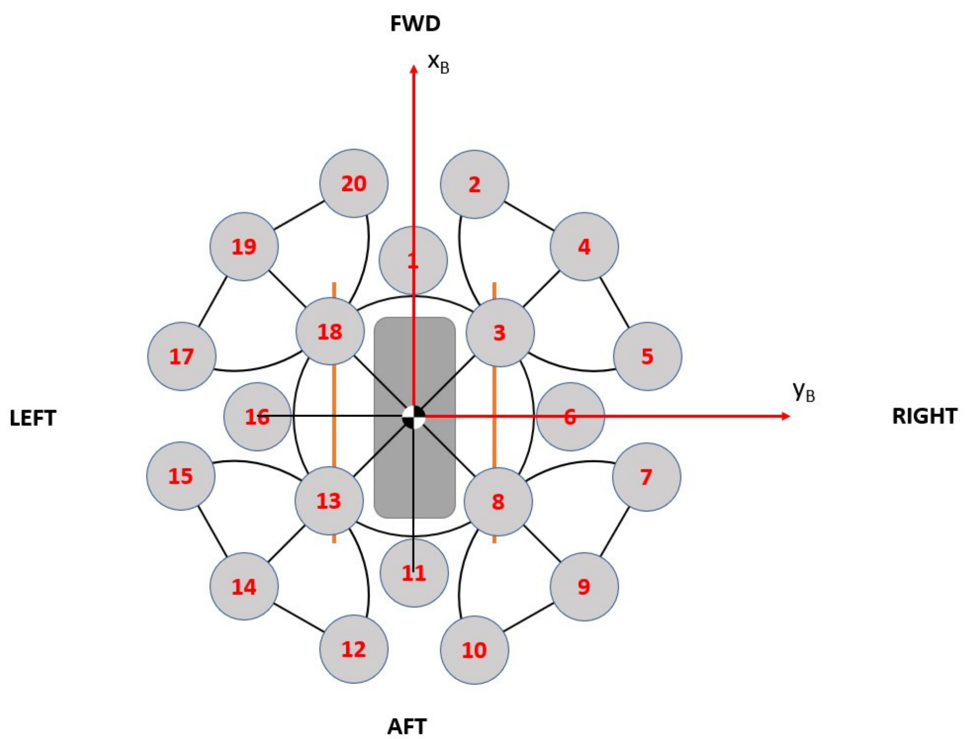

Figure 3.3: Body Fixed Frame

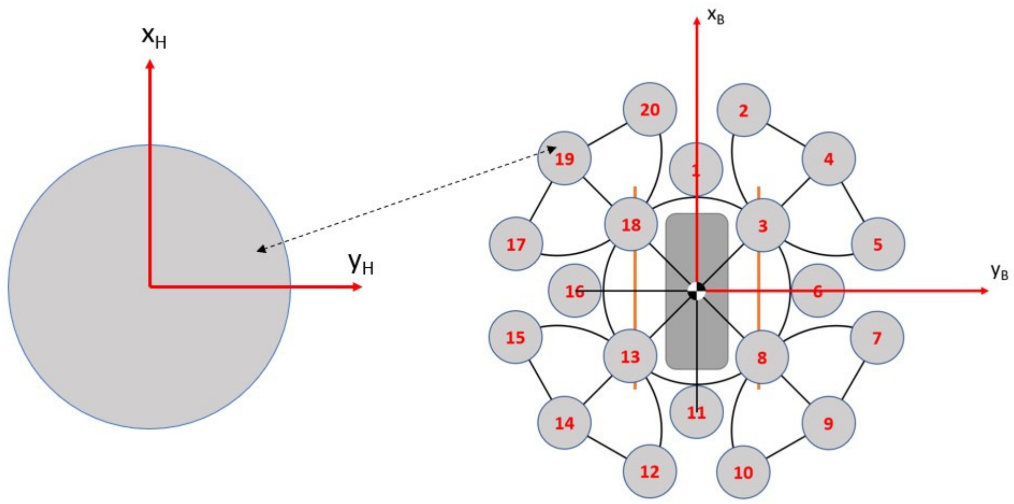

Figure 3.4: Hub Frame

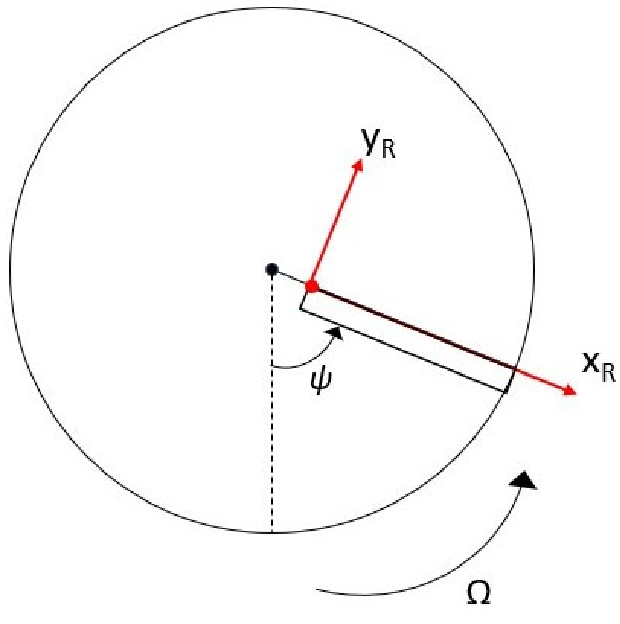

Figure 3.5: Rotor Frame of a rotor with counter-clockwise rotation

All coordinate systems used in this study use the right-hand rule.

3.2.1.2 Blade Element Theory

In Blade Element Theory, aerodynamic forces and moments of an infinitesimal blade section are calculated in the rotor frame (Fig. 3.5). Then, integration along the blade span from root to tip and also along the azimuth from $0°$ to $360°$ degrees gives the total forces and moments for the single blade. Blade properties are shown in Table 3.2. These parameters are used for calculations in this section.

Parameter	Value	Variable Name
Chord length	0.05 m	c
Airfoil type	NACA 0012	-
Linear twist	$-8°$	θ_{tw}
Precone angle	$13°$	θ_0

Table 3.2: Single Blade Properties

Free-body diagram of an infinitesimal blade section is given in Fig. 3.6 that shows force vectors, velocity components and specific angles related with aerodynamics.

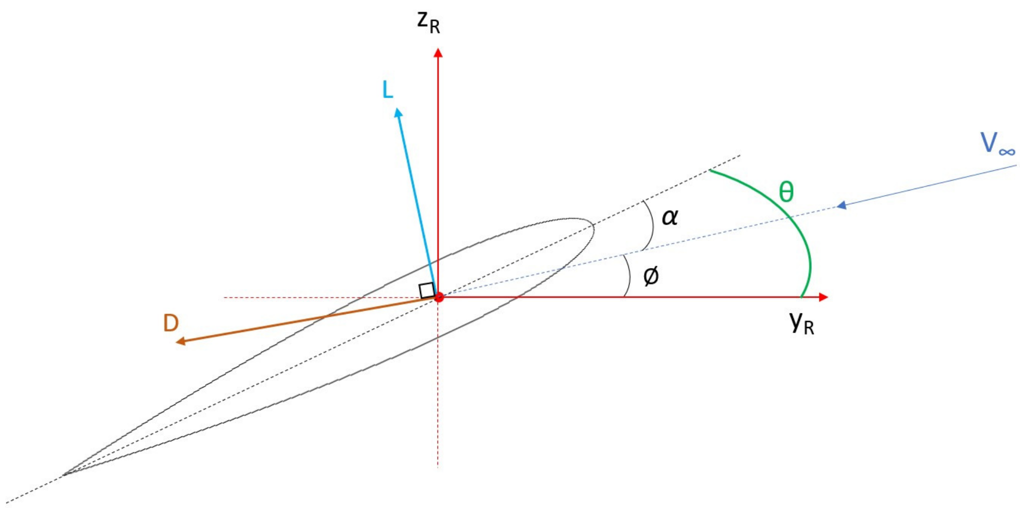

Figure 3.6: Free-body diagram of a blade section

In Fig. 3.6 "V_∞" is the free-stream velocity, "α" is the angle of attack, "ϕ" is the inflow angle, "θ" is the blade pitch angle, "L" is the lift force and "D" is the drag force. Calculation of each of these parameters are explained below.

Free-stream velocity:

$$V_{\infty} = \sqrt{{u_P}^2 + {u_T}^2} \tag{3.1}$$

where "$\mathrm{u_P}$" and "$\mathrm{u_T}$" are perpendicular and tangential velocity components of "$\mathrm{V_{\infty}}$".

$$u_P = w_i - w \tag{3.2}$$

and

$$u_T = \Omega r + u \sin(\psi) + v \cos(\psi) \tag{3.3}$$

where "u", "v", "w" are the three velocity components of the body-fixed frame, "r" is the radius of the current blade section, "ψ" is the current azimuth angle and "$\mathrm{w_i}$" is the inflow induced by the rotor.
Inflow is calculated according to dynamic mean inflow estimation in [7]:

$$\tau \dot{\lambda}_w = -2\frac{|V_a|}{V_T}\lambda_w + C_T \tag{3.4}$$

where "λ_w" is the non-dimensional inflow, "$\mathrm{V_a} = \sqrt{\mathrm{u_T}^2 + \mathrm{u_P}^2}$", "$\mathrm{V_T} = \Omega\mathrm{R}$" is the blade tip speed, "$\mathrm{C_T}$" is the non-dimensional thrust, "$\tau = 4\mathrm{k}^3/3$".
According to [7], values of k is between 0.74 and 0.86. For this model, "$\mathrm{k} = 0.8$" is used. Non-dimensional thrust in Eq. (3.4) is calculated as following:

$$C_T = \frac{T}{\rho A {V_T}^2} \tag{3.5}$$

where "T" is the total thrust produced by the rotor, "ρ" is the air density and "$\mathrm{A} = \pi\mathrm{R}^2$" is the rotor disk area.

According to [7],

$$\dot{w}_i = \dot{\lambda}_w(\Omega^2 R) \tag{3.6}$$

Rotor inflow dynamics is propagated with Eqs. (3.4), (3.5) and (3.6). After having calculated "$\mathrm{u_T}$" and "$\mathrm{u_P}$", inflow angle is calculated from them:

$$\phi = \frac{u_P}{u_T} \tag{3.7}$$

Blade pitch angle:

$$\theta = \theta_0 + r\theta_{tw} \tag{3.8}$$

Angle of attack:

$$\alpha = \theta - \phi \tag{3.9}$$

Lift (L) and drag (D) forces are functions of the parameters defined above.

$$L = \frac{1}{2}\rho {V_\infty}^2 S C_L \alpha \tag{3.10}$$

$$D = \frac{1}{2}\rho {V_\infty}^2 S C_D \alpha \tag{3.11}$$

where "S" is the blade section area and "$\mathrm{C_L}$, $\mathrm{C_D}$" are aerodynamic lift and drag coefficients respectively.
"$\mathrm{C_L}$, $\mathrm{C_D}$" in Eqs. (3.10), (3.11) are function of angle of attack (α). The relation between them is shown in Appendix-A.2.

Blade section area (S) in Eqs. (3.10) and (3.11) is constant along the blade span since there is no taper ratio and chord length is constant from blade root to tip. Then blade section area is "$\mathrm{S = c(\Delta r)}$" and "Δr" is the infinitesimal radius length.

Finally, force equations in Fig. 3.6 can be written in the rotor frame as following:

$$F_y = -L\sin(\phi) - D\cos(\phi) \tag{3.12}$$

$$F_z = L\cos(\phi) - D\sin(\phi) \tag{3.13}$$

where "$\mathrm{L}\sin(\phi)$" term corresponds to induced drag by the lift force.

Resultant force vector of the blade expressed in the rotor frame is:

$$\vec{F}_R = \begin{bmatrix} F_x \\ F_y \\ F_z \end{bmatrix} \tag{3.14}$$

where "$\mathrm{F_x} = 0$" since there is no force produced through the radial direction of the blade.

Then, moments are calculated by using the forces found in Eqs. (3.12) and (3.13):

$$\vec{M}_R = \vec{r}_R \times \vec{F}_R \tag{3.15}$$

where $\vec{r}_R$ and $\vec{M}_R$ are current position and moment vectors written with respect to the rotor frame, respectively.

Up to this point, force and moment vectors of an infinitesimal blade section in the rotor frame are calculated. Integration from blade root to blade tip and $0°$ azimuth to $360°$ azimuth gives the total forces and moments in the rotor frame.

For integration along blade span, radius increment of "$\Delta\mathrm{r} = 0.0425\ \mathrm{m}$" is used. Azimuth integration is performed as if the rotor has 16 virtual blades. As a result, azimuth increment is "$\Delta\psi = \frac{360}{16} = 22.5°$" during integration. Then the final force and moments are calculated as following:

$$F_{actual} = \frac{F_{virtual}}{16} \times 3 \tag{3.16}$$

Similarly,

$$M_{actual} = \frac{M_{virtual}}{16} \times 3 \tag{3.17}$$

Finally, Equations (3.16) and (3.17) are included in order to cover the disk area of the rotor as much as possible. This approach gives more accurate response to change of rotor inputs. Another way of doing this can be reducing the step size of the simulation. However, in this case computational time of the simulation will be increased or more sophisticated hardware is needed.

3.2.1.3 Modifications for rotors with clockwise rotation

Mathematical changes should be made in the calculations in order to obtain correct dynamics for the rotors rotated clockwise. First of all, new rotor frame is defined in Fig. 3.7 to be used in the calculations.

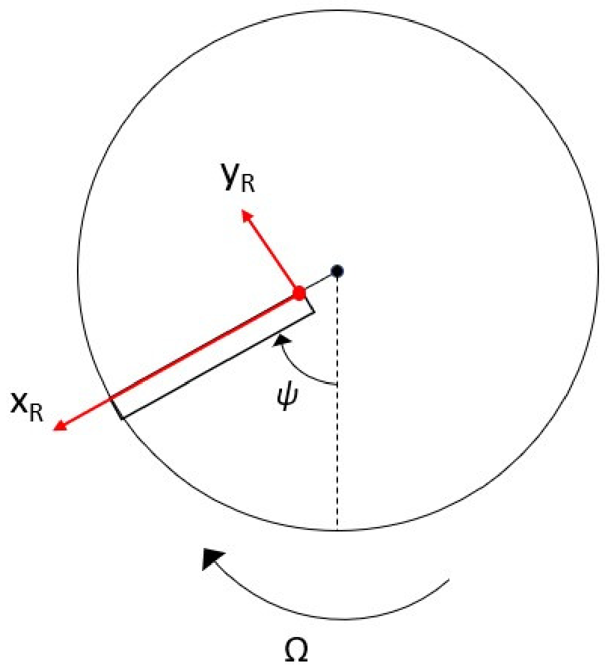

Figure 3.7: Rotor Frame of a rotor with clockwise rotation

Tangential velocity calculation of a blade section in Eq. (3.3) should be changed as following:

$$u_T = \Omega r + u \sin(\psi) - v \cos(\psi) \tag{3.18}$$

Eq. (3.18) implies that tangential velocity of a blade section passing through front side of the rotor disk increases while the aircraft flies through right side.

Another modification is for the direction of the lift force. By comparing two rotor frames shown in Figs. (3.5) and (3.7), z-axis direction of clockwise rotor frame is in the opposite direction of z-axis of counter-clockwise rotor frame. This requires sign change of a single blade section lift force. Then, Eq. (3.13) becomes as following:

$$F_z = -L \cos(\phi) + D \sin(\phi) \tag{3.19}$$

Lastly, another modification is needed for the coordinate system transformation from rotor frame to hub frame. This is explained in the following section.

3.2.1.4 Transformation of Forces and Moments from Rotor-Frame to Body Fixed Frame

Output of the rotor model should be expressed in the body fixed frame because the outputs are sent to 6 degrees-of-freedom equations of motion. First, output vectors should be transformed to hub frame from rotor frame. Then, they should be transformed from hub frame to body fixed frame. However, the latter operation is not necessary because hub frame and body fixed frame are aligned to each other in this vehicle (see Fig. 3.4). This is due to the fact that there is no tilt angle at rotor hubs. Rotors are placed parallel to the ground and the xy-plane of the body fixed frame.

Two types of transformation is needed due to existence of two different rotor frames (Figs. (3.5), (3.7)). At first, counter-clockwise rotated rotor transformation is explained.

Transformation of a rotor with counter-clockwise rotation:

First transformation is around the z-axis (vertical axis) of the rotor frame. In order to align the y-axes of rotor-frame and hub-frame, rotor frame should be rotated in the negative direction with "ψ" amount:

$$R_z(-\psi) = \begin{bmatrix} cos(-\psi) & sin(-\psi) & 0 \\ -sin(-\psi) & cos(-\psi) & 0 \\ 0 & 0 & 1 \end{bmatrix} \tag{3.20}$$

After that, to align x and z axes, 180 degrees rotation is needed around the y-axis:

$$R_y(180°) = \begin{bmatrix} cos(180°) & 0 & -sin(180°) \\ 0 & 1 & 0 \\ sin(180°) & 0 & cos(180°) \end{bmatrix} \tag{3.21}$$

The final transformation can be written as:

$$L_{R2H} = R_y(180°) \times R_z(-\psi) \tag{3.22}$$

where R2H: Rotor to Hub frame.

Transformation of a rotor with clockwise rotation:

For a rotor rotating in clockwise direction, one additional calculation step is required for transformation from rotor to hub frame. This additional step should be performed between Eq. (3.20) and Eq. (3.21). The overall transformation steps are as following:

1) Perform Eq. (3.20)

2) To align y-axis, 180 degrees rotation is needed around the x-axis:

$$R_x(180°) = \begin{bmatrix} 1 & 0 & 0 \\ 0 & cos(180°) & sin(180°) \\ 0 & -sin(180°) & cos(180°) \end{bmatrix} \tag{3.23}$$

3) To align x and z axes, perform Eq. (3.21)

After completed the steps above, the final transformation will be written as:

$$L_{R2H} = R_y(180°) \times R_x(180°) \times R_z(-\psi) \tag{3.24}$$

where R2H: Rotor to Hub frame.

3.2.2 Electric Motor Model

Each rotor is equipped with its own electric motor which includes electronic speed controller. The main objective of the motor is to keep the rotational speed of the rotor with the rotational speed command received from the flight control system. Torque loss due to friction forces is also modelled as a linear function of rotor's rotational speed (Eq. (3.25)). Block diagram of the single electric motor and corresponding rotor dynamics is shown in Fig. 3.8. Rotors are modelled as they cannot rotate in the opposite direction to their defined rotational directions. Also, maximum rotational speed for each rotor is limited.

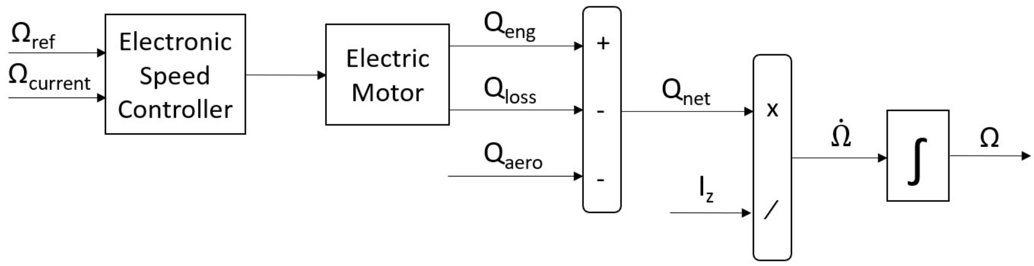

Figure 3.8: Block diagram of rotor dynamics

$$Q_{loss} = (0.01)\Omega_{current} \tag{3.25}$$

The electronic speed controller in Fig. 3.8 is a proportional integral (PI) controller that amplifies the rotational speed error and generates torque for the motor. Related block diagram is shown in Fig. 3.9 where "0.2" is the proportional gain and "0.1" is the integral gain of the controller. Motors are modelled such that they cannot provide negative torque and can only provide limited amount of torque which is 200 lb.ft.

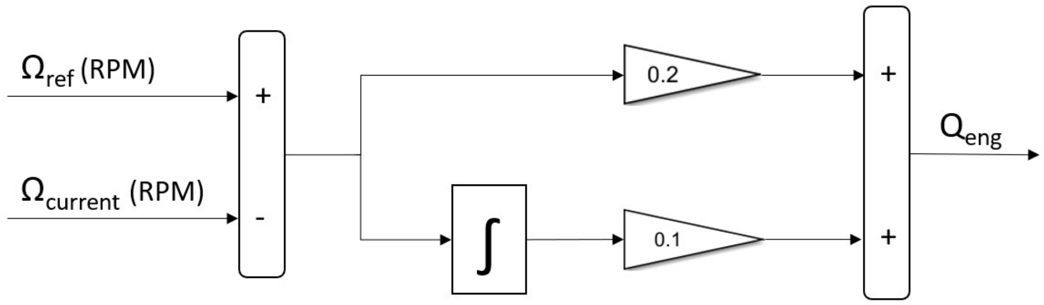

Figure 3.9: Block diagram of rotor dynamics

3.2.3 Fuselage Model

The fuselage is modelled so that it generates only forces in three body-axis directions. Each force is modelled using a flat plate drag area for drag. Dimensions of the fuselage are given in Table 3.3.

Parameter	**Value**
Length	5 m
Height	2 m
Width	2 m

Table 3.3: Fuselage Dimensions

From Table 3.3, cross-sectional areas are $4\,\mathrm{m}^2$, $10\,\mathrm{m}^2$, $10\,\mathrm{m}^2$ in yz-plane, xz-plane, xy-plane, respectively. By using these values, fuselage forces are calculated as following:

$$F_x = -\frac{1}{2}\rho u^2 S_{yz} K_x \tag{3.26}$$

$$F_y = -\frac{1}{2}\rho v^2 S_{xz} K_y \tag{3.27}$$

$$F_z = -\frac{1}{2}\rho w^2 S_{xy} K_z \tag{3.28}$$

where $\mathrm{K_x},\ \mathrm{K_y},\ \mathrm{K_z}$ are the flat plate drag area parameters and "$\mathrm{K_x} = \mathrm{K_y} = \mathrm{K_z} = 0.2$".

3.2.4 Atmosphere Model

Basics of the atmosphere model is described in this section. The model provides data of ambient air temperature, ambient barometric pressure and air density. Air density is the major output that is used in the simulation because it is included in dynamic pressure calculation. Dynamic pressure is used for aerodynamic force and moment calculations which are the main driving force for the simulation propagation.

Atmosphere model should be initiated with an initial value of pressure altitude. Then, the ambient temperature is calculated as following:

$$T_{amb} = T_0 + \Delta_{ISA} - L h_{PA} \tag{3.29}$$

where "$\mathrm{T_0}$" is the sea level temperature, "Δ_{ISA}" is the deviation from ISA (International Standard Atmosphere) temperature at given pressure altitude, "L" is the temperature lapse rate and "$\mathrm{h_{PA}}$" is the pressure altitude.

The ambient pressure calculation is given by:

$$P_{amb} = P_0 (1 - \frac{L h_{PA}}{T_0})^{\frac{gM}{RL}} \tag{3.30}$$

where "P_0" is the sea level pressure, "g" is the gravitational acceleration, "M" is the molar mass of dry air and "R" is the ideal gas constant.

"Δ_{ISA}" is taken as zero in the entire study, and values of the parameters in Eqs. (3.29) and (3.30) are listed in Table 3.4.

Finally, air density is calculated in Eq. (3.31).

$$\rho = \frac{P_{amb}M}{T_{amb}R} \tag{3.31}$$

Parameter	**Unit**	**Value**
T_0	Celsius	15
P_0	kPa	101.325
L	Kelvin/m	0.0065
M	kg/mol	0.0289654
R	J/(mol.Kelvin)	8.31447
g	$kg.m/s^2$	9.81

Table 3.4: Atmospheric model parameters

3.2.5 6-DoF Equations of Motion

The simulation is propagated based on the equations of motion written in 6-degrees-of-freedom. First, forces and moments generated from the aircraft components are added-up and total force and moment vectors are obtained with respect to the body-axis frame (Fig. 3.3). Then, translational accelerations are calculated by using Eqs. (3.32) to (3.34) and angular accelerations are calculated by using Eqs. (3.35) to (3.37).

$$\dot{U} = rV - qW + \frac{F_x}{m} - \{g\sin(\theta)\} \tag{3.32}$$

$$\dot{V} = pW - rU + \frac{F_y}{m} + \{g\cos(\theta)\sin(\phi)\} \tag{3.33}$$

$$\dot{W} = qU - pV + \frac{F_z}{m} + \{g\cos(\theta)\cos(\phi)\} \tag{3.34}$$

$$\dot{p} = \frac{M_x}{I_{xx}} + (I_{yy} - I_{zz})\frac{qr}{I_{xx}} \tag{3.35}$$

$$\dot{q} = \frac{M_y}{I_{yy}} + (I_{zz} - I_{xx})\frac{rp}{I_{yy}} \tag{3.36}$$

$$\dot{r} = \frac{M_z}{I_{zz}} + (I_{xx} - I_{yy})\frac{pq}{I_{zz}} \tag{3.37}$$

Parameters of the equations of motion are explained in the following list:

- $\{F_x, F_y, F_z\}$: Total force vectors with respect to the body-axis frame [Newton]
- $\{M_x, M_y, M_z\}$: Total moment vectors with respect to the body-axis frame [Newton]
- $\{U, V, W\}$: Translational velocities with respect to the body-axis frame [m/s]
- $\{p, q, r\}$: Angular velocities with respect to the body-axis frame [rad/s]
- $\{\phi, \theta\}$: Euler roll angle and pitch angle [rad]
- $\{I_{xx}, I_{yy}, I_{zz}\}$: Moment of inertias with respect to the body-axis frame $[\mathrm{kg.m^2}]$ (see Appendix-A.1)
- **m**: Mass [kg] (see Appendix-A.1)
- **g**: Gravitational acceleration $[\mathrm{kg.m/s^2}]$

3.2.6 Autopilot Design

An autopilot is designed for performing simulation tests with the eVTOL aircraft. The results are shown in Chapter-4. It is also used for trimming the aircraft to obtain steady-state conditions for analysis. The controller consists of PID (Proportional-Integral-Derivative) and PI (Proportional-Integral) controllers that are designed by gain tuning in order to operate in various flight conditions successfully. Block diagrams representing the controller structure are shown in Figs. 3.10 and 3.11. In the figures, subscript "e" represents error terms, subscript "ref" represents reference values, "δ" represents control inputs and "h" represents the altitude. For the remaining parameters, see item list in Section-3.2.5.

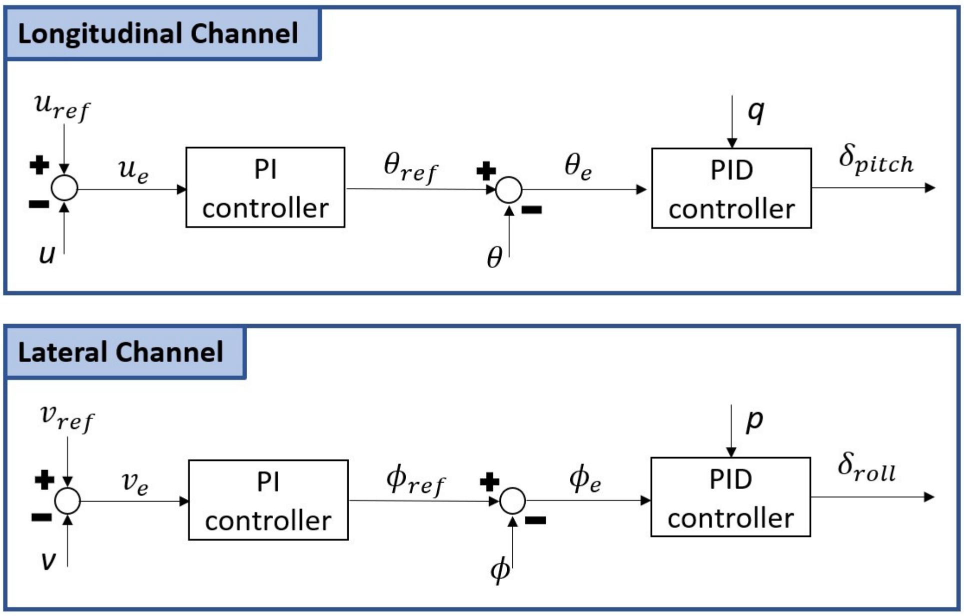

Figure 3.10: Controller block diagram of longitudinal and lateral channels

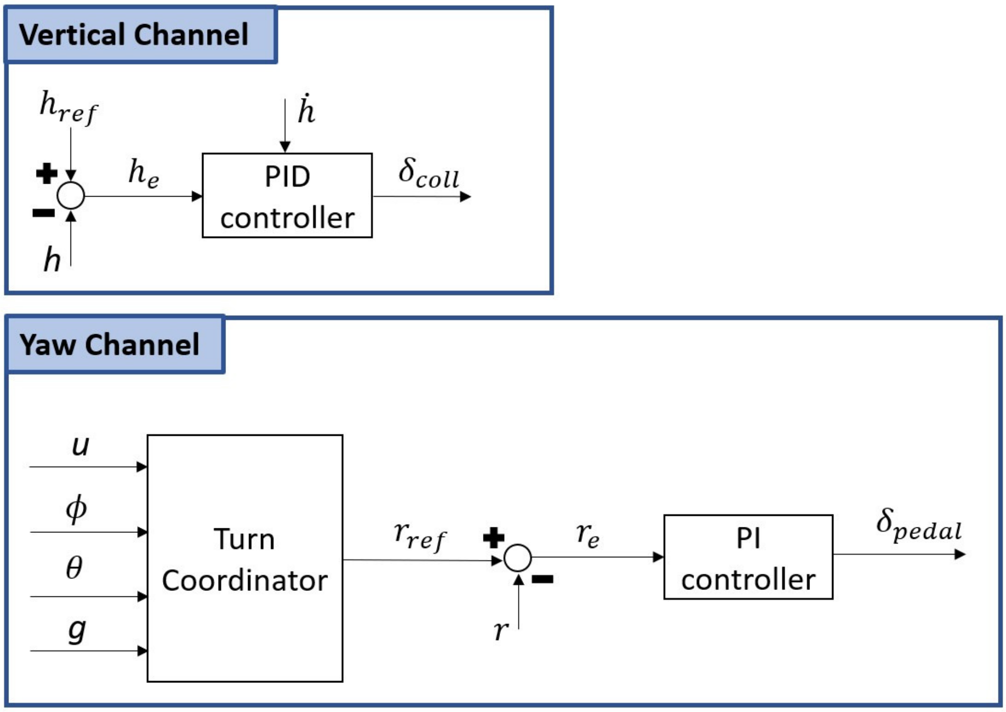

Figure 3.11: Controller block diagram of heave and yaw channels

Controller gains are listed in Appendix-A.7. And, yaw rate reference generated by the turn coordinator in Fig. 3.11 is expressed in Eq. (3.38). The turn coordinator starts to work above 20 knots of forward velocity.

$$r_{ref} = \frac{g \sin(\phi) \cos(\theta)}{u} \tag{3.38}$$

CHAPTER 4

SIMULATION RESULTS

4.1 Introduction

In this chapter, designed flight tests in simulation are conducted on the conceptual eVTOL aircraft of Chapter-3.2 with the implementation of the proposed control method in Chapter-2. Dynamics of the simulation environment where simulations performed are included in Chapter-3.2. This chapter consists of three sections. Firstly in Section-4.2, steady-state hover condition is analysed by comparing nominal flight condition and rotor failure condition. The purpose is to demonstrate the input re-distribution of Chapter-2.4. In Section-4.3, transient flight from hover to forward flight is performed. Then the same simulation is conducted with another vehicle with a different rotor speed limit. By comparing those tests, rotor saturation avoidance methods of Chapter-2.3 are demonstrated. In the final section (Section-4.4), various rotor failure scenarios are considered and tested on the aircraft model. The purpose of these simulations is to demonstrate the safe operation in case of rotor failure with the proposed control method.

Sign convention of pilot control inputs that are used in the analysis of this chapter is provided in Fig. 4.1.

4.2 Trim Analysis

Trim conditions of the aircraft are found by using the autopilot which is explained in Chapter-3.2.6. The aircraft is trimmed to hover with four combinations of operating rotor distribution.

Control input	Input direction	Sign convention	Interval
Roll cyclic	Right	+	[-1, 1]
Roll cyclic	Left	-	
Pitch cyclic	Up	+	[-1, 1]
Pitch cyclic	Down	-	
Pedal	Right	+	[-1, 1]
Pedal	Left	-	
Collective	Up	+	[0, 1]
Collective	Down	-	

Figure 4.1: Pilot control input sign convention

As a start, nominal hover trim condition is obtained where all rotors are operating (Section-4.2.1). The nominal trim condition is used as reference for comparison with rotor failure cases.

In case-1 (Section-4.2.2), four rotors are failed and the aircraft is trimmed to hover in this condition. Failed rotor positions are symmetrical with respect to each other (Fig. 4.2). The objective is to observe the collective control response.

In case-2 (Section-4.2.3), four rotors are failed where all of them rotate in the same direction and their positions are symmetrical with respect to each other (Fig. 4.3). Then the aircraft is trimmed to hover in this condition. The objective is to observe the yaw control response.

In case-3 (Section-4.2.4), four rotors are failed from the same quarter of the vehicle (Fig. 4.4). Then the aircraft is trimmed to hover in this condition. The objective is to observe the behaviour in roll and pitch axes.

In all cases explained above, two vehicles are compared:

- *Vehicle-1*: Inputs are not re-distributed.
- *Vehicle-2*: Inputs are re-distributed in case of rotor failure according to method described in Chapter-2.4.

Nominal rotor speed is 4500 RPM in all cases.

4.2.1 Nominal Operation

Trim results are shown in Table 4.1 and the corresponding rotor speeds are shown in Table 4.2. Since all rotor positions are symmetrical with respect to the C.G. of the vehicle, trim values of attitude angles and control positions in three body-frame axes (roll, pitch, yaw) are all zero. Only collective control input is significant in hover for lift generation.

Parameter	Unit	Value
Altitude	ft	1000.00
ΔISA	-	0.00
Longitudinal velocity in body frame (U)	ft/s	0.00
Lateral velocity in body frame (V)	ft/s	0.00
Normal velocity in body frame (W)	ft/s	0.00
Vertical Speed	ft/min	0.00
Roll angle (ϕ)	deg	0.00
Pitch angle (θ)	deg	0.00
Roll cyclic input	norm	0.00
Pitch cyclic input	norm	0.00
Pedal input	norm	0.00
Collective input	norm	0.57

Table 4.1: Nominal hover trim results

Rotor Number	Rotor Speed (%)	Rotor Number	Rotor Speed (%)
No: 1	55.5	No: 11	55.5
No: 2	55.5	No: 12	55.5
No: 3	55.5	No: 13	55.5
No: 4	55.5	No: 14	55.5
No: 5	55.5	No: 15	55.5
No: 6	55.5	No: 16	55.5
No: 7	55.5	No: 17	55.5
No: 8	55.5	No: 18	55.5
No: 9	55.5	No: 19	55.5
No: 10	55.5	No: 20	55.5

Table 4.2: Rotor speeds of nominal hover trim

4.2.2 Case-1: Lift Compensation

In this simulation, rotors with the following numbers are intentionally failed: 3, 8, 13, 18 (Fig. 4.2).

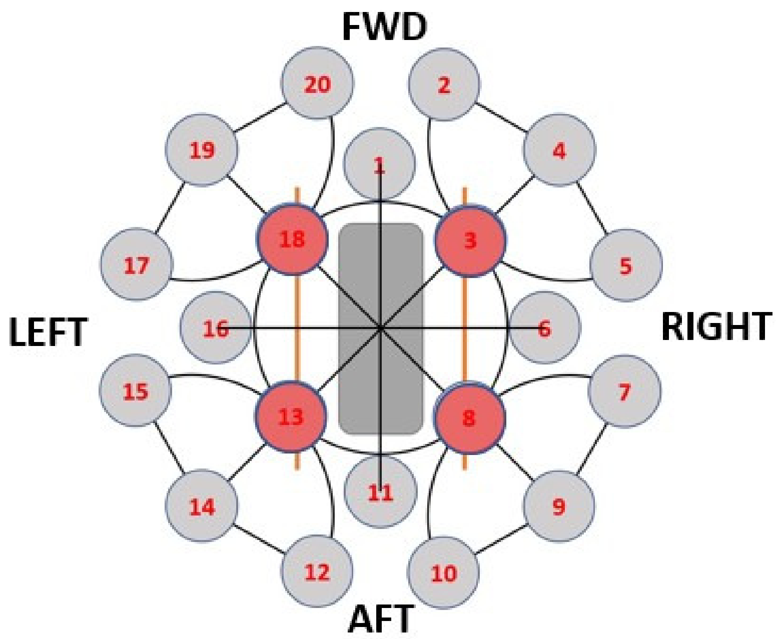

Figure 4.2: Failed rotors of case-1

Trim results of Vehicle-1 are shown in Table 4.3 and the corresponding rotor speeds are shown in Table 4.4.

Trim results of Vehicle-2 are shown in Table 4.5 and the corresponding rotor speeds are shown in Table 4.6.

Parameter	Unit	Value
Altitude	ft	1000.00
ΔISA	-	0.00
Longitudinal velocity in body frame (U)	ft/s	0.00
Lateral velocity in body frame (V)	ft/s	0.00
Normal velocity in body frame (W)	ft/s	0.00
Vertical Speed	ft/min	0.00
Roll angle (ϕ)	deg	0.00
Pitch angle (θ)	deg	0.00
Roll cyclic input	norm	0.00
Pitch cyclic input	norm	0.00
Pedal input	norm	0.00
Collective input	norm	0.77

Table 4.3: Hover trim results of case-1 for Vehicle-1

Rotor Number	Rotor Speed (%)	Rotor Number	Rotor Speed (%)
No: 1	62.0	No: 11	62.0
No: 2	62.0	No: 12	62.0
No: 3	0.0	No: 13	0.0
No: 4	62.0	No: 14	62.0
No: 5	62.0	No: 15	62.0
No: 6	62.0	No: 16	62.0
No: 7	62.0	No: 17	62.0
No: 8	0.0	No: 18	0.0
No: 9	62.0	No: 19	62.0
No: 10	62.0	No: 20	62.0

Table 4.4: Rotor speeds of hover trim of case-1 for Vehicle-1

Parameter	Unit	Value
Altitude	ft	1000.00
ΔISA	-	0.00
Longitudinal velocity in body frame (U)	ft/s	0.00
Lateral velocity in body frame (V)	ft/s	0.00
Normal velocity in body frame (W)	ft/s	0.00
Vertical Speed	ft/min	0.00
Roll angle (ϕ)	deg	0.00
Pitch angle (θ)	deg	0.00
Roll cyclic input	norm	0.00
Pitch cyclic input	norm	0.00
Pedal input	norm	0.00
Collective input	norm	0.63

Table 4.5: Hover trim results of case-1 for Vehicle-2

Rotor Number	Rotor Speed (%)	Rotor Number	Rotor Speed (%)
No: 1	62.0	No: 11	62.0
No: 2	62.0	No: 12	62.0
No: 3	0.0	No: 13	0.0
No: 4	62.0	No: 14	62.0
No: 5	62.0	No: 15	62.0
No: 6	62.0	No: 16	62.0
No: 7	62.0	No: 17	62.0
No: 8	0.0	No: 18	0.0
No: 9	62.0	No: 19	62.0
No: 10	62.0	No: 20	62.0

Table 4.6: Rotor speeds of hover trim of case-1 for Vehicle-2

In both vehicles, attitude angles and all controls, except the collective, remain zero

(Tables 4.3 and 4.5) because positions of failed rotors are symmetrical with respect to the C.G. of the aircraft and their rotation directions compensate their yaw effects.

The rotor speed distributions of the two vehicles (Tables 4.4 and 4.6) are the same. Rotor speeds of both vehicles are higher than the nominal operation of Section-4.2.1, Table 4.2. This is expected because of the lack of lift as the thrust of failed rotors should be compensated in order to keep hovering.

The difference between the two vehicles is the position of the collective control. Inputs are not re-distributed in Vehicle-1, then the required rotor speeds result from the increase in collective control which becomes 0.77 (Table 4.4). Whereas, it is 0.57 (Table 4.1) in the nominal operation (Section-4.2.1).

However in Vehicle-2, inputs are re-distributed. The rotor speeds are set by this system for lift compensation. Therefore there is no need to increase the collective position. No change in collective is expected with the re-distribution algorithm. Since the eVTOL aircraft is non-linearly modelled, there is a little deviation in the collective control (0.63, in Table 4.6) compared to collective position of the nominal hover case (0.57, in Table 4.1) in Section-4.2.1.

See Tables 4.15 and 4.16 for overall comparison of the simulations conducted in Section-4.2.

4.2.3 Case-2: Yaw Compensation

In this simulation, rotors with the following numbers are intentionally failed: 6, 8, 16, 18 (Fig. 4.3). All of the failed rotors rotate counter-clockwise direction in the nominal operation.

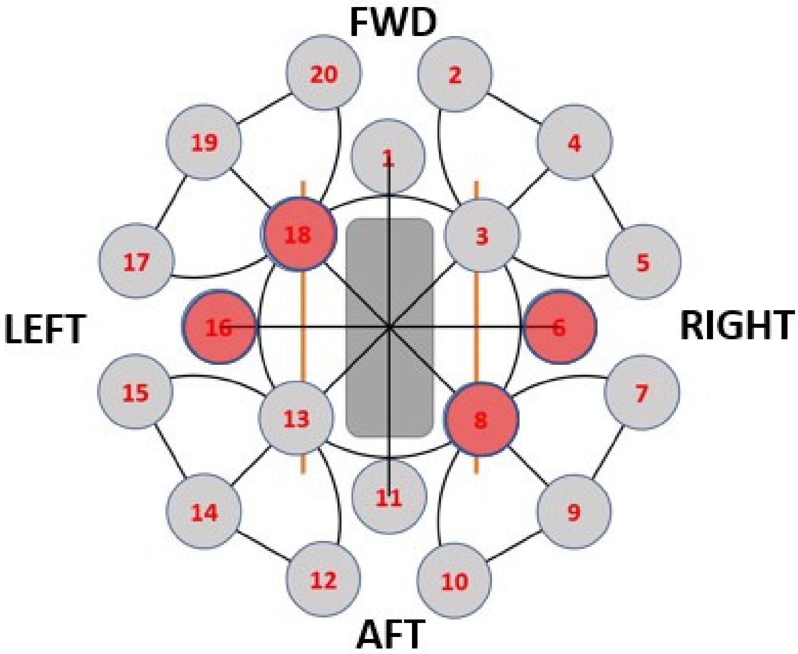

Figure 4.3: Failed rotors of case-2

Trim results of Vehicle-1 are shown in Table 4.7 and the corresponding rotor speeds are shown in Table 4.8.

Trim results of Vehicle-2 are shown in Table 4.9 and the corresponding rotor speeds are shown in Table 4.10.

Parameter	Unit	Value
Altitude	ft	1000.00
ΔISA	-	0.00
Longitudinal velocity in body frame (U)	ft/s	0.00
Lateral velocity in body frame (V)	ft/s	0.00
Normal velocity in body frame (W)	ft/s	0.00
Vertical Speed	ft/min	0.00
Roll angle (ϕ)	deg	0.00
Pitch angle (θ)	deg	0.00
Roll cyclic input	norm	0.00
Pitch cyclic input	norm	0.00
Pedal input	norm	0.63
Collective input	norm	0.87

Table 4.7: Hover trim results of case-2 for Vehicle-1

Rotor Number	Rotor Speed (%)	Rotor Number	Rotor Speed (%)
No: 1	52.8	No: 11	52.8
No: 2	74.9	No: 12	74.9
No: 3	52.8	No: 13	52.8
No: 4	74.9	No: 14	74.9
No: 5	52.8	No: 15	52.8
No: 6	0	No: 16	0
No: 7	52.8	No: 17	52.8
No: 8	0	No: 18	0
No: 9	52.8	No: 19	52.8
No: 10	74.9	No: 20	74.9

Table 4.8: Rotor speeds of hover trim of case-2 for Vehicle-1

Parameter	Unit	Value
Altitude	ft	1000.00
ΔISA	-	0.00
Longitudinal velocity in body frame (U)	ft/s	0.00
Lateral velocity in body frame (V)	ft/s	0.00
Normal velocity in body frame (W)	ft/s	0.00
Vertical Speed	ft/min	0.00
Roll angle (ϕ)	deg	0.00
Pitch angle (θ)	deg	0.00
Roll cyclic input	norm	0.00
Pitch cyclic input	norm	0.00
Pedal input	norm	0.16
Collective input	norm	0.66

Table 4.9: Hover trim results of case-2 for Vehicle-2

Rotor Number	Rotor Speed (%)	Rotor Number	Rotor Speed (%)
No: 1	52.8	No: 11	52.8
No: 2	74.9	No: 12	74.9
No: 3	52.8	No: 13	52.8
No: 4	74.9	No: 14	74.9
No: 5	52.8	No: 15	52.8
No: 6	0.0	No: 16	0.0
No: 7	52.8	No: 17	52.8
No: 8	0.0	No: 18	0.0
No: 9	52.8	No: 19	52.8
No: 10	74.9	No: 20	74.9

Table 4.10: Rotor speeds of hover trim of case-2 for Vehicle-2

In both vehicles attitude angles, roll cyclic and pitch cyclic controls remain zero (Tables 4.7 and 4.9) because positions of failed rotors are symmetrical with respect to the C.G. of the aircraft.

The rotor speed distributions of the two vehicles (Tables 4.8 and 4.10) are the same because they are both resulted from the Blended-Inverse. Flight control system updated the rotor speed distribution to make yaw moment zero.

The difference between the two vehicle is position of the collective and pedal controls. Inputs are not re-distributed in Vehicle-1, then the required rotor speeds result from the higher amount of pedal control which becomes 0.63 (Table 4.7). Whereas, it is 0 (centred position) in the nominal operation (Section-4.2.1, Table 4.1). Counter-clockwise rotated rotors create torque towards right. Thus, extra pedal input towards right is the expected result due to failed rotors. In the plant model positive pedal input provides yaw moment towards right (Fig. 4.1), then 63% positive increase in pedal control is meaningful. Also, collective increase of Vehicle-1 is observed because inputs are not re-distributed in this vehicle.

However in Vehicle-2, inputs are re-distributed and the rotor speeds are set by this system for lift and yaw moment compensation. Therefore there is no need to increase the collective and pedal with respect to nominal hover operation in Section-4.2.1. No change in controls is expected with the re-distribution algorithm. Since the eVTOL aircraft is non-linearly modelled, there is a little deviation in the pedal (0.16, in Table 4.9) and collective control (0.66, in Table 4.9) compared to corresponding controls of the nominal operation in Section-4.2.1, Table 4.1 where collective is 0.57 and pedal is 0 (centred position).

See Tables 4.15 and 4.16 for overall comparison of the simulations conducted in Section-4.2.

4.2.4 Case-3: Roll and Pitch Moment Compensation

In this simulation, rotors with the following numbers are intentionally failed: 1, 3, 4, 6 (Fig. 4.4). All of the failed rotors are located in the forward-right side of the aircraft.

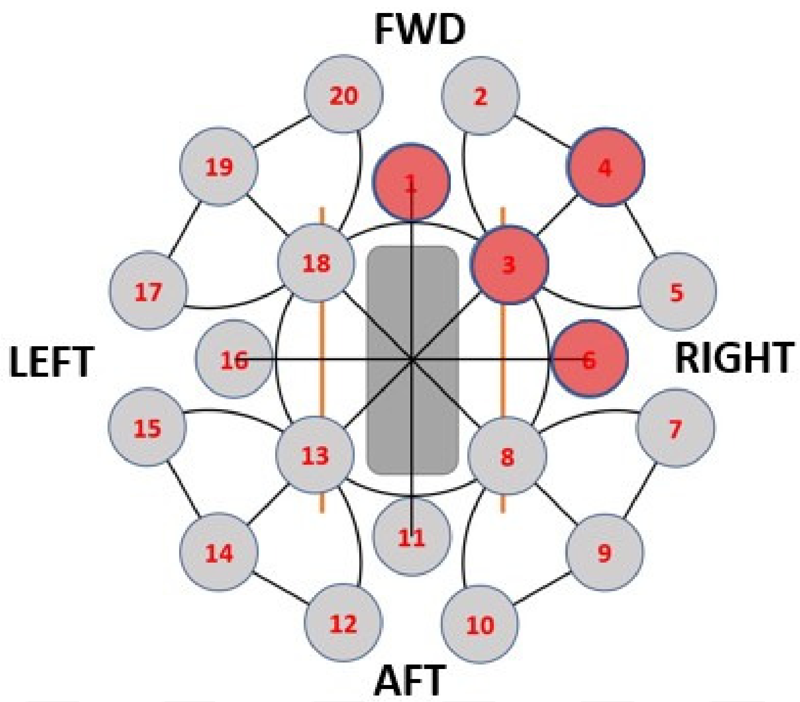

Figure 4.4: Failed rotors of case-3

Trim results of Vehicle-1 are shown in Table 4.11 and the corresponding rotor speeds are shown in Table 4.12.

Trim results of Vehicle-2 are shown in Table 4.13 and the corresponding rotor speeds are shown in Table 4.14.

Parameter	Unit	Value
Altitude	ft	1000.00
ΔISA	-	0.00
Longitudinal velocity in body frame (U)	ft/s	0.00
Lateral velocity in body frame (V)	ft/s	0.00
Normal velocity in body frame (W)	ft/s	0.00
Vertical Speed	ft/min	0.00
Roll angle (ϕ)	deg	0.00
Pitch angle (θ)	deg	0.00
Roll cyclic input	norm	-0.69
Pitch cyclic input	norm	0.69
Pedal input	norm	0.03
Collective input	norm	0.85

Table 4.11: Hover trim results of case-3 for Vehicle-1

Rotor Number	Rotor Speed (%)	Rotor Number	Rotor Speed (%)
No: 1	0	No: 11	57.0
No: 2	75.4	No: 12	51.6
No: 3	0	No: 13	56.3
No: 4	0	No: 14	49.1
No: 5	74.6	No: 15	50.3
No: 6	0	No: 16	57.9
No: 7	70.4	No: 17	56.1
No: 8	64.6	No: 18	64.5
No: 9	63.7	No: 19	63.6
No: 10	57.3	No: 20	71.1

Table 4.12: Rotor speeds of hover trim of case-3 for Vehicle-1

Parameter	Unit	Value
Altitude	ft	1000.00
ΔISA	-	0.00
Longitudinal velocity in body frame (U)	ft/s	0.00
Lateral velocity in body frame (V)	ft/s	0.00
Normal velocity in body frame (W)	ft/s	0.00
Vertical Speed	ft/min	0.00
Roll angle (ϕ)	deg	0.00
Pitch angle (θ)	deg	0.00
Roll cyclic input	norm	-0.04
Pitch cyclic input	norm	0.04
Pedal input	norm	0.00
Collective input	norm	0.65

Table 4.13: Hover trim results of case-3 for Vehicle-2

Rotor Number	Rotor Speed (%)	Rotor Number	Rotor Speed (%)
No: 1	0.0	No: 11	57.0
No: 2	75.4	No: 12	51.6
No: 3	0.0	No: 13	56.3
No: 4	0.0	No: 14	49.1
No: 5	74.6	No: 15	50.3
No: 6	0.0	No: 16	57.9
No: 7	70.4	No: 17	56.1
No: 8	64.6	No: 18	64.5
No: 9	63.7	No: 19	63.6
No: 10	57.3	No: 20	71.1

Table 4.14: Rotor speeds of hover trim of case-3 for Vehicle-2

The rotor speed distributions of the two vehicles (Tables 4.12 and 4.14) are the same because they are both resulted from the Blended-Inverse. Flight control system updated the rotor speed distribution to make resultant forces and moments to zero.

The difference between the two vehicles is position of the controls. Inputs are not re-distributed in Vehicle-1. Therefore, the required rotor speeds result from the increase in all of the controls (Table 4.11) with respect to the nominal operation of Section-4.2.1 (Table 4.1). Due to positions of the failed rotors, the aircraft has tendency to pitch-forward and roll-right, and also, it loses lift. As a result, control inputs of pitch-up, roll-left and collective-up are required which are observed in Table 4.11.

However in Vehicle-2, inputs are re-distributed and the rotor speeds are set by this system for lift and moment compensation. Therefore there is no need for increase in controls (see Table 4.13) with respect to nominal hover operation of Section-4.2.1, Table 4.1. No change in controls is expected with the re-distribution algorithm. Since the eVTOL aircraft is non-linearly modelled, there is a little deviation in all controls (Table 4.13) compared to controls of the nominal hover case of Section-4.2.1, Table 4.1.

See Tables 4.15 and 4.16 for overall comparison of the simulations conducted in Section-4.2.

Parameter	**Unit**	**Nominal Case**	**Case-1**	**Case-2**	**Case-3**
Altitude	ft	1000.00	1000.00	1000.00	1000.00
ΔISA	-	0.00	0.00	0.00	0.00
Longitudinal velocity in body frame (U)	ft/s	0.00	0.00	0.00	0.00
Lateral velocity in body frame (V)	ft/s	0.00	0.00	0.00	0.00
Normal velocity in body frame (W)	ft/s	0.00	0.00	0.00	0.00
Vertical Speed	ft/min	0.00	0.00	0.00	0.00
Roll angle (ϕ)	deg	0.00	0.00	0.00	0.00
Pitch angle (θ)	deg	0.00	0.00	0.00	0.00
Roll cyclic input	norm	0.00	0.00	0.00	-0.69
Pitch cyclic input	norm	0.00	0.00	0.00	0.69
Pedal input	norm	0.00	0.00	0.63	0.03
Collective input	norm	0.57	0.77	0.87	0.85

Table 4.15: Overall comparison of hover trim results for Vehicle-1

Parameter	Unit	Nominal Case	Case-1	Case-2	Case-3
Altitude	ft	1000.00	1000.00	1000.00	1000.00
ΔISA	-	0.00	0.00	0.00	0.00
Longitudinal velocity in body frame (U)	ft/s	0.00	0.00	0.00	0.00
Lateral velocity in body frame (V)	ft/s	0.00	0.00	0.00	0.00
Normal velocity in body frame (W)	ft/s	0.00	0.00	0.00	0.00
Vertical Speed	ft/min	0.00	0.00	0.00	0.00
Roll angle (ϕ)	deg	0.00	0.00	0.00	0.00
Pitch angle (θ)	deg	0.00	0.00	0.00	0.00
Roll cyclic input	norm	0.00	0.00	0.00	-0.04
Pitch cyclic input	norm	0.00	0.00	0.00	0.04
Pedal input	norm	0.00	0.00	0.16	0.00
Collective input	norm	0.57	0.63	0.66	0.65

Table 4.16: Overall comparison of hover trim results for Vehicle-2

4.3 Simulation in Manoeuvres

In this section, two simulation tests are conducted to demonstrate control saturation avoidance. To prevent rotor saturations, two methods described in Section-2.3 are used.

In "Test-1" (Section-4.3.1), Blended-Inverse modification method explained in Section-2.3.2 is used.

In "Test-2" (Section-4.3.2), weight matrix modification method explained in Section-2.3.1 is used.

Simulation procedure:
Two vehicles are compared in this section:

- *Vehicle-1*: Rotor rotational speed limit is 4500 RPM.
- *Vehicle-2*: rotor rotational speed limit is 2565 RPM.

The same flight manoeuvre is performed in the simulation for the two vehicles by using the autopilot described in Chapter-3.2.6. Then, results are compared in terms of handling qualities and flight performance.

The simulation starts from a steady hover trim condition at 1000 ft pressure altitude, then is accelerated to 50 knots of forward flight. Then, a coordinated turn manoeuvre with 45 degrees bank angle towards right is performed. Finally, the aircraft is decelerated until full stop in the air and trimmed back to hover condition. During the test, collective position of the aircraft is fixed at the trim value. The manoeuvres are performed aggressively so that there are higher amount of rotor speed deviations for a satisfactory comparison.

Hover trim condition at the beginning of the simulation is the same trim condition of Section-4.2.1. Values of the trim states can be read from the Table 4.1 and the corresponding rotor rotational speed distribution is shown at the Table 4.2.

4.3.1 Test-1: Rotor Saturation Avoidance with Blended-Inverse Modification

In this section, method of Section-2.3.2 is used where the Blended-Inverse equation is modified (Eq. (2.18)).

Results are shown in Figs. 4.5, 4.6, 4.7 and 4.8.

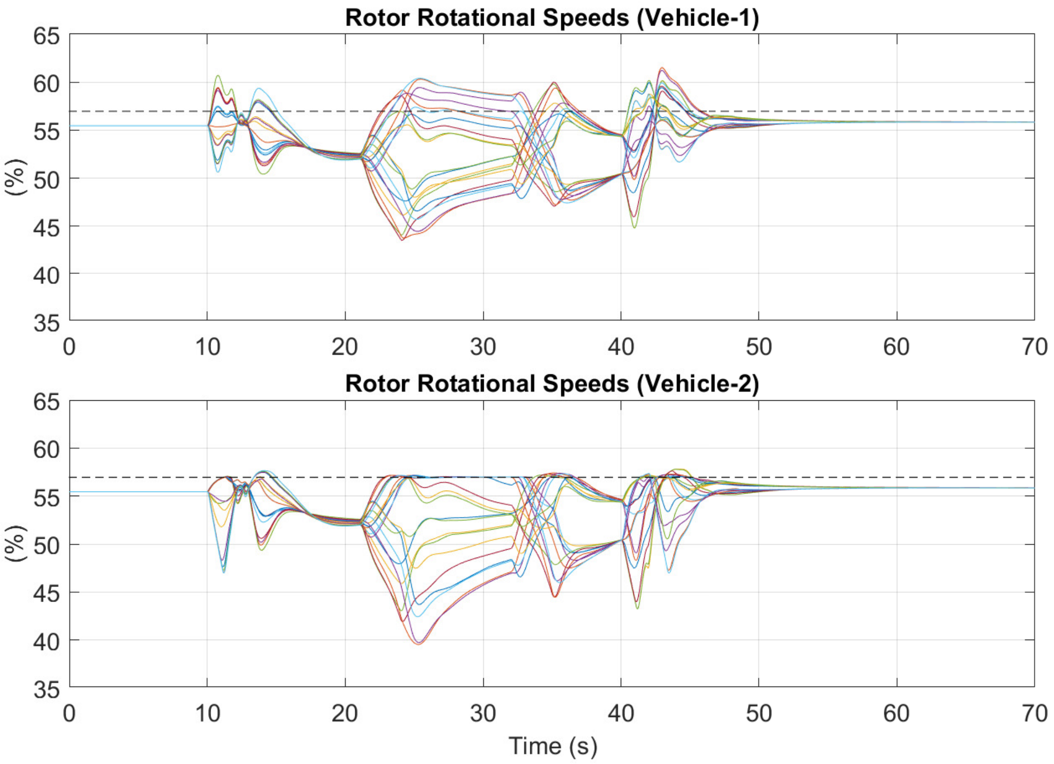

Figure 4.5: Rotor speed distribution comparison of test-1

Dash line in Fig.4.5 is the rotor speed limit of Vehicle-2 which is 57% (2565 RPM). For comparison it is also shown in the graph of Vehicle-1. By looking at the graph, the flight control system prevents rotors from exceeding the saturation limit.

In Fig.4.5, failed rotor speeds become zero in one second. It is not shown in the graph for closer visualization.

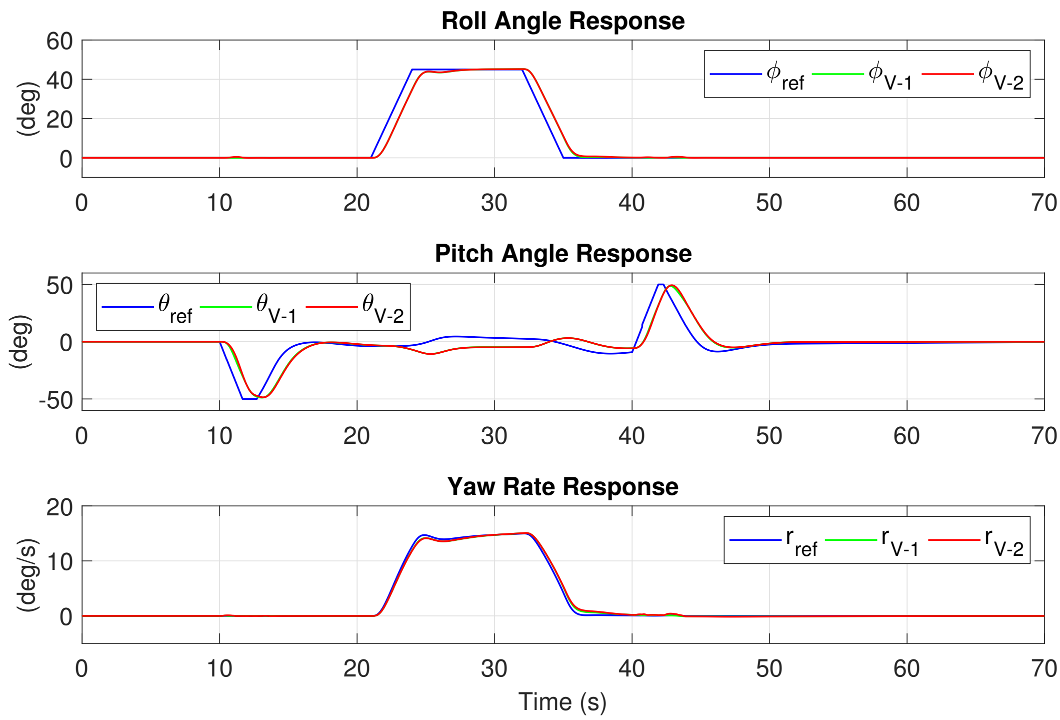

Figure 4.6: Attitude response comparison of test-1

In Fig. 4.6, blue lines are the reference state values generated by the autopilot in order to perform the simulation. It can be seen that flight control system safely controls the Vehicle-2 by limiting the rotor speeds, almost with the same flight performance of Vehicle-1.

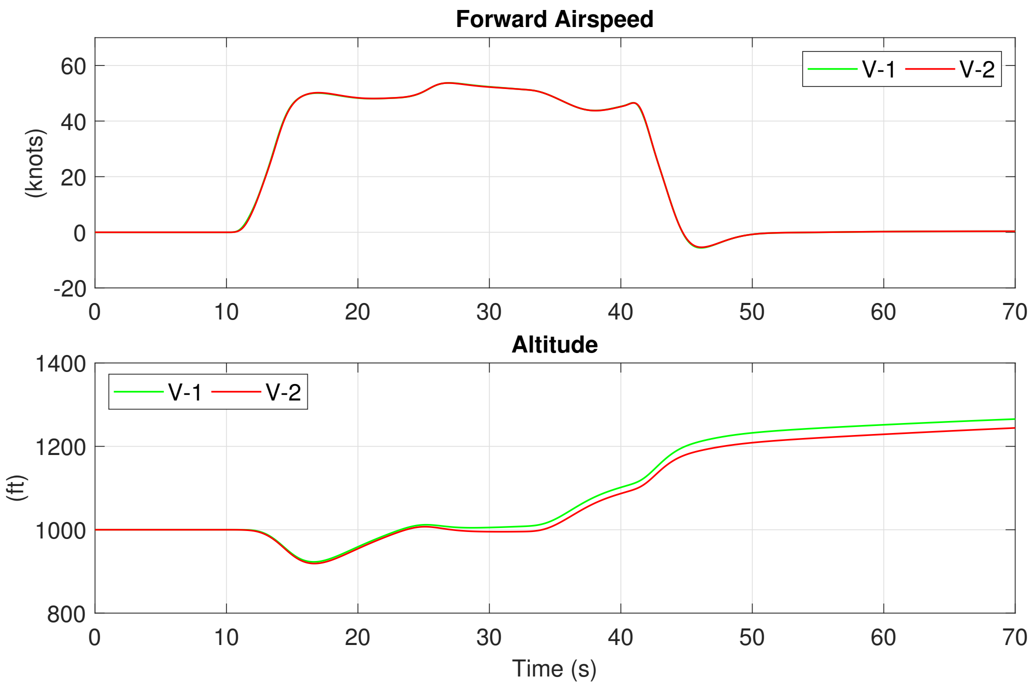

Figure 4.7: Airspeed and altitude comparison of test-1

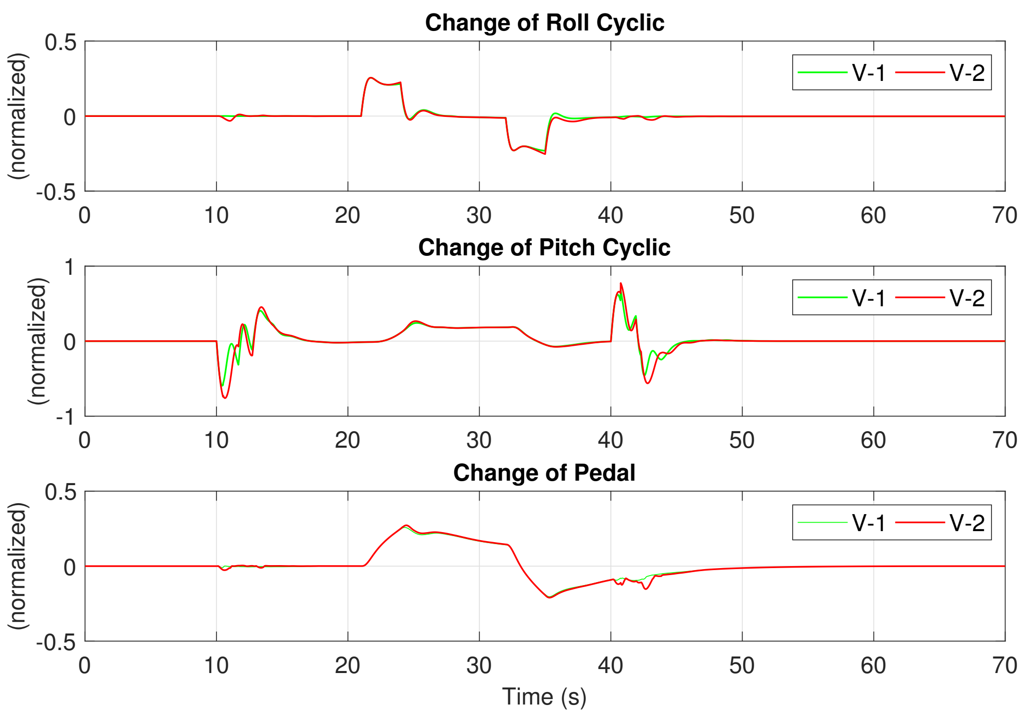

Figure 4.8: Control position comparison of test-1

Due to the rotor limitation, a little higher amount of controls are required for Vehicle-2 compared to Vehicle-1 (Fig. 4.8). The difference in controls can be seen most significantly in the pitch channel because in Vehicle-2, rotor speeds are limited mostly during pitching manoeuvres at low airspeeds.

4.3.2 Test-2: Rotor Saturation Avoidance with Weight Matrix Modification

In this section, method of Section-2.3.1 is used where the weight matrix of input is modified.

Results are shown in Figs. 4.9, 4.10, 4.11 and 4.12.

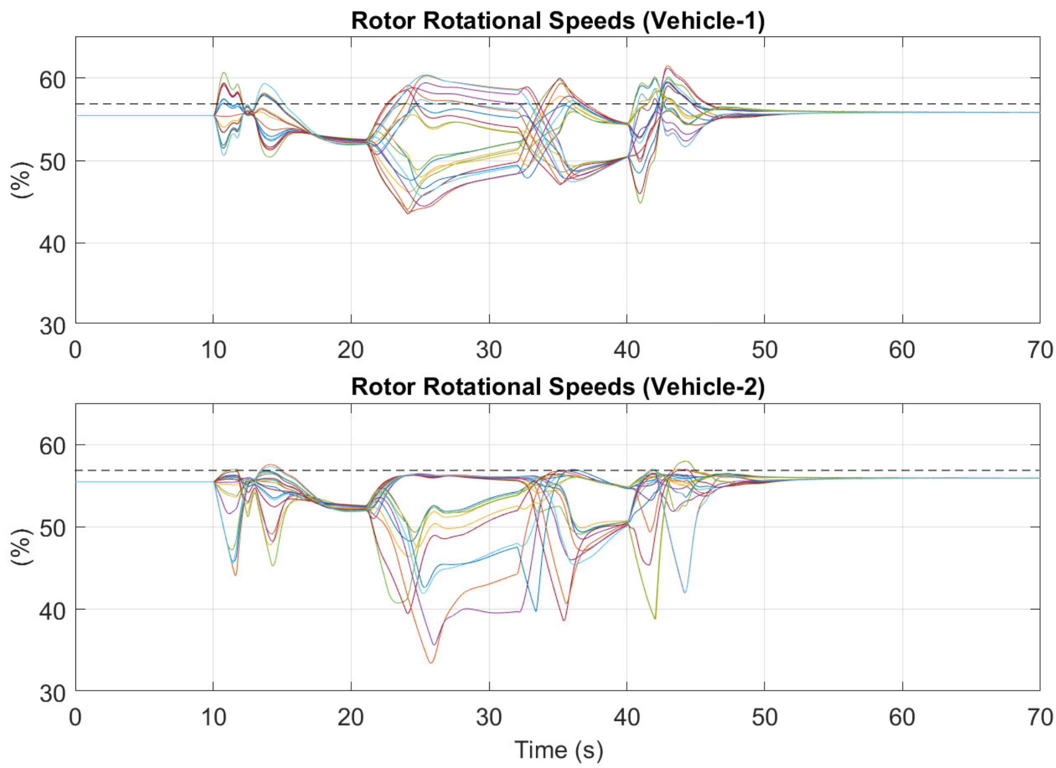

Figure 4.9: Rotor speed distribution comparison of test-2

In Fig.4.9, failed rotor speeds become zero in one second. It is not shown in the graph for closer visualization. From this graph, rotors are kept further away from saturation limit with this method compared to Blended-Inverse modification method (see Fig. 4.5).

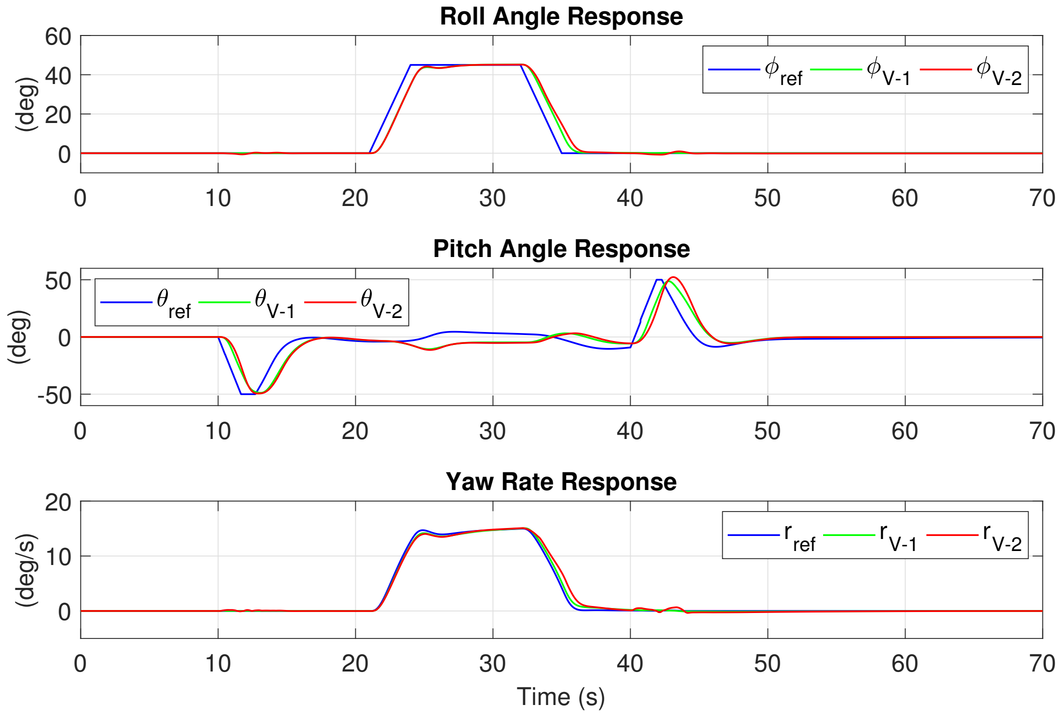

Figure 4.10: Attitude response comparison of test-2

In Fig. 4.10, blue lines are the reference state values generated by the autopilot in order to perform the simulation. It can be seen that flight control system safely controls Vehicle-2 by limiting the rotor speeds, almost with the same flight performance of Vehicle-1.

Weight matrix modification method gives a close dynamic response with the Blended-Inverse modification method.

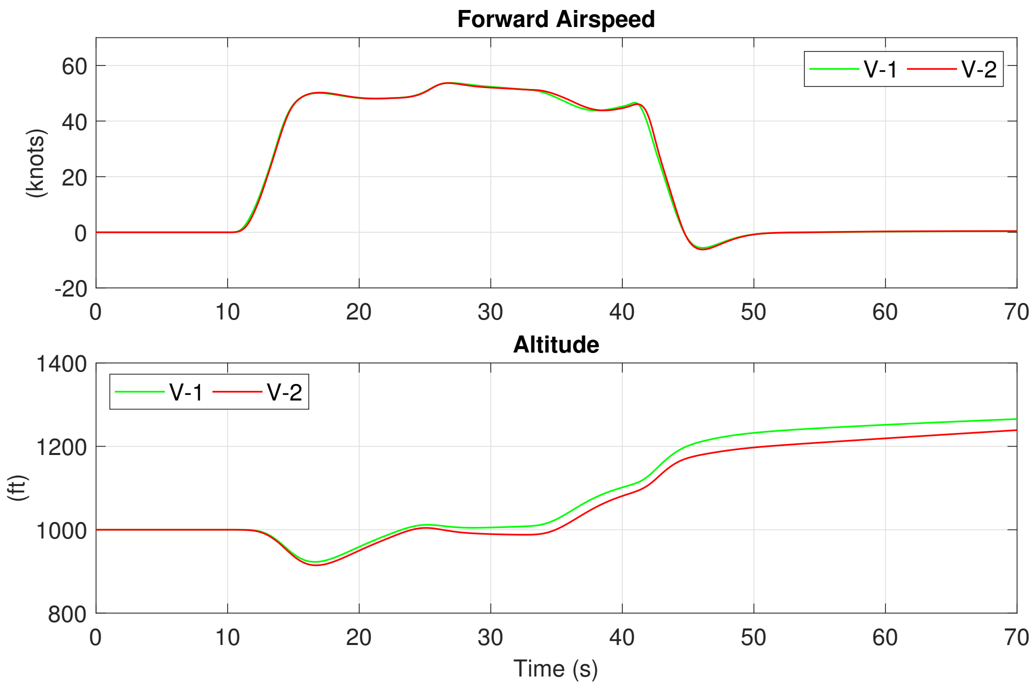

Figure 4.11: Airspeed and altitude comparison of test-2

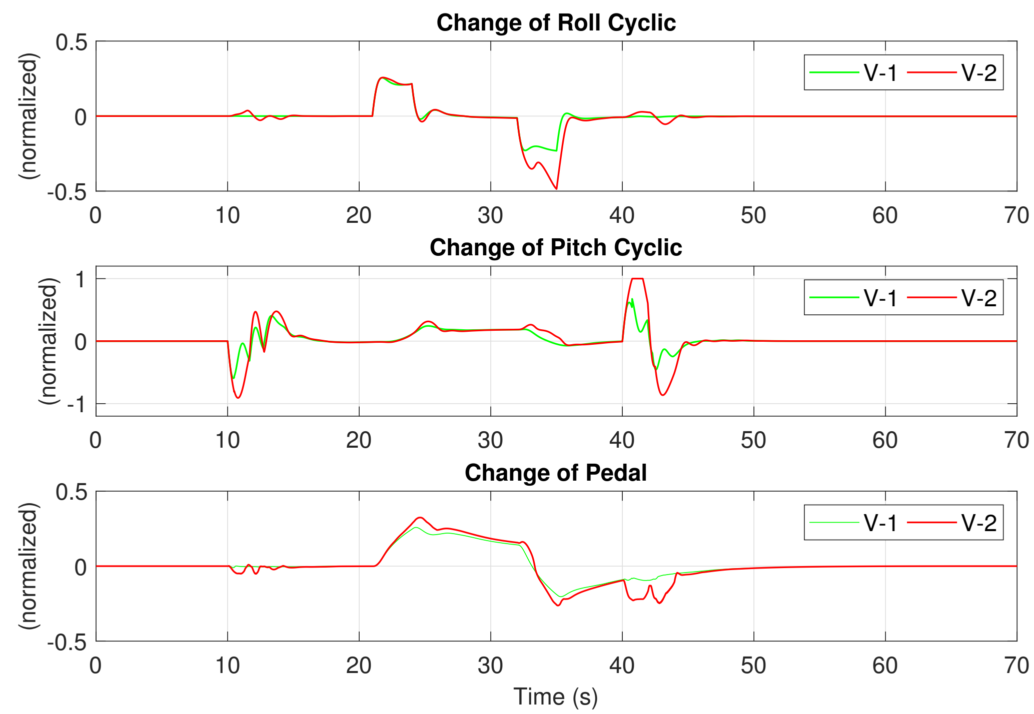

Figure 4.12: Control position comparison of test-2

By looking at Fig. 4.12, pilot control inputs are closer to saturation limits compared to Fig. 4.8 where Blended-Inverse modification method is used. This is due to more responsive output provided by weight matrix modification. Since rotors are kept further away from saturation limit with this method, pilot control inputs become more aggressive to perform the defined flight manoeuvre. This can also be seen in Fig. 4.10. Vehicle-2 follows reference attitude values a little bit more sluggish than the one in Section-4.3.1.

4.4 Control Allocation during Rotor Failure

In this section, three rotor failure scenarios are considered in the simulation environment. In each case, the autopilot (see Chapter-3.2.6) generates control commands in order to keep the aircraft in trim condition. All simulations are conducted at both hover and 60 knots of forward flight. Then, the results are evaluated.

In all cases, it takes one second for a single rotor to fail. Also, there is no rotor failure detection system. There are manual switches for each rotor in order to activate a failure.

Nominal rotational speed of rotors is defined as 4500 RPM for all cases.

Case-1:
Five rotors are randomly failed one by one at intervals of 15 seconds (Fig. 4.13).

The simulation is conducted for two different vehicles:

- *Vehicle-1*: Rotor rotational speed limit is 4500 RPM (100%).
- *Vehicle-2*: Rotor rotational speed limit is 2925 RPM (65%).

The focus is to demonstrate that inputs are re-distributed on-line following the rotor failures while it avoids rotor saturations at the same time. The method described in Section-2.3.2 is used in both vehicles for saturation avoidance.

Case-2:
Five rotors are intentionally failed from the same quarter of the aircraft at intervals of

15 seconds (Fig. 4.19).

The simulation is conducted for two different vehicles:

- *Vehicle-1*: Inputs are re-distributed in case of rotor failure according to method described in Chapter-2.4.
- *Vehicle-2*: Inputs are not re-distributed.

The purpose is to demonstrate the on-line operation of input re-distribution explained in Chapter-2.4.

Case-3:
Ten rotors are randomly failed one by one at intervals of 15 seconds (Fig. 4.25).

The simulation is conducted for two different vehicles:

- *Vehicle-1*: Inputs are re-distributed in case of rotor failure according to method described in Chapter-2.4.
- *Vehicle-2*: Inputs are not re-distributed.

4.4.1 Hover

For the simulations conducted in this section, hover trim condition is the same as with Section-4.2.1. Values of the trim states can be read from the Table 4.1 and the corresponding rotor rotational speed distribution can be found in the Table 4.2.

4.4.1.1 Failure Case-1

In this simulation, rotors with the following numbers are failed, respectively: 8, 9, 17, 14, 18 (Fig. 4.13). These numbers are randomly selected.

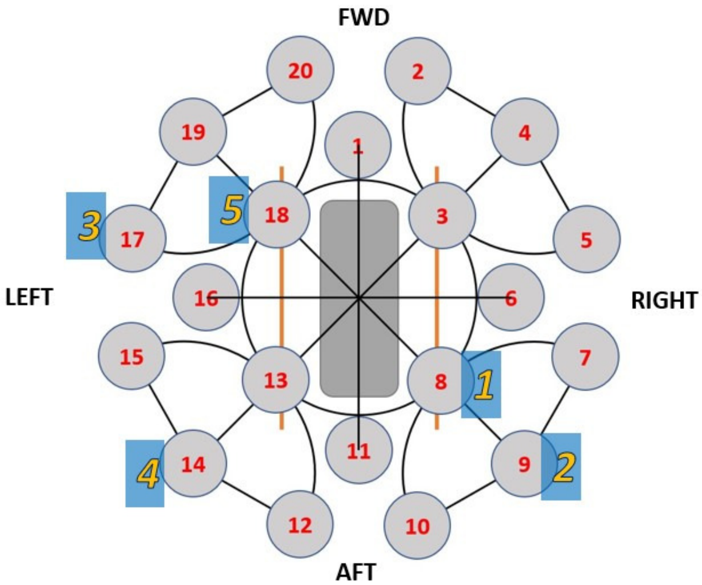

Figure 4.13: Failed rotors of case-1 and their orders

The results of the simulation are shown in Figs. 4.14, 4.15, 4.16, 4.17 and 4.18.

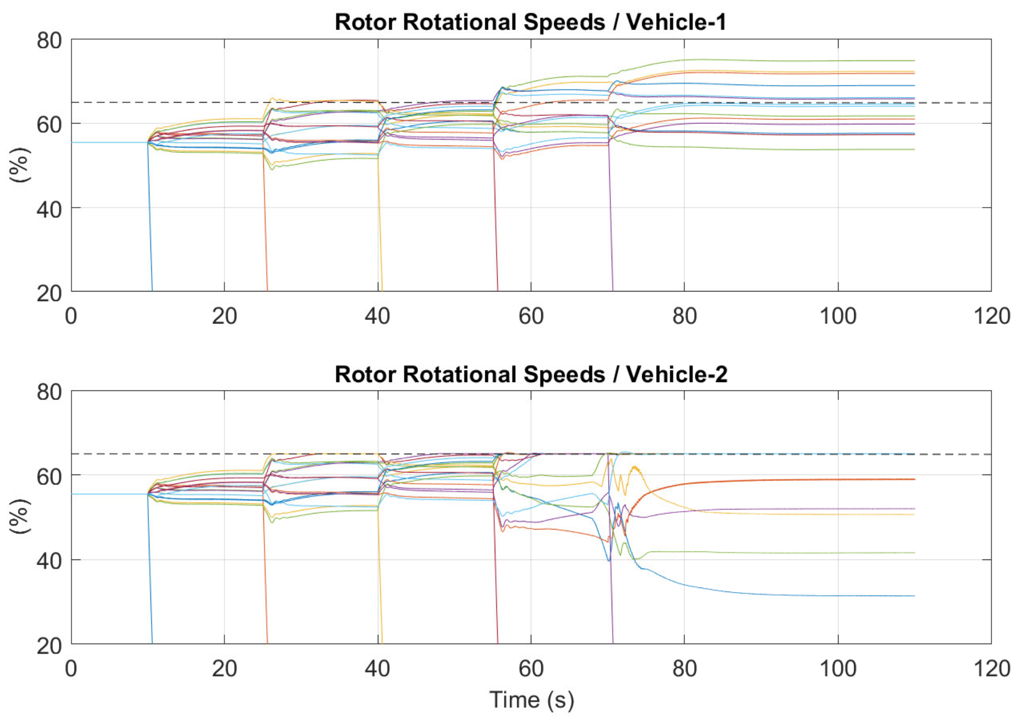

Figure 4.14: Rotor speed distribution of simulation

In Fig. 4.14, dashed line represents the rotor speed limit of Vehicle-2. For comparison, it is also plotted to the graph of Vehicle-1. It can be clearly seen from the figure that the control system avoids rotors from excessing the limit. In Vehicle-2, the control system works to provide desired control force by using the rotors that are not saturated. There are six rotors that are limited due to the limit application and it can be seen from the Fig. 4.14.

In Fig.4.14, failed rotor speeds become zero in one second. It is partly shown in the graph to provide closer visualization of the operating rotors.

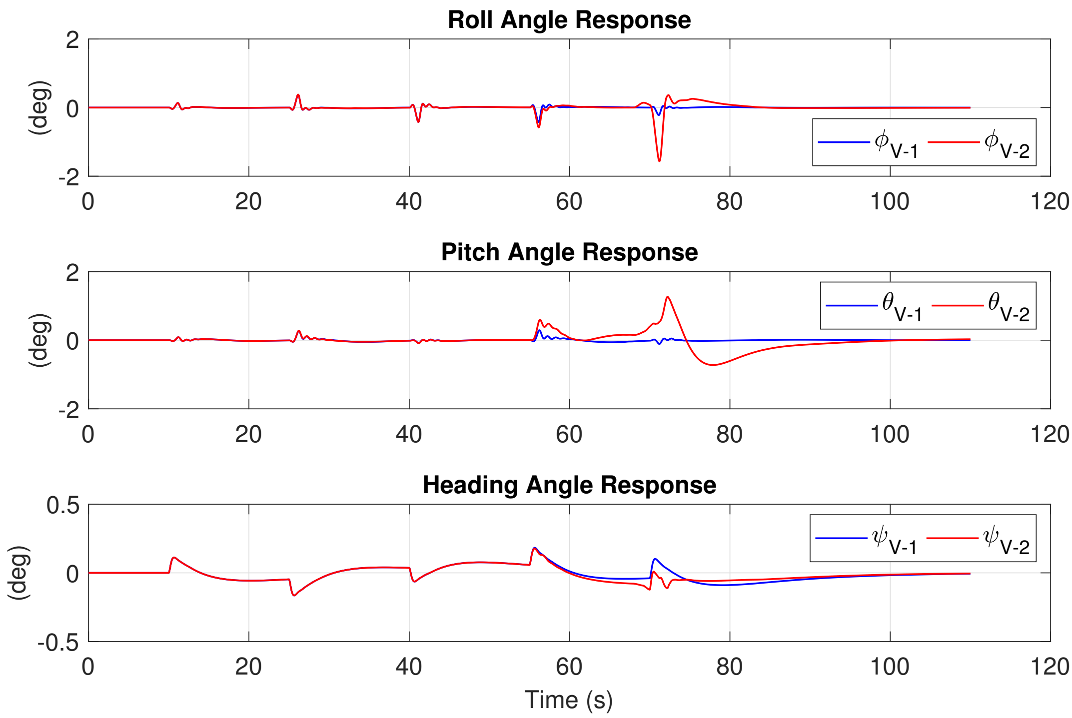

Figure 4.15: Euler angles of simulation

Effects of rotor saturations can be seen in the resultant attitude angles shown in Fig. 4.15. There is no difference until the failure of the 4^{th} rotor at 55^{th} second because rotors start saturating after this point. In parallel, magnitude of controls become larger due to lack of rotor thrusts (Figs. 4.16, 4.17). Collective control hits the upper limit because sufficient lift cannot be generated in this condition while keeping the hover attitude. Loss of altitude can be seen in Fig. 4.18.

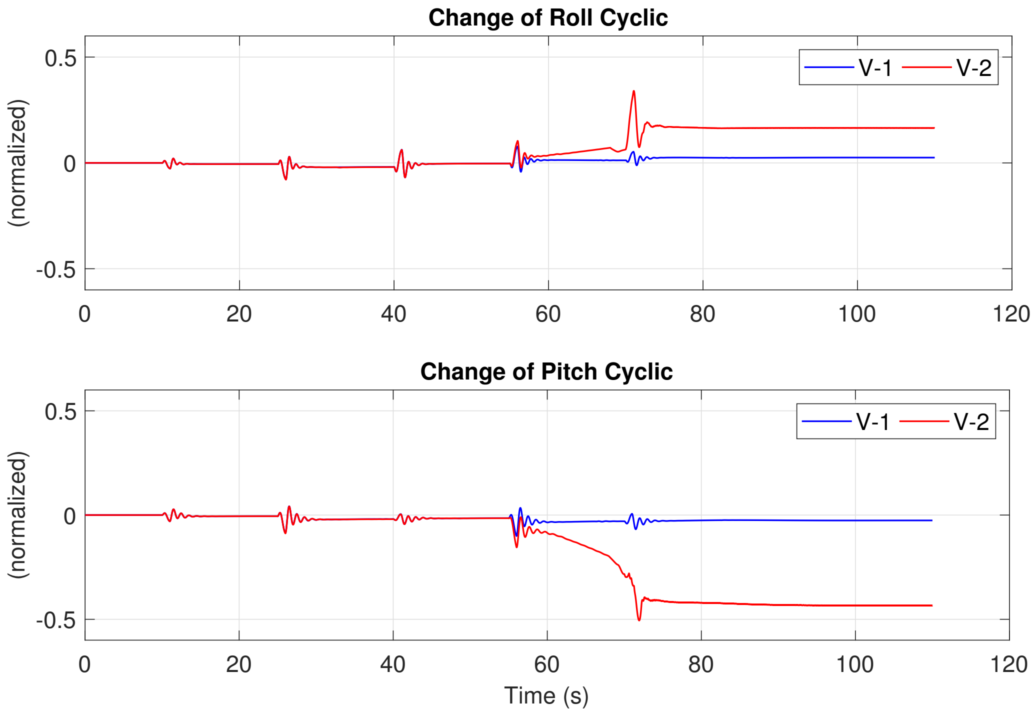

Figure 4.16: Roll and pitch cyclic positions of simulation

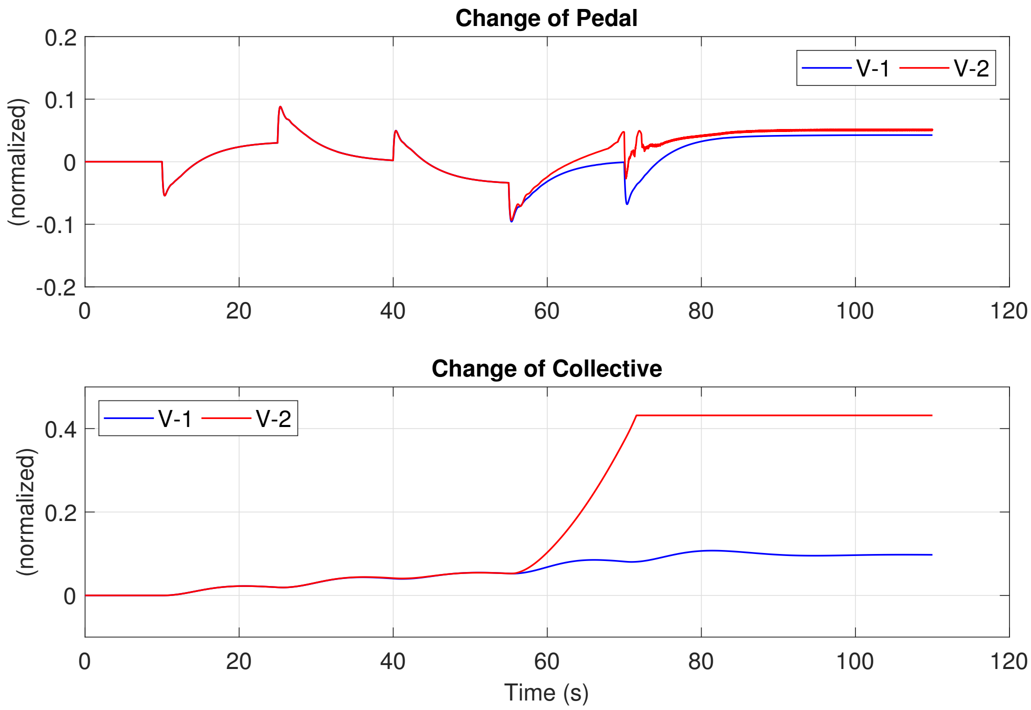

Figure 4.17: Pedal and collective positions of simulation

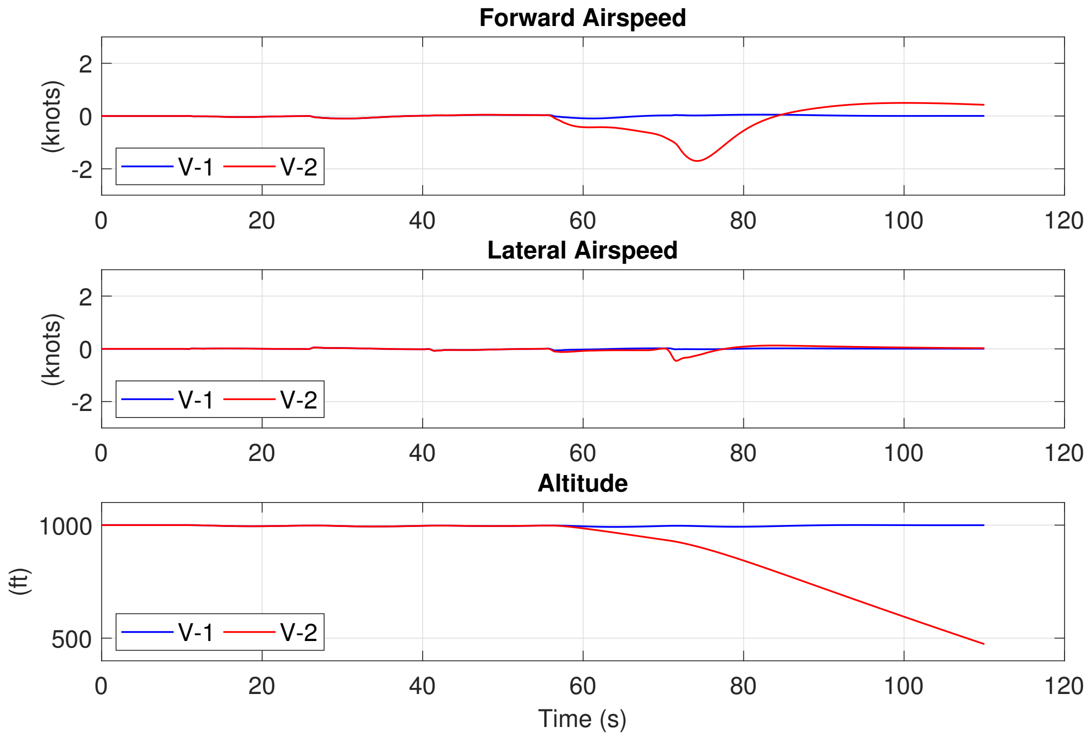

Figure 4.18: Airspeed and altitude of simulation

Losing altitude is inevitable with five rotor loss and 65% rotor speed limit in Vehicle-2. Although the aircraft cannot keep its initial altitude due to this reason (Fig. 4.18), the control system can provide sufficient controls to keep the attitude and airspeed in the trim condition. This result shows that the flight control system can provide sufficient control with the "on-line input re-distribution algorithm" following the rotor failures while simultaneously avoiding rotors from saturation.

4.4.1.2 Failure Case-2

In this simulation, rotors with the following numbers are failed, respectively: 1, 6, 2, 5, 3 (Fig. 4.19). These numbers are intentionally selected from the same region of the aircraft in order to push the control limits.

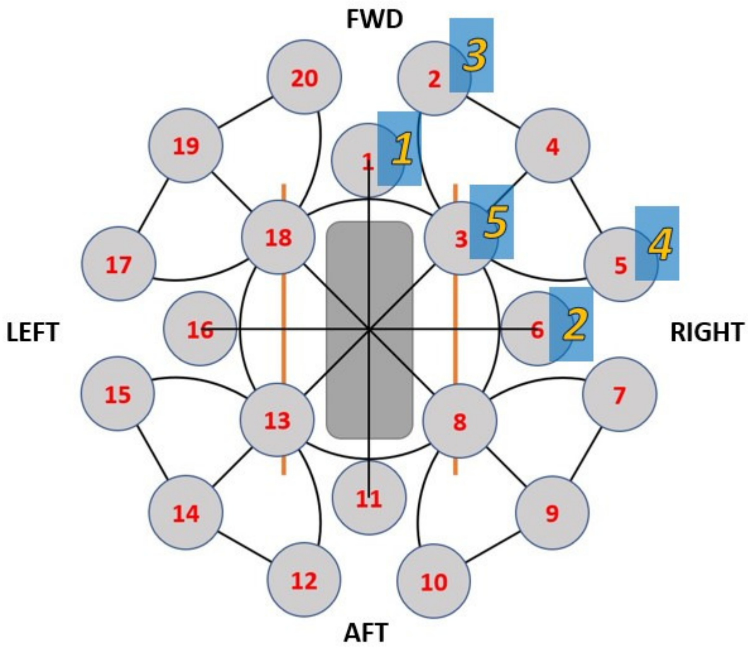

Figure 4.19: Failed rotors of case-2 and their orders

The results are shown in Figs. 4.20, 4.21, 4.22, 4.23 and 4.24.

By looking at the results, it can be clearly said that the proposed control method works successfully because Vehicle-1 can keep its hover trim condition steadily with very little control effort. All rotor speeds are automatically re-distributed on-line, following the rotor failures. As a result, there is almost no deviation in the controls from their trim values in order to stay at hover after each rotor failure.

However, in Vehicle-2, loads of the pilot work starts to increase with the failures (Figs. 4.22, 4.23). Finally, controls are hit the limits and the control force becomes insufficient. Then, the control of the aircraft is lost and it diverges from the hover condition towards the direction of the rotor failure region (Figs. 4.20, 4.21).

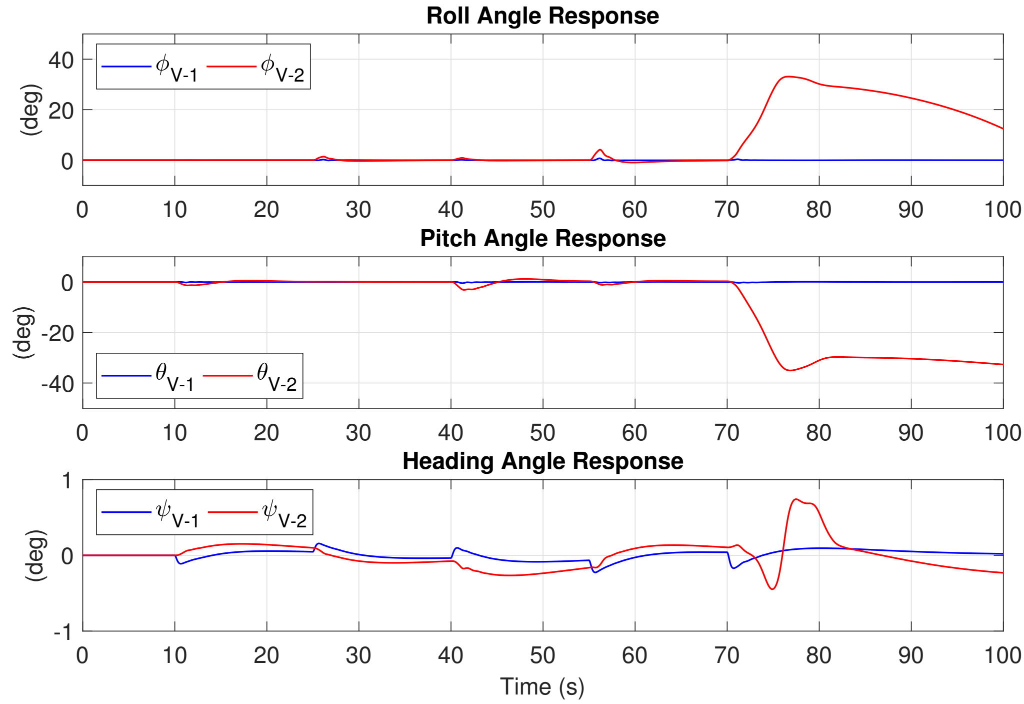

Figure 4.20: Euler angles of simulation

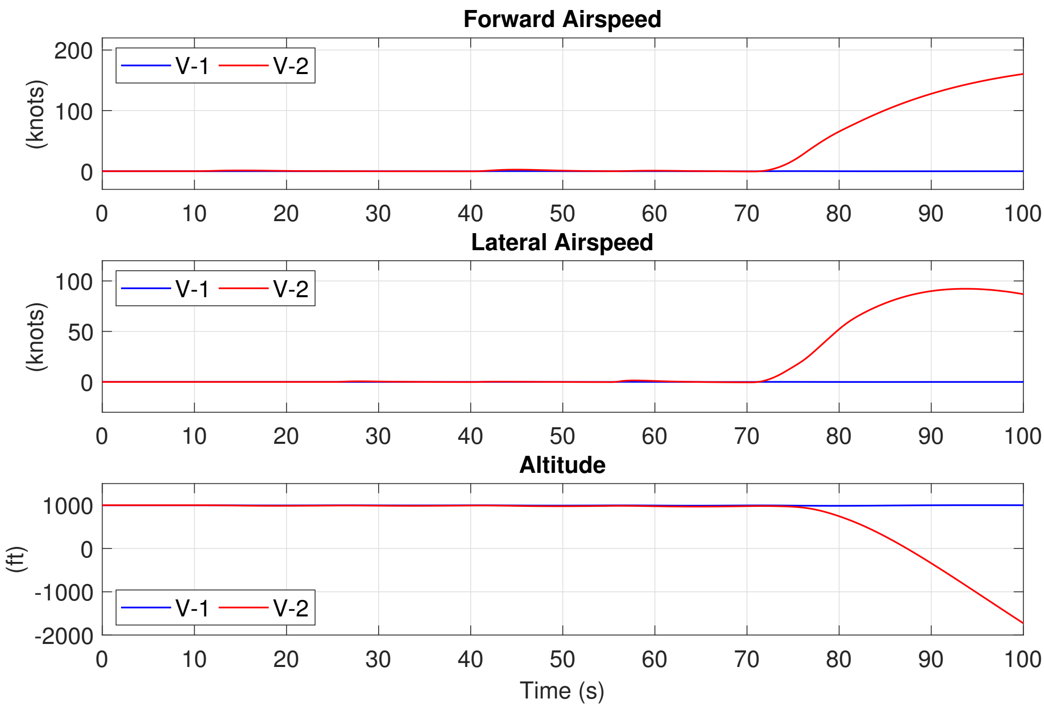

Figure 4.21: Airspeed and altitude of simulation

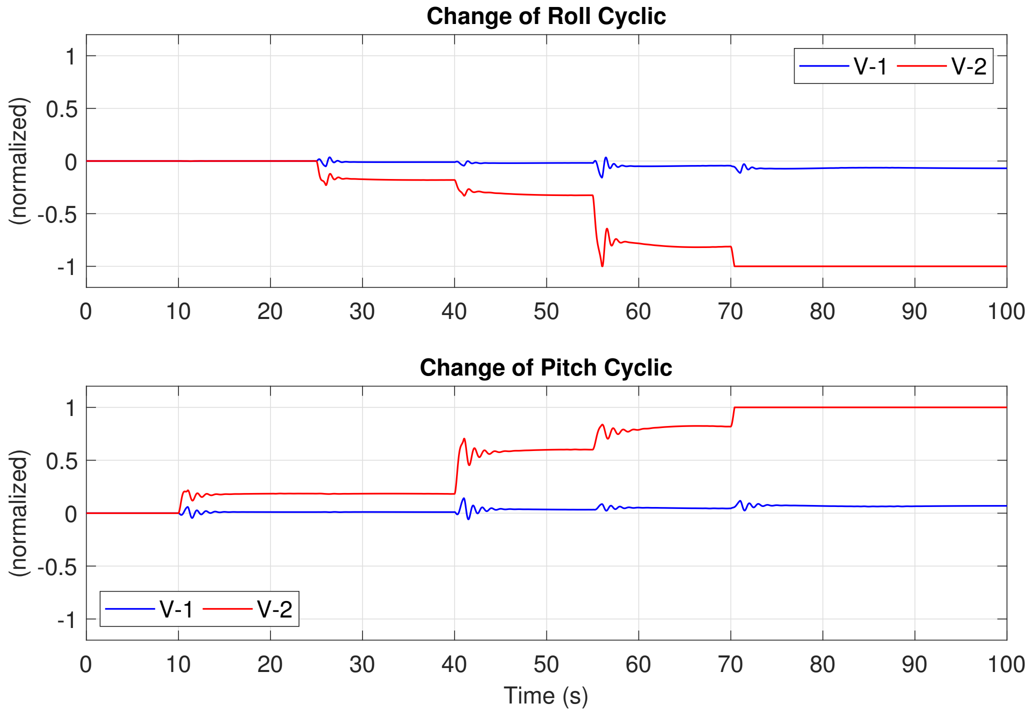

Figure 4.22: Roll and pitch cyclic positions of simulation

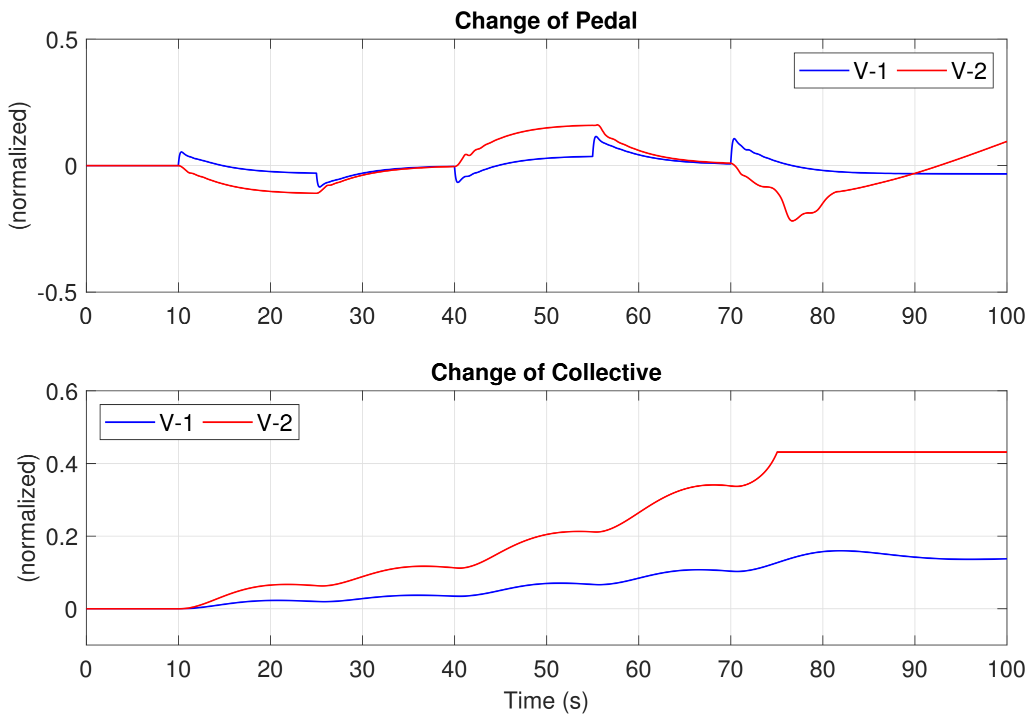

Figure 4.23: Pedal and collective positions of simulation

Since failed rotor positions are at the forward-right side, the aircraft has a tendency of pitch-down and roll-right. Thus, the manoeuvre controller model applies pitch-up and roll-left input. It also applies collective-up input to compensate loss of lift force. There is no such effort in the pedal because failed rotors rotates both directions in equal amounts so they cancel out their resultant yaw moments (Figs. 4.22, 4.23).

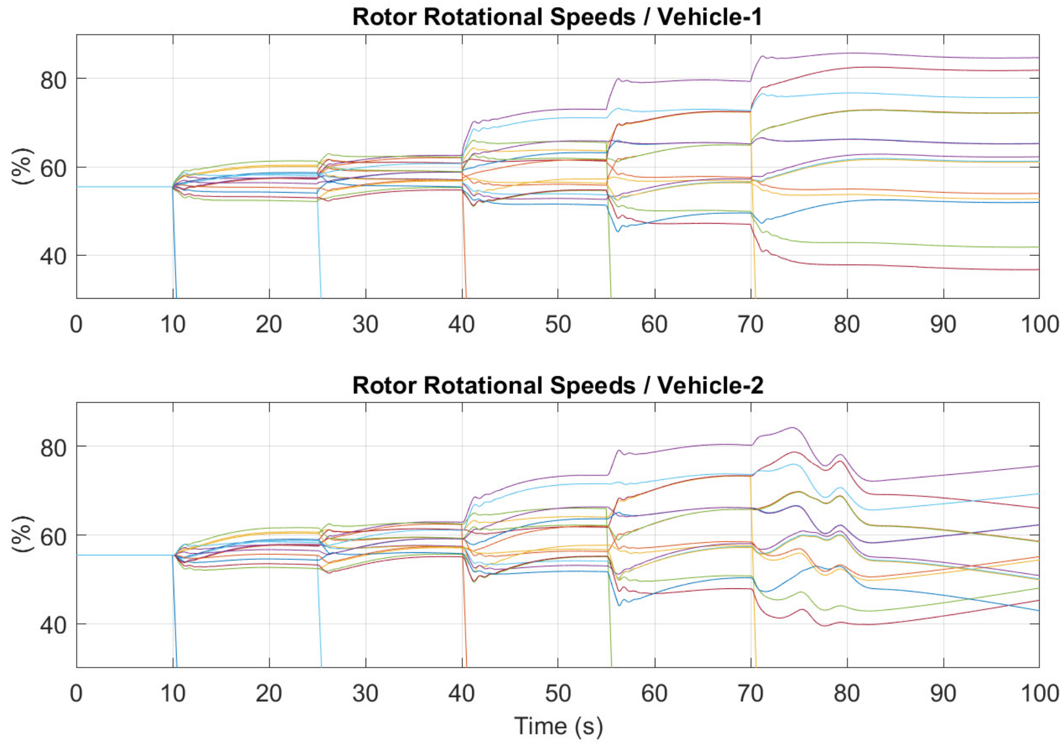

Figure 4.24: Rotor speed distribution of simulation

In Fig.4.24, failed rotor speeds become zero in one second. It is partly shown in the graph to provide closer visualization of the operating rotors.

4.4.1.3 Failure Case-3

In this simulation, rotors with the following numbers are failed, respectively: 19, 12, 11, 16, 6, 4, 1, 9, 18, 13 (Fig. 4.25). This means that half of the entire rotors are failed. These numbers are randomly selected.

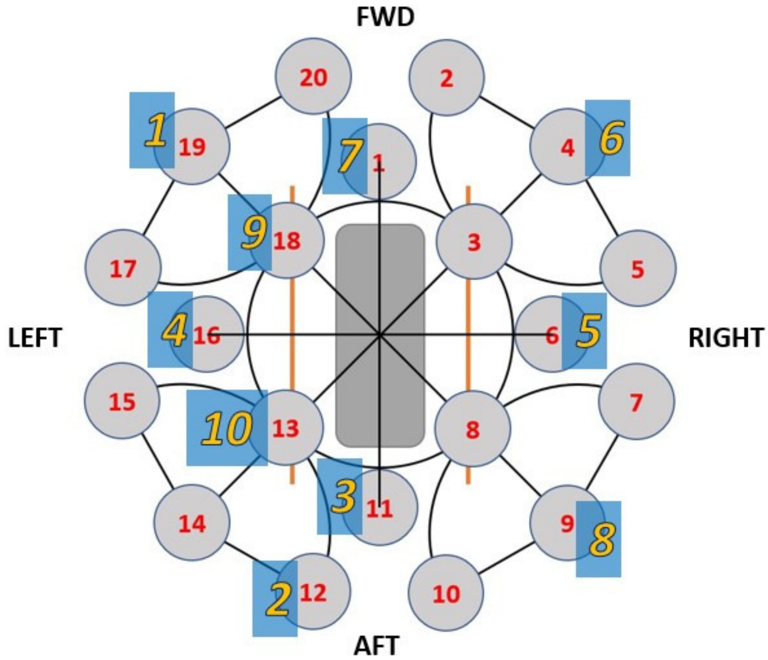

Figure 4.25: Failed rotors of case-3 and their orders

The results are shown in Figs. 4.26, 4.27, 4.28, 4.29 and 4.30.

In Vehicle-1, the aircraft survives from ten random rotor failures. Flight control system automatically re-distributes the rotor speeds after each failure, thus very little control change is observed in all channels in Figs. 4.28 and 4.29 as in the previous case (Section-4.4.1.2).

In Vehicle-2, the aircraft can keep euler attitudes in the trim condition (Fig. 4.26) since some of the failed rotors mutually compensate their dynamic effects emerged from failure. However, compensation of lift force is not sufficient because the collective control hits its maximum limit (Fig. 4.29) and the control is lost in the vertical channel (Fig. 4.27).

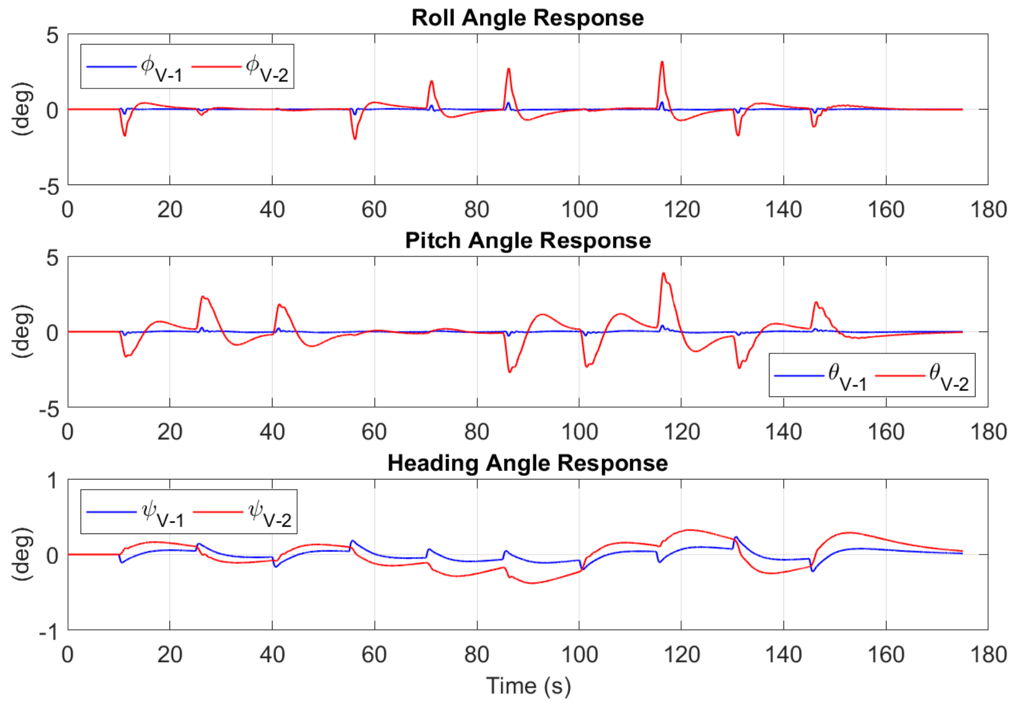

Figure 4.26: Euler angles of simulation

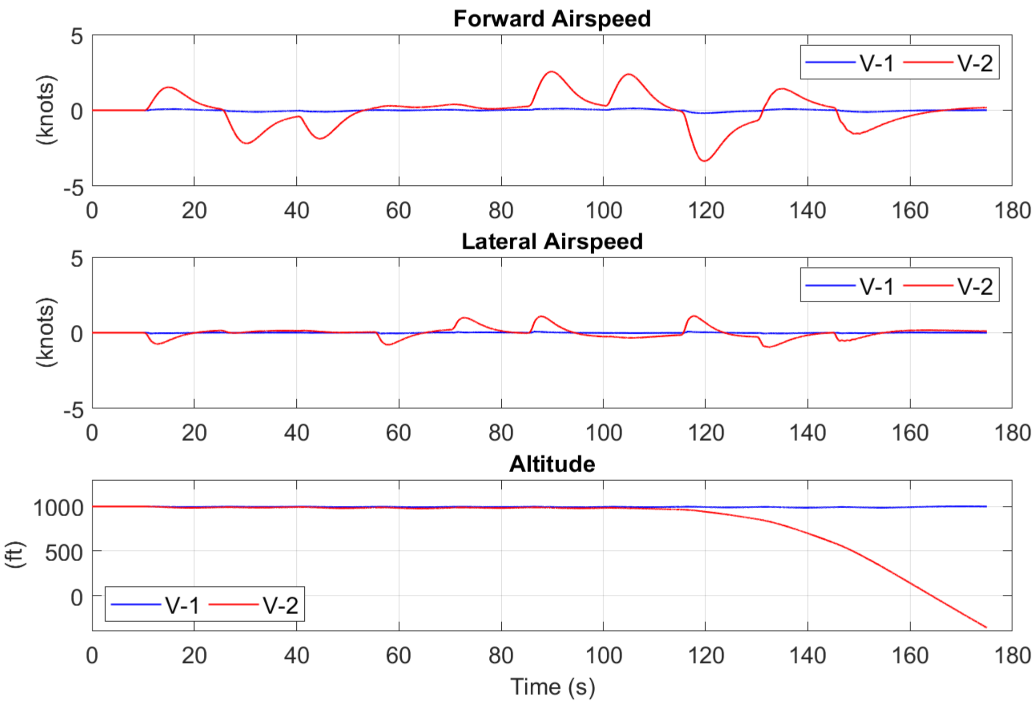

Figure 4.27: Airspeed and altitude of simulation

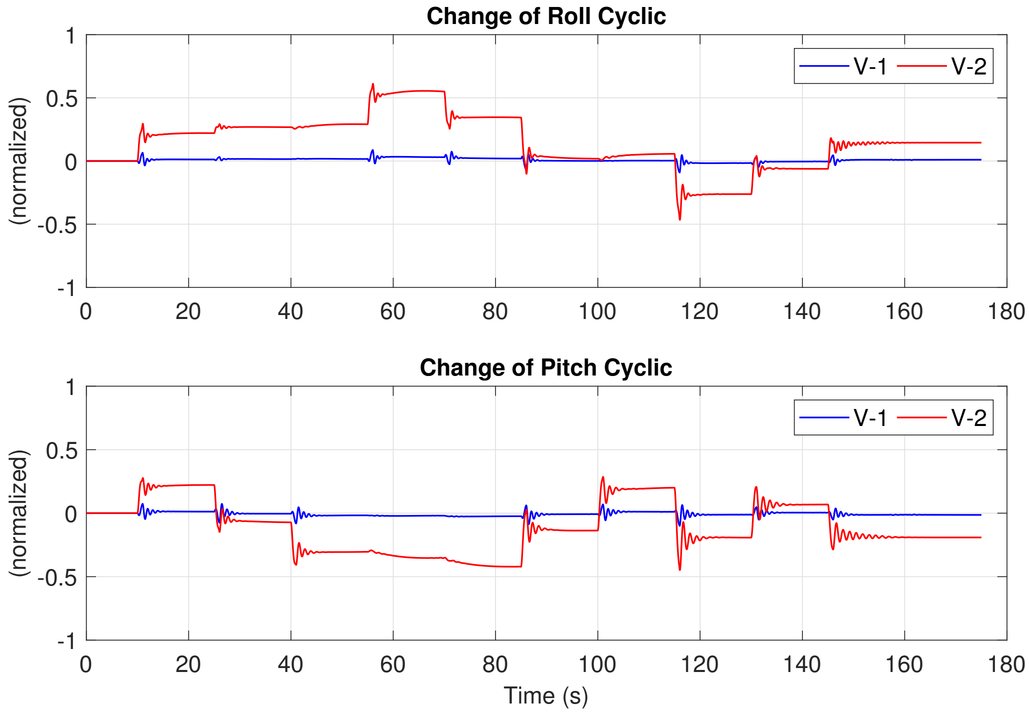

Figure 4.28: Roll and pitch cyclic positions of simulation

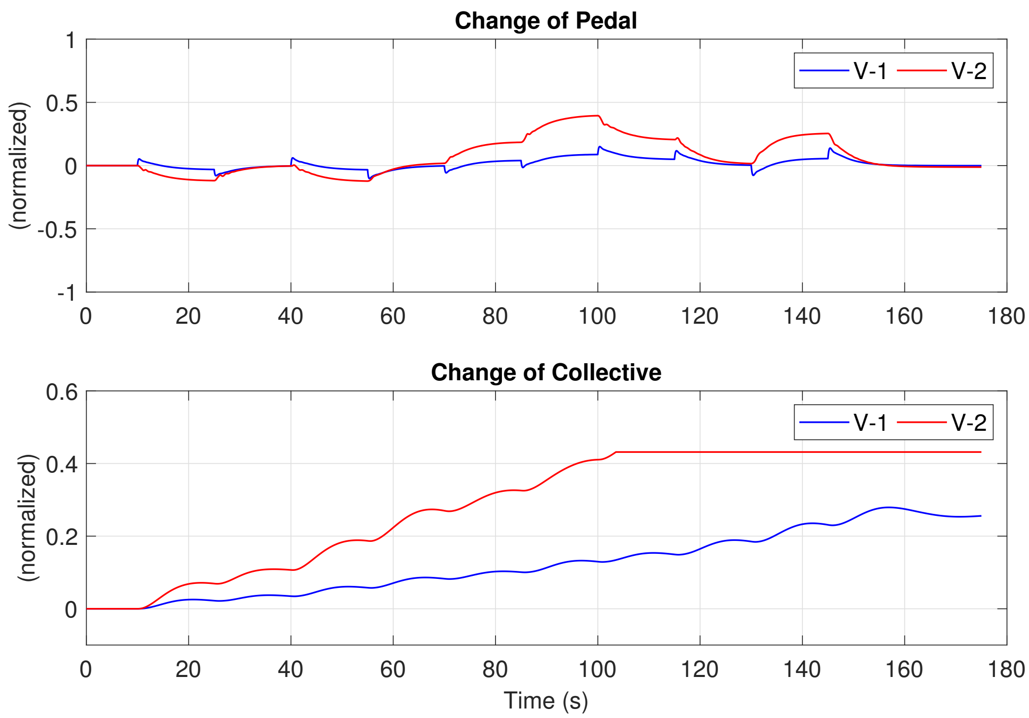

Figure 4.29: Pedal and collective positions of simulation

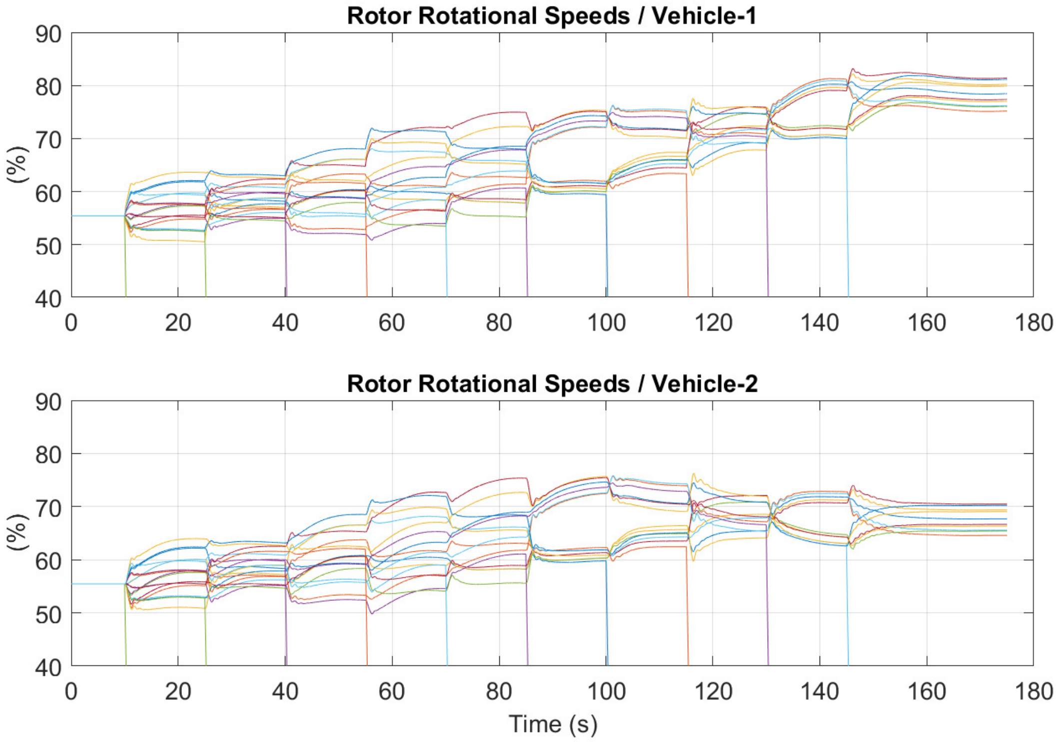

Figure 4.30: Rotor speed distribution of simulation

In Fig.4.30, failed rotor speeds become zero in one second. It is partly shown in the graph to provide closer visualization of the operating rotors.

4.4.2 Forward Flight

For the simulations conducted in this section, forward flight trim condition is shown in Tables 4.17 and 4.18. Values of the trim states can be read from the Table 4.17 and the corresponding rotor rotational speed distribution can be found in the Table 4.18.

Parameter	Unit	Value
Altitude	ft	1000.00
ΔISA	-	0.00
Longitudinal velocity in body frame (U)	ft/s	101.27
Lateral velocity in body frame (V)	ft/s	0.00
Normal velocity in body frame (W)	ft/s	-6.32
Vertical Speed	ft/min	0.00
Roll angle (ϕ)	deg	0.00
Pitch angle (θ)	deg	-3.57
Roll cyclic input	norm	0.00
Pitch cyclic input	norm	-0.01
Pedal input	norm	0.00
Collective input	norm	0.35

Table 4.17: Forward flight trim results

Rotor Number	Rotor Speed (%)	Rotor Number	Rotor Speed (%)
No: 1	44.0	No: 11	44.2
No: 2	44.0	No: 12	44.3
No: 3	44.1	No: 13	44.2
No: 4	44.0	No: 14	44.2
No: 5	44.1	No: 15	44.2
No: 6	44.1	No: 16	44.1
No: 7	44.2	No: 17	44.1
No: 8	44.2	No: 18	44.1
No: 9	44.2	No: 19	44.0
No: 10	44.3	No: 20	44.0

Table 4.18: Rotor speed distribution of forward flight trim

Failure scenarios and the simulation procedures are the same as in Section-4.4.1. The only difference here, is the trim condition which is 60 knots forward flight instead of hovering.

4.4.2.1 Failure Case-1

In Vehicle-2, rotor rotational speed limit is defined as 2565 RPM (57%) for this section.

Simulation results are shown in Figs. 4.31, 4.32, 4.33, 4.34 and 4.35.

Results of the two vehicles are closer to each other than simulations of Section-4.4.1.1, because rotors produce more thrust in forward flight due to higher free-stream velocity. Then, amount of the applied controls become less for manoeuvring. As a result, rotor speed deviations are lower and only three rotors are saturated during the simulation (Fig. 4.35).

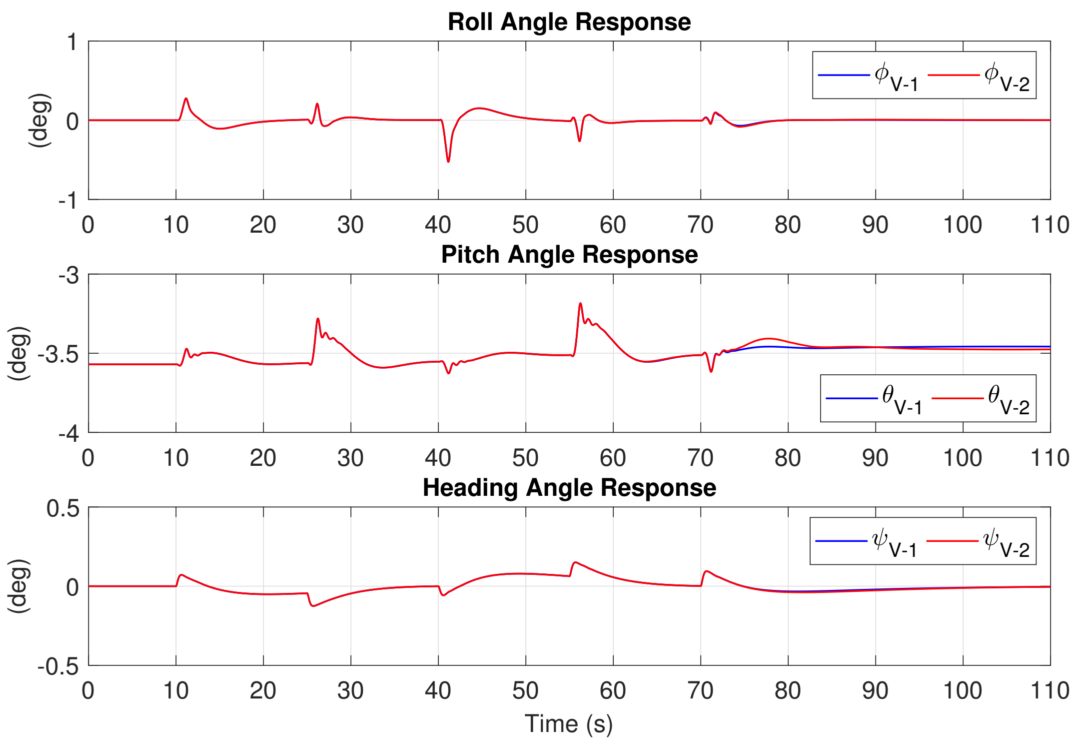

Figure 4.31: Euler angles of simulation

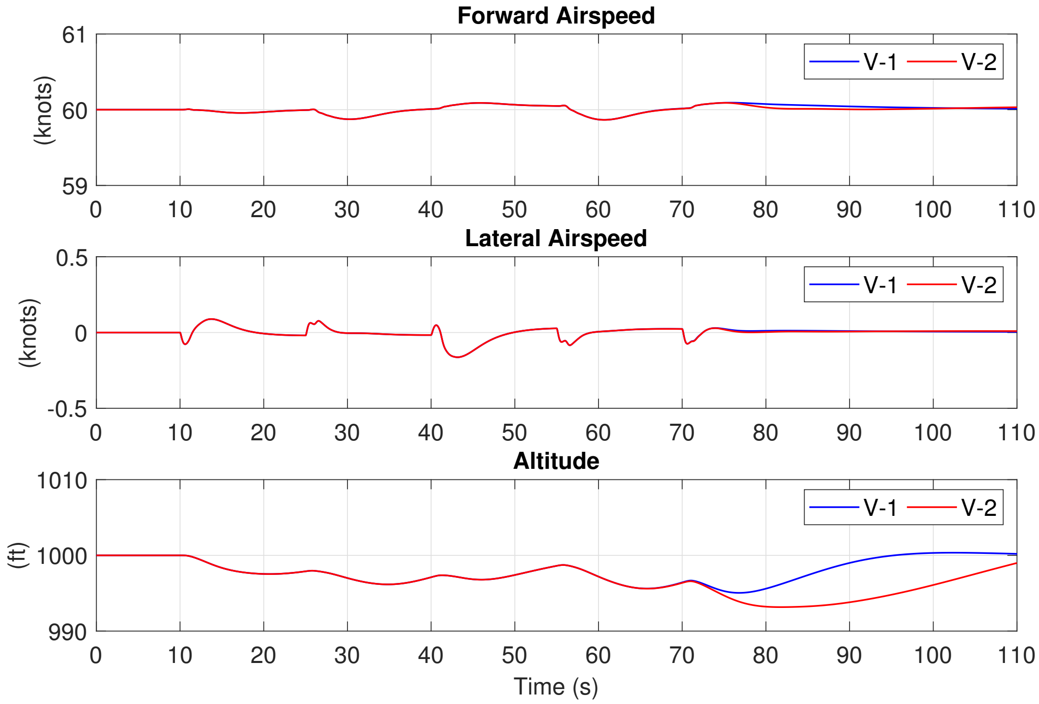

Figure 4.32: Airspeed and altitude of simulation

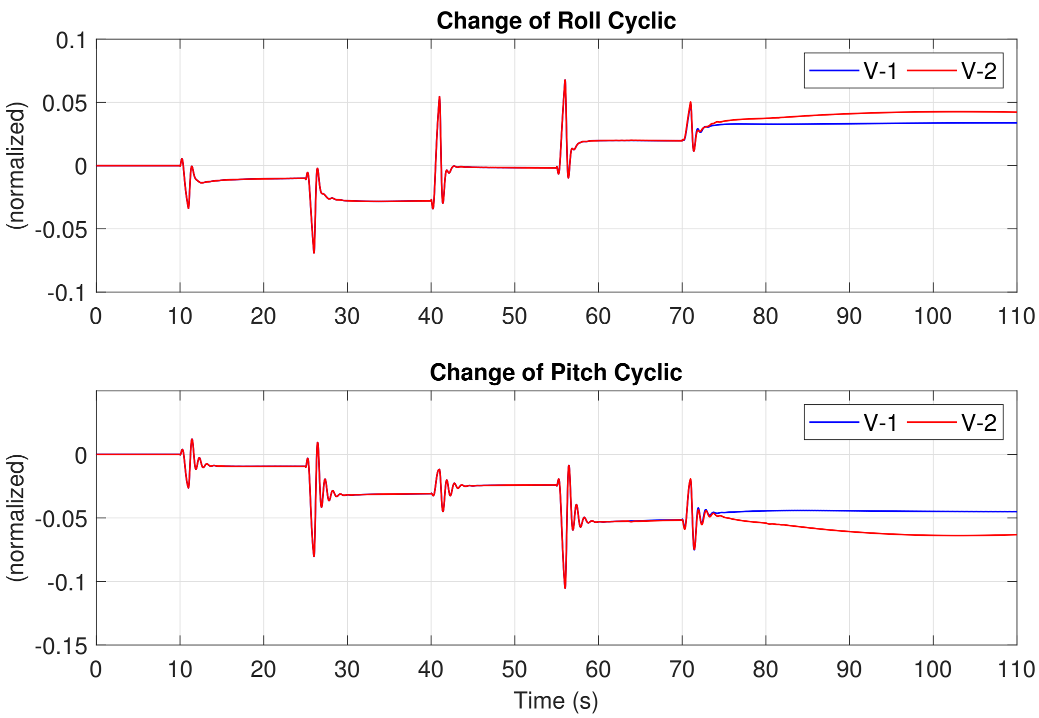

Figure 4.33: Roll and pitch cyclic positions of simulation

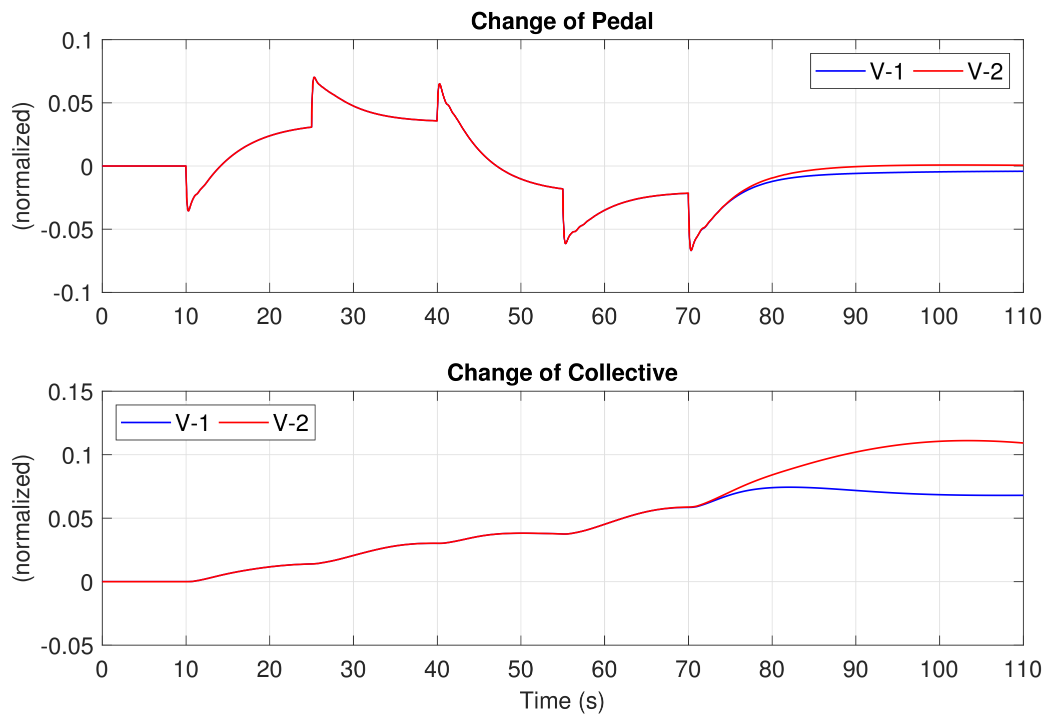

Figure 4.34: Pedal and collective positions of simulation

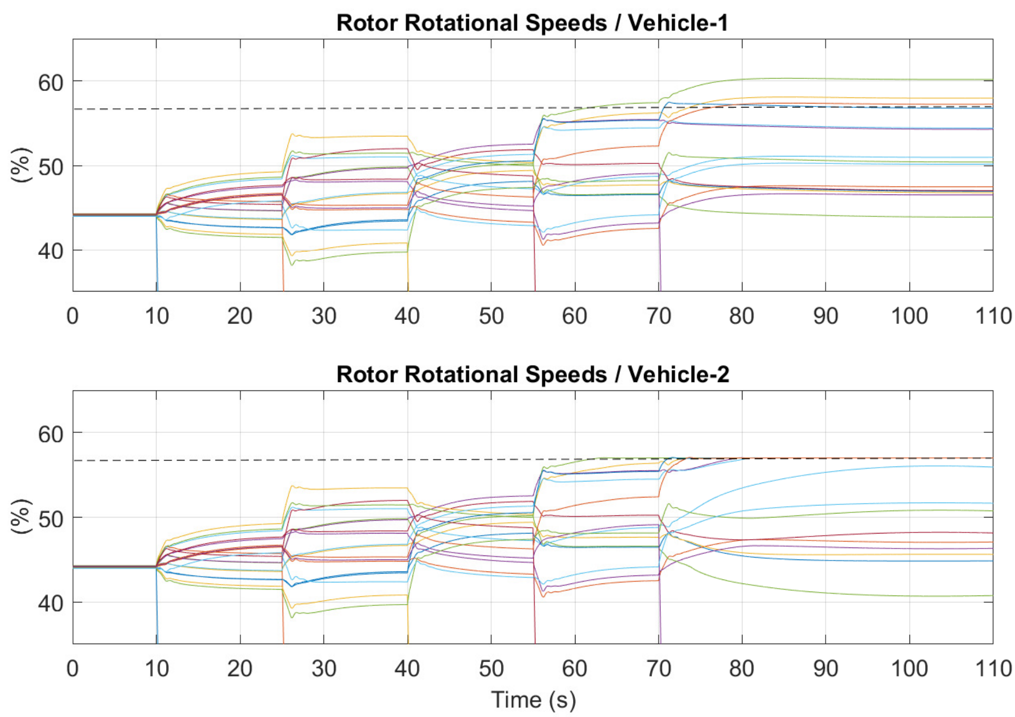

Figure 4.35: Rotor speed distribution of simulation

In Fig.4.35, failed rotor speeds become zero in one second. It is partly shown in the graph to provide closer visualization of the operating rotors.

This simulation shows that the rotor saturations are prevented by the flight control system also in forward flight condition.

4.4.2.2 Failure Case-2

Simulation results are shown in Figs. 4.36, 4.37, 4.38, 4.39 and 4.40.

The difference from the results of hover in Section-4.4.1.2 is that Vehicle-2 can keep its initial trim condition in this section (Figs. 4.36, 4.37). In the hover case, the controls were saturated and the aircraft diverged from its trim condition (Section-4.4.1.2).

In the forward flight case considered in this section, such a result is obtained because higher control force can be produced in the forward flight. Free-stream velocity is higher, thus rotors can generate more thrust. Consequently, the control intervals are adequate to keep the aircraft in control although positions of the controls get almost the edge of their limits near the end of simulation (Figs. 4.38, 4.39).

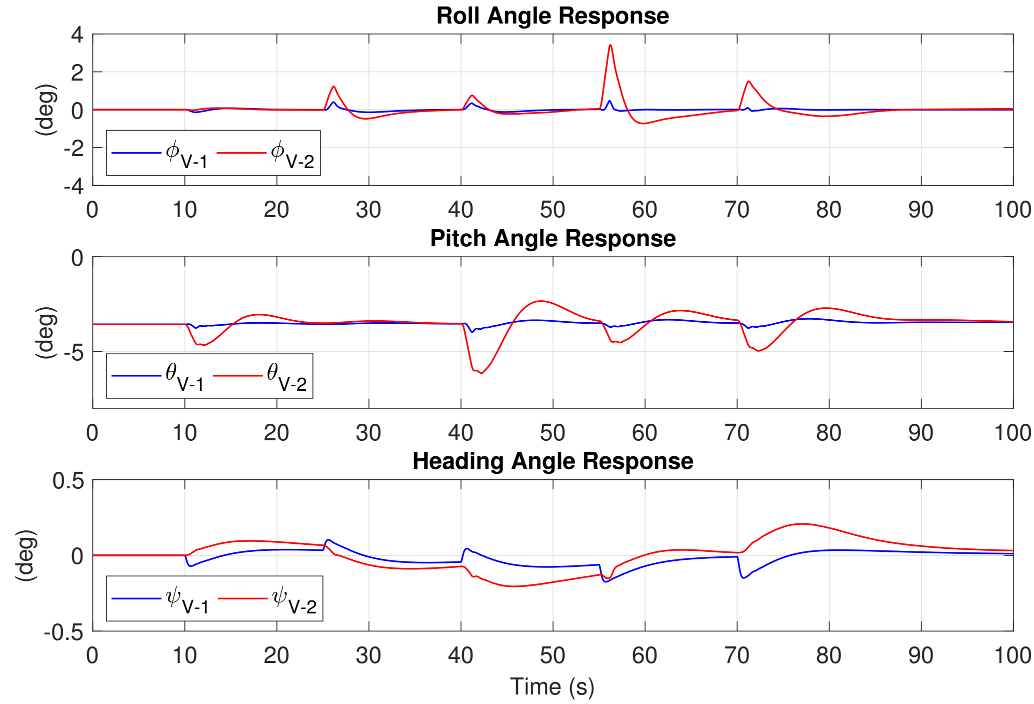

Figure 4.36: Euler angles of simulation

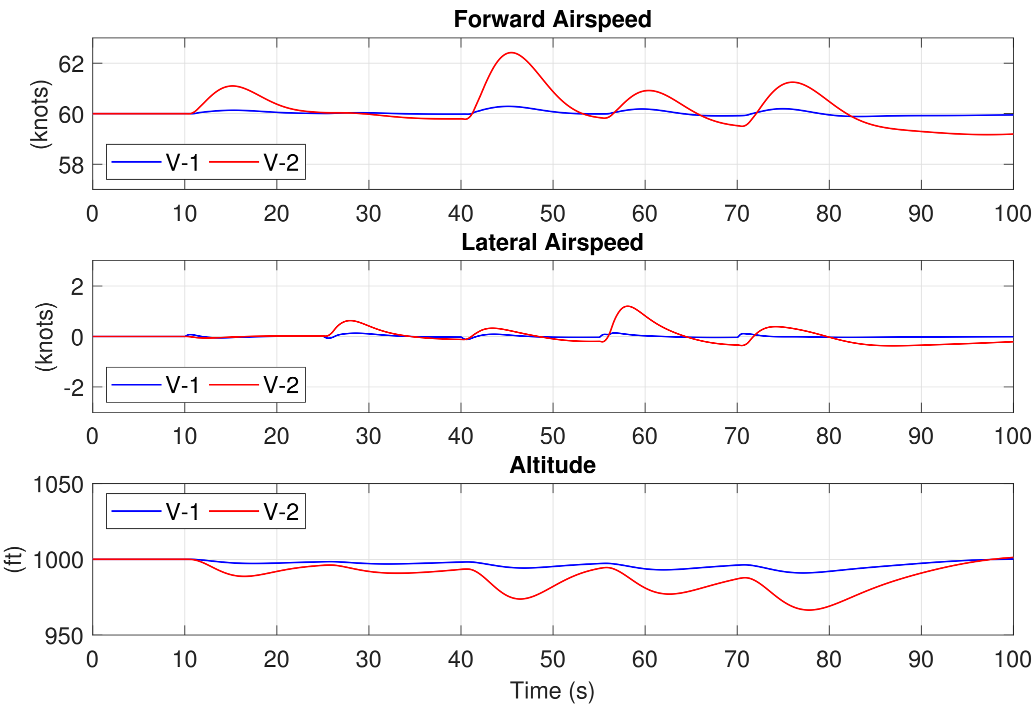

Figure 4.37: Airspeed and altitude of simulation

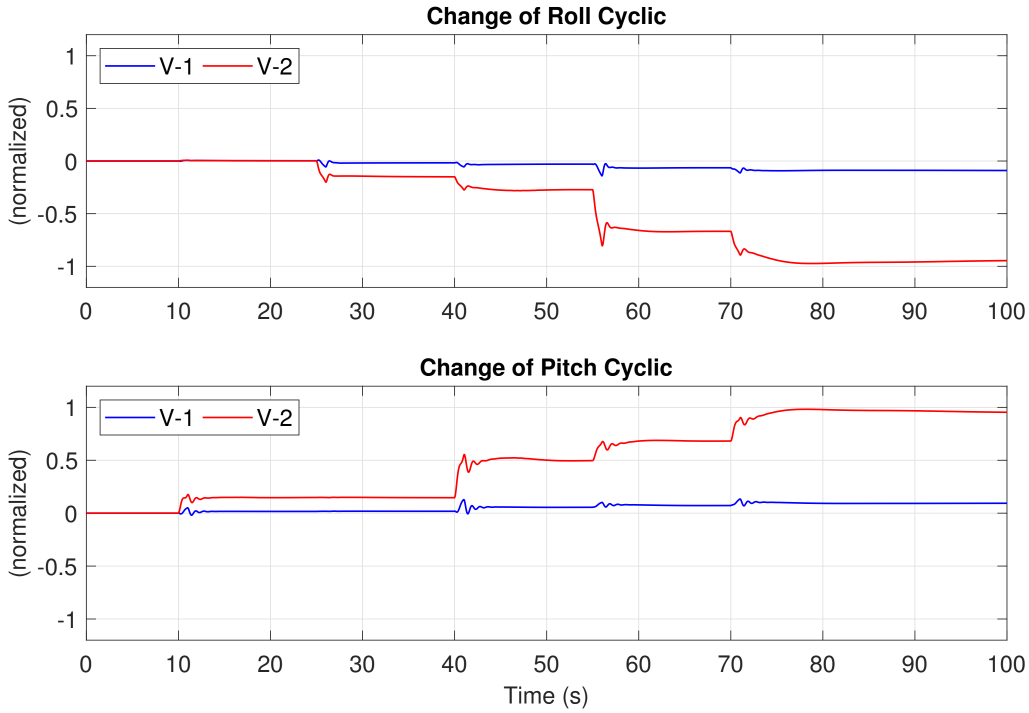

Figure 4.38: Roll and pitch cyclic positions of simulation

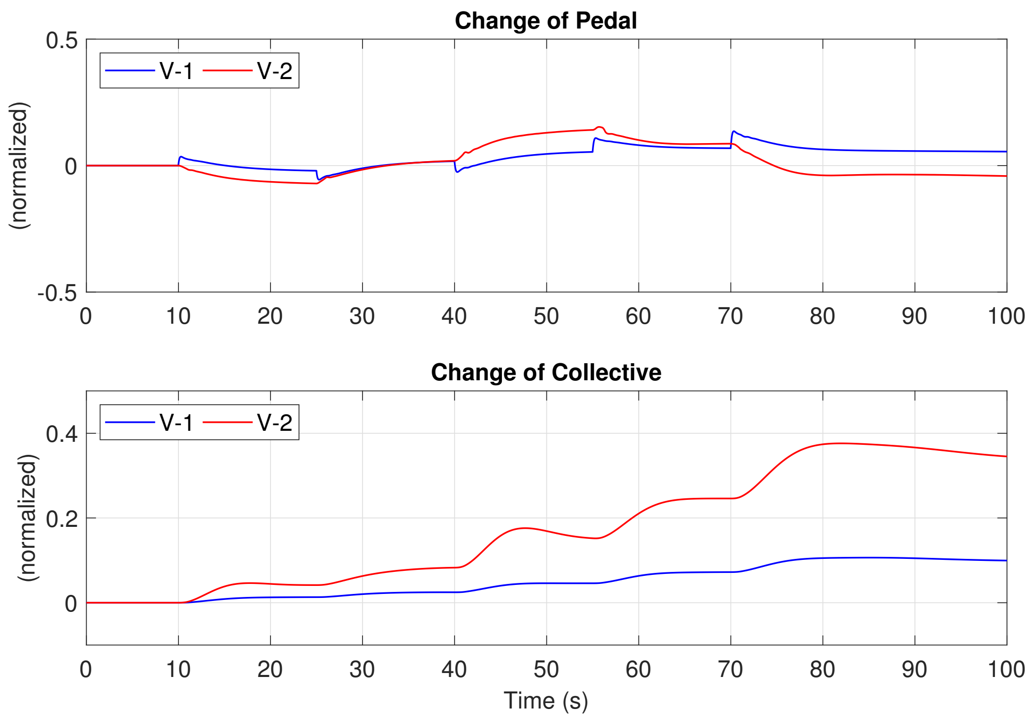

Figure 4.39: Pedal and collective positions of simulation

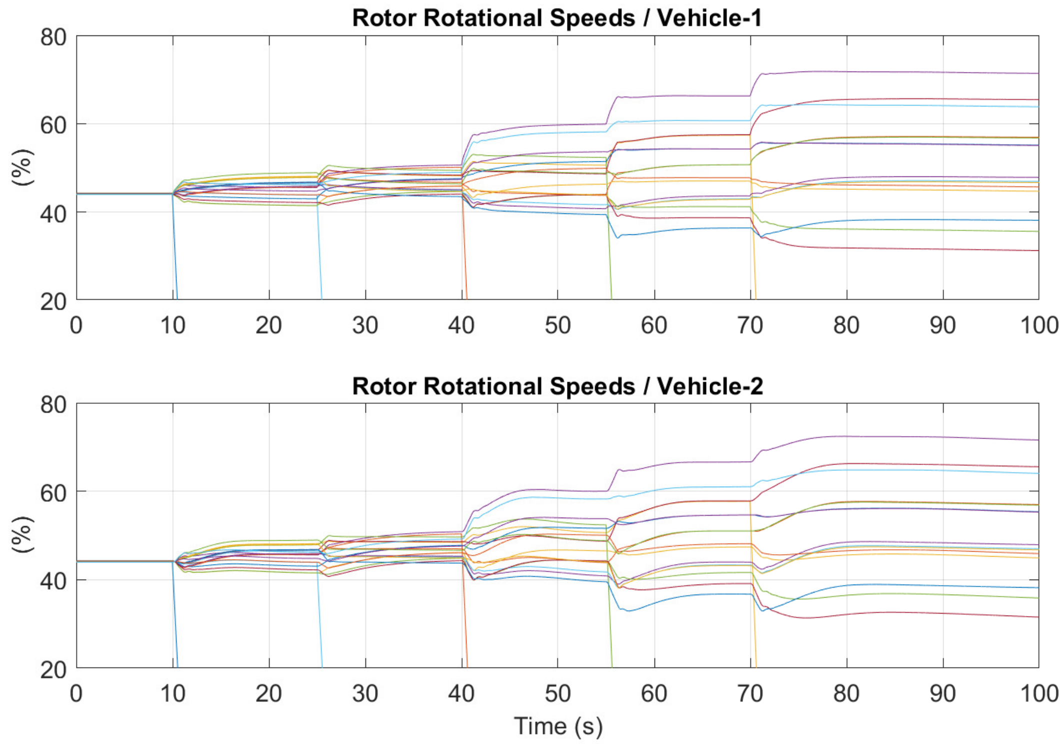

Figure 4.40: Rotor speed distribution of simulation

In Fig.4.40, failed rotor speeds become zero in one second. It is partly shown in the graph to provide closer visualization of the operating rotors.

By looking at the results of this section, the proposed control method works properly also in the forward flight condition. Although Vehicle-2 can survive from failures, its control effort is very high compared to Vehicle-1. Inputs are re-distributed in Vehicle-1. Therefore, it can survive until the end of simulation with a very little pilot control effort. This significant difference can be seen in Figs.4.38 and 4.39.

4.4.2.3 Failure Case-3

Simulation results are shown in Figs. 4.41, 4.42, 4.43, 4.44 and 4.45.

The difference from the results of hover case in Section-4.4.1.3 is that Vehicle-2 can keep its initial trim condition throughout the simulation, in this section. In the hover case, Vehicle-2 cannot keep flying at its initial altitude until the end of simulation and starts diving (Section-4.4.1.3). The explanation of this is about the same phenomena explained in Section-4.4.2.2 which is related with the existence of higher rotor thrust generation at higher amount of free-stream velocity. The similar results can be seen in the figures below, as of Section-4.4.2.2.

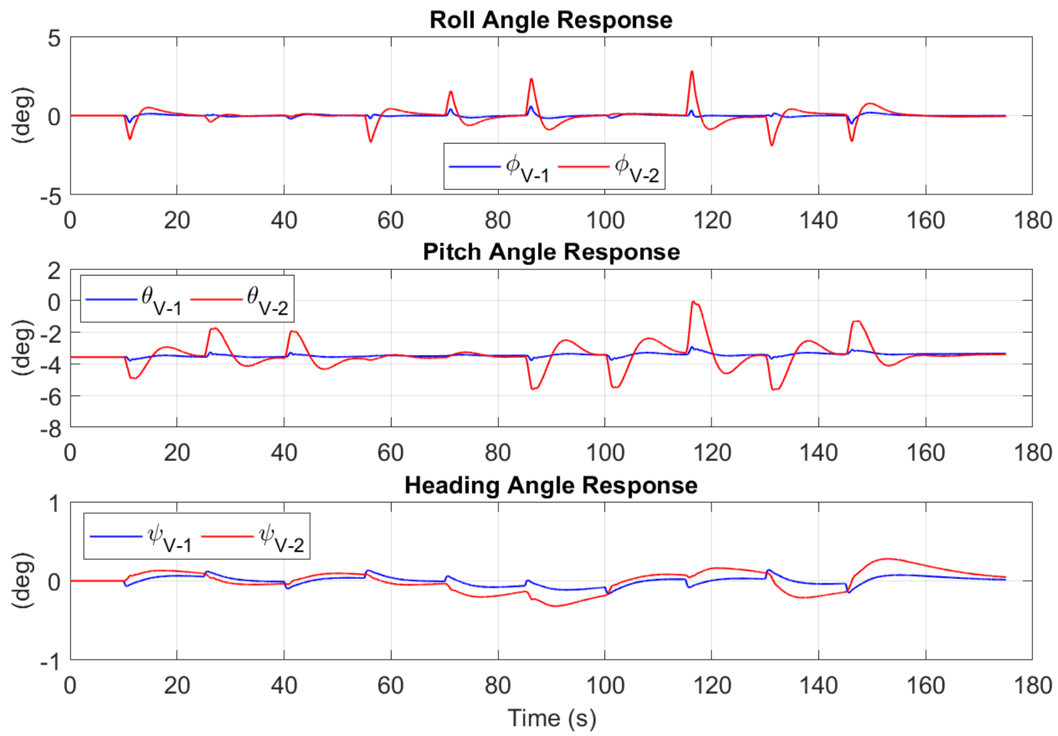

Figure 4.41: Euler angles of simulation

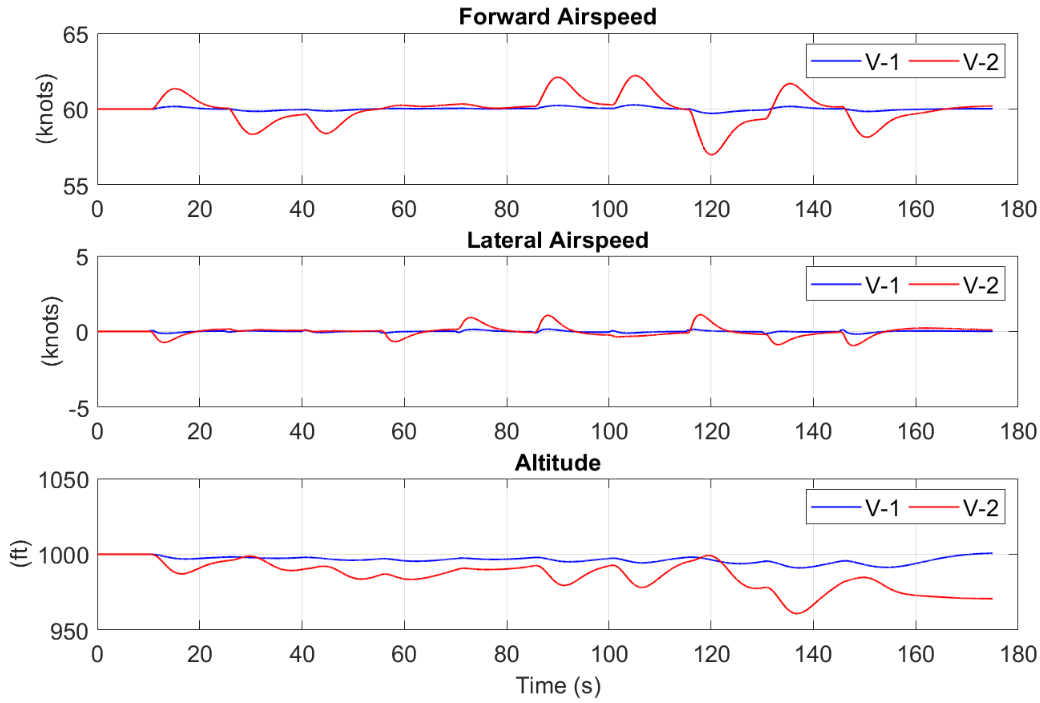

Figure 4.42: Airspeed and altitude of simulation

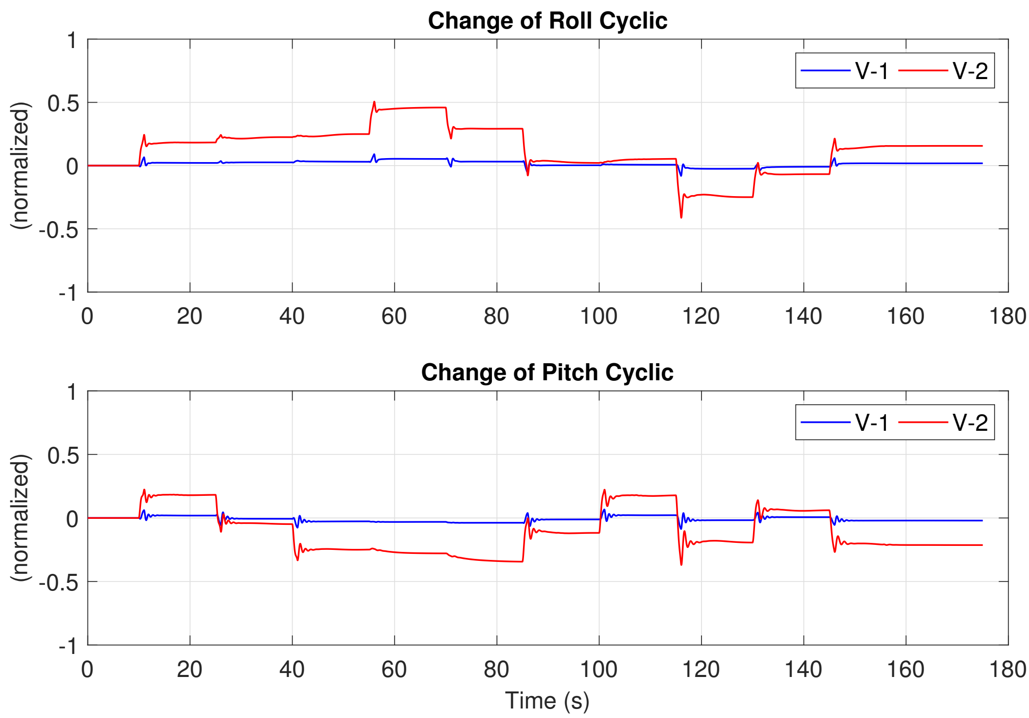

Figure 4.43: Roll and pitch cyclic positions of simulation

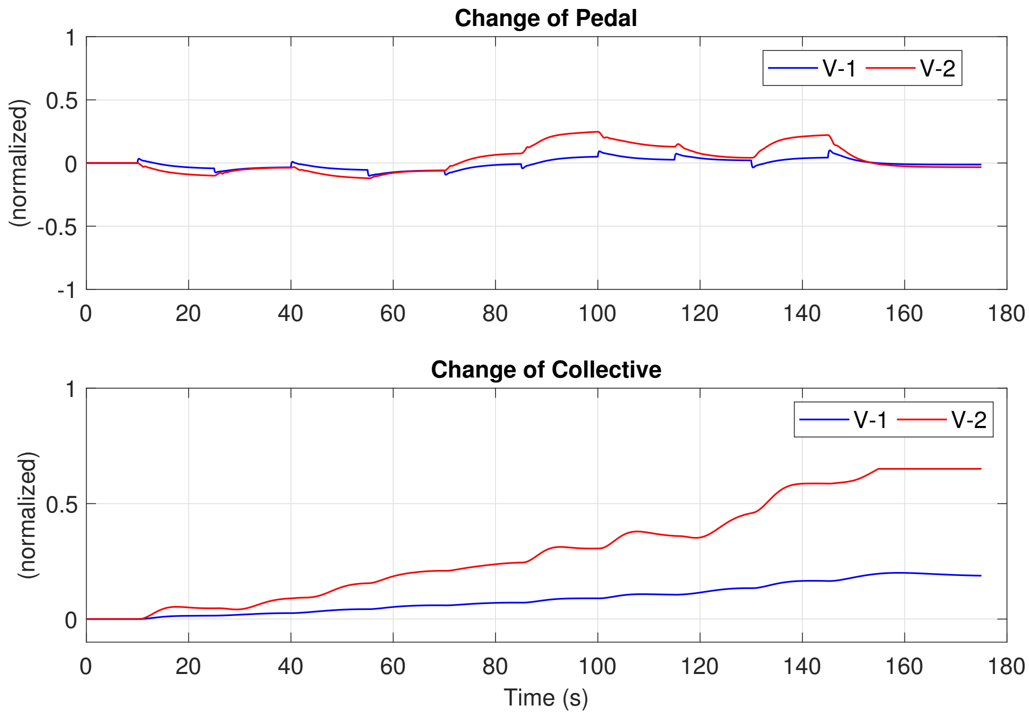

Figure 4.44: Pedal and collective positions of simulation

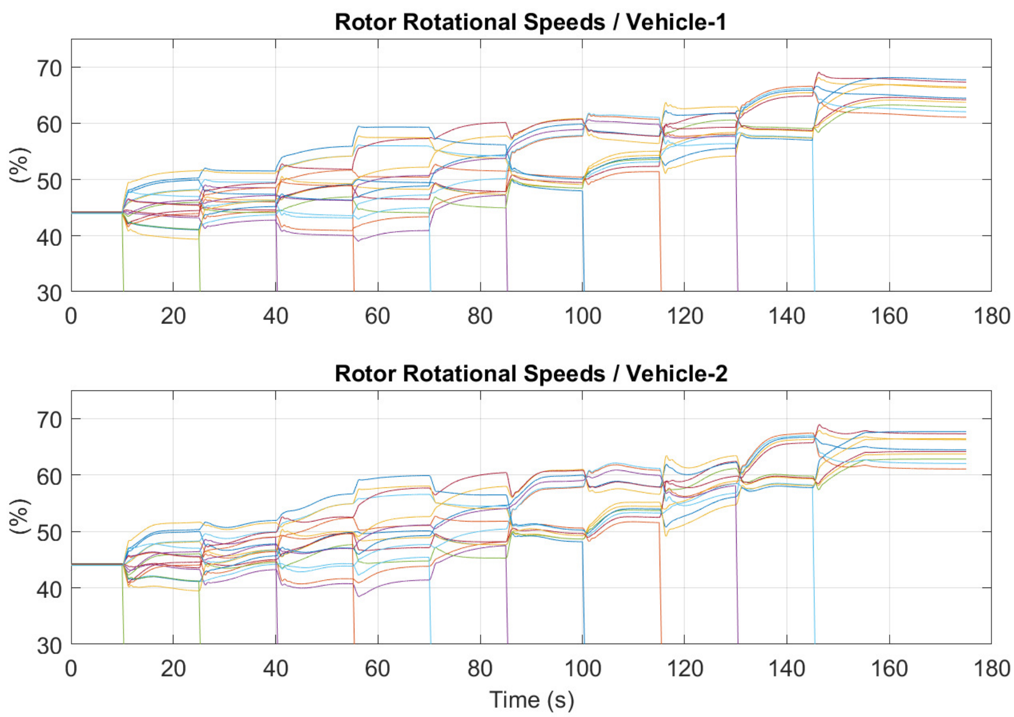

Figure 4.45: Rotor speed distribution of simulation

In Fig.4.45, failed rotor speeds become zero in one second. It is partly shown in the graph to provide closer visualization of the operating rotors.

To conclude, this simulation shows that safe flight achieved in the hover case of Section-4.4.1.3 by the proposed control method can also be achieved in the forward flight condition.

CHAPTER 5

CONCLUSIONS

In this thesis, a flight control system is designed for a conceptual multi-rotor eVTOL aircraft. Nonlinear simulation model of the aircraft is developed. It includes rotor models with nonlinear aerodynamic coefficients and inflow dynamics, electric motor models as actuators with physical limits and a fuselage model. Also, a simulation environment is created by using six degrees-of-freedom equations of motion, atmosphere model and an autopilot model. The controller model is used to find trim conditions of the aircraft and to conduct simulation tests.

In the control system, dynamic control allocation with Blended-Inverse is used. Using this method, singularities are prevented during control matrix inversion and input distribution along rotors are obtained to perform the demanded manoeuvre. To prevent actuator (rotor speed) saturation during manoeuvres, an offset vector is introduced for inputs and the effect of the saturated rotor is limited in the control allocation. This avoids further increasing the speed of saturated rotor and provides input re-distribution satisfying the demanded manoeuvre by using the remaining unsaturated rotors. Also, rotor saturation avoidance is addressed by modifying elements of the input weight matrix. It is seen that sufficient avoidance from saturation limits can also be achieved with this method.

During failure, dimension reduction technique is applied dynamically to the control allocation where aerodynamic effect of the failed rotor is removed. This yields that required thrust and moments are shared between operating rotors only. This method provides on-line input re-distribution to maintain current manoeuvre in case of rotor failure.

The proposed method is implemented to the developed multi-rotor eVTOL aircraft and simulation based flight tests are conducted. These tests consist of three parts. First part includes steady-state performance tests for the proof of concept. The analysis show that the effective re-distribution is possible in various combinations of operating rotors. Trim values of control positions of failed rotor conditions are very close to that of no failure condition. Second part includes transient tests between hover and forward flight where two different vehicles are compared. These tests demonstrate that the proposed control system can provide sufficient control as rotors saturate. In the third part, various rotor failure scenarios are committed to test flight safety of the dynamic system. It is seen that the aircraft with the proposed control system implemented can survive from all failure scenarios successfully by fast and effective on-line input re-distribution following the failures.

The following are obtained for both hover and forward flight conditions with the proposed study of this thesis:

- Control distribution at nominal flight conditions
- On-line control re-distribution as actuators saturate
- On-line control re-distribution as actuators fail
- Control sensitivity adjustment using weight matrices

As future work, the proposed method can be applied to a more enhanced aircraft model. Better airfoil data can be used for rotor blades with aerodynamic coefficients. Aerodynamic interactions between rotor to rotor and rotor to fuselage can be included. Also, more detailed inflow models can be implemented to each rotor. As final notes, an identification system for rotor failure detection can be implemented to the aircraft.

In conclusion, dynamic control allocation with Blended-Inverse is demonstrated on a multi-rotor eVTOL aircraft application in the simulation environment. Rotor failure scenarios and actuator saturation limits are considered in simulation tests for demonstration. The conceptual aircraft and the simulation environment is modelled in detail to provide realistic and accurate simulation results. It is shown that an over-actuated multi-rotor eVTOL aircraft can be flown effectively with the proposed flight control system design. Also, it is proved to be sufficient, robust and redundant in case of actuator saturation and failure.

REFERENCES

[1] Volocopter design. `https://www.volocopter.com/en/product/`. Accessed: 2021-01-27.

[2] R. N. Ariel Walter, Michael McKay and F. Gandhi. Trim analysis of a classical octocopter after single-rotor failure. *AIAA Propulsion and Energy Forum*, Cincinnati, Ohio, July 2018.

[3] J. F. W. Aryeh Marks and I. Yamamoto. Control allocation for fault tolerant control of a vtol octorotor. *UKACC International Conference on Control*, Cardiff, UK, September 2012.

[4] K. A. Bordignon. *Constrained Control Allocation for Systems with Redundant Control Effectors*. PhD thesis, Virginia Polytechnic Institute and State University, 1996.

[5] K. A. Bordignon and W. C. Durham. Closed-form solutions to constrained control allocation problem. *Journal of Guidance, Control, and Dynamics*, Vol:18, No:5, September-October 1995.

[6] O. Cornes. Basic design limitations for urban electric vtol aircraft. *Vertical Flight Society 75th Annual Forum and Technology Display*, Philadelphia, Pennsylvania, May 2019.

[7] M. E. Dreier. *Introduction to Helicopter and Tiltrotor Simulation*. American Institute of Aeronautics and Astronautics Inc., 1801 Alexander Bell Drive, Reston, VA 20191, 2007.

[8] W. C. Durham. Constrained control allocation. *Journal of Guidance, Control, and Dynamics*, Vol:16, No:4, July-August 1993.

[9] O. Harkegard. Dynamic control allocation using constrained quadratic programming. *Journal of Guidance, Control, and Dynamics*, Vol:27, No:6, November-December 2004.

[10] D. B. D. Michael W. Oppenheimer and M. A. Bolender. Control allocation for over-actuated systems. *14th Mediterranean Conference on Control and Automation*, 2006.

[11] L. Z. Michele Furci, Carlo Nainer and A. Franchi. Input allocation for the propeller-based overactuated platform rospo. *IEEE Transactions on Control Systems Technology*, 2020.

[12] I. Y. Ozan Tekinalp and T. Unlu. Simulation and flight control of a tilt duct uav. *AIAA Modeling and Simulation Technologies Conference*, Chicago, Illinois, August 2009.

[13] E. D. F. Snell S. A. and G. W. L. Nonlinear inversion flight control for a supermaneuverable aircraft. *AIAA Guidance, Navigation, and Control Conference*, pp:808–817, Washington, DC, 1990.

[14] O. Tekinalp and E. Yavuzoglu. A new steering law for redundant control moment gyroscope clusters. *Aerospace Science and Technology*, 9 (2005) 626634.

[15] E. A. M.-C. Victor Manuel Arellano-Quintana and A. Franchi. A novel experimental model and a drag-optimal allocation method for variable-pitch propellers in multirotors. *IEEE Access*, 6, 2018.

APPENDIX A

MODEL PARAMETERS

A.1 Aircraft Weight and Balance Parameters

Mass and moment of inertia properties are listed in Table A.1, below.

Parameter	**Unit**	**Value**
Mass	kg	1000
I_{xx}	$kg.m^2$	1060.6
I_{yy}	$kg.m^2$	3160.6
I_{zz}	$kg.m^2$	3305.8

Table A.1: Weight and balance parameters

Moment of inertia values in Table A.1 are estimated from the geometry of the eVTOL aircraft (Fig. 3.2) and it is calculated with respect to the body-axis frame (Fig. 3.3). It is assumed that all product of inertia terms (I_{xy}, I_{yz}, etc.) are zero. The inertia matrix is expressed below with all of its elements.

$$I = \begin{bmatrix} 1060.6 & 0 & 0 \\ 0 & 3160.6 & 0 \\ 0 & 0 & 3305.8 \end{bmatrix}$$

A.2 Single Blade Aerodynamic Coefficients

Aerodynamic coefficients of NACA-0012, which is used for rotor blades of the eV-TOL aircraft, is shown in Fig. A.1.

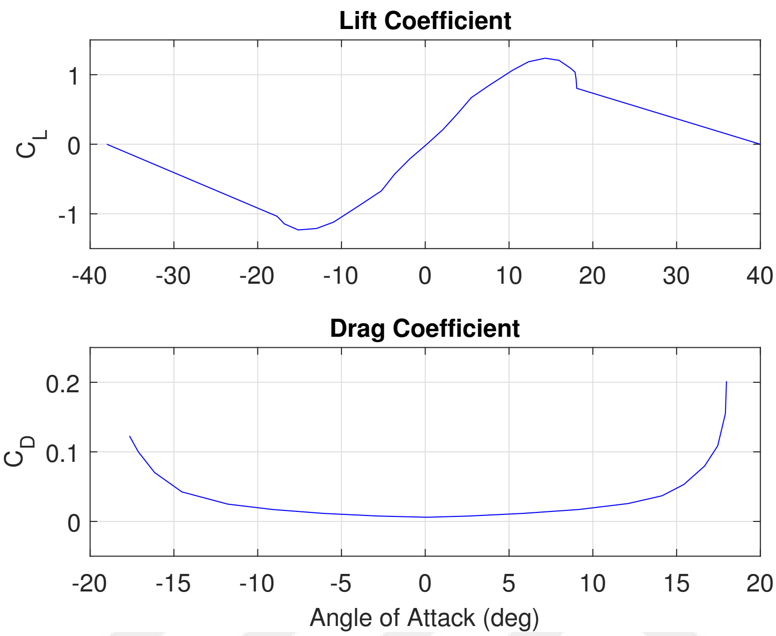

Figure A.1: Lift and drag coefficient graphs

A.3 Thrust and Torque Coefficients of Control Allocation Matrix

Thrust coefficient (C_T) and torque coefficient (C_Q) are obtained by applying 3-D body-frame velocity sweeps to isolated rotor model of the eVTOL aircraft. At each combination of body-velocities, steady-state simulations are conducted by applying rotational speed sweep from "0 RPM" to "3600 RPM" to the rotor. Then, "RPM vs thrust" and "RPM vs torque" curves are obtained by collecting the resultant thrust and torque values for each rotational speed. A curve fitting is applied to these curves in order to obtain the thrust and torque deviation with rotational speed change in the form of "$T = C_T\Omega^2$" and "$Q = C_Q\Omega^2$". A sample calculation is provided in Section-A.3.1.

Body-frame velocity sweeps are applied as following:

- **U**: -80 knots to 80 knots with increments of 20 knots

- **V**: -80 knots to 80 knots with increments of 20 knots

- **W**: -1500 ft/min to 1500 ft/min with increments of 300 ft/min

Results are tabulated in Sections-A.3.2 and A.3.3.

A.3.1 Sample Calculation

Consider a hover condition where all of the body-frame velocities are zero
$(\mathrm{U} = \mathrm{V} = \mathrm{W} = 0)$.

Resultant thrust curve and the corresponding curve-fitting is shown in Fig. A.2. Thrust values are negative since force vector is calculated with respect to the hub-frame (Fig. 3.4) where the positive z-axis direction is towards downward. Equation of the thrust curve (Fig. A.2) is given as the following:

$$T = f(\Omega) = (-0.00166)\Omega^2$$

This value can be read from Table A.7.

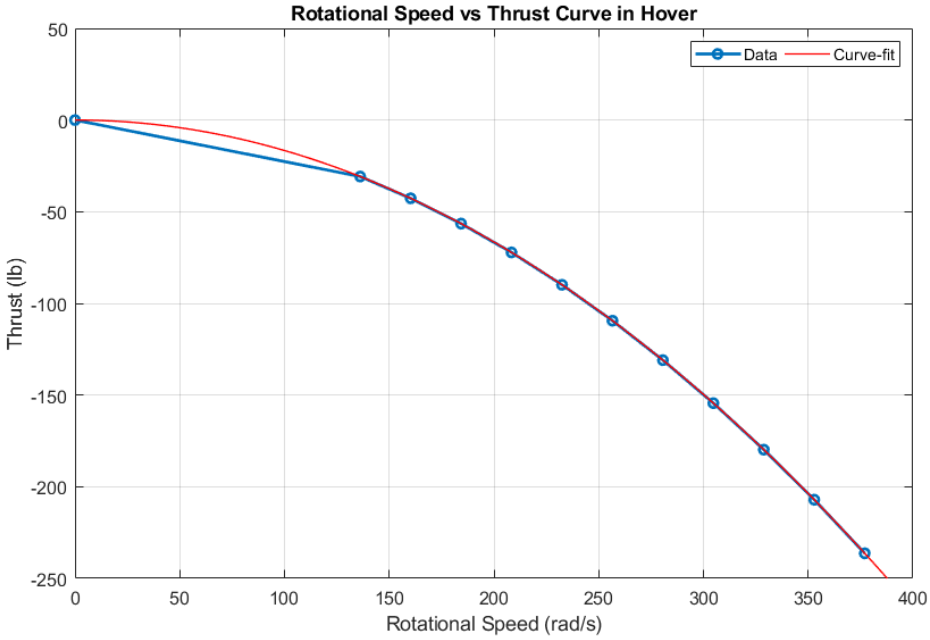

Figure A.2: Thrust curve for hover

A.3.2 Thrust Tables

U/V	-80	-60	-40	-20	0	20	40	60	80
-80	-0.00238	-0.00235	-0.00231	-0.00208	-0.00198	-0.00208	-0.00231	-0.00235	-0.00238
-60	-0.00235	-0.00224	-0.00172	-0.00216	-0.00213	-0.00216	-0.00172	-0.00224	-0.00235
-40	-0.00231	-0.00172	-0.00210	-0.00200	-0.00195	-0.00200	-0.00210	-0.00172	-0.00231
-20	-0.00208	-0.00216	-0.00200	-0.00185	-0.00179	-0.00185	-0.00200	-0.00216	-0.00208
0	-0.00198	-0.00213	-0.00195	-0.00179	-0.00174	-0.00179	-0.00195	-0.00213	-0.00198
20	-0.00208	-0.00216	-0.00200	-0.00185	-0.00179	-0.00185	-0.00200	-0.00216	-0.00208
40	-0.00231	-0.00172	-0.00210	-0.00200	-0.00195	-0.00200	-0.00210	-0.00172	-0.00231
60	-0.00235	-0.00224	-0.00172	-0.00216	-0.00213	-0.00216	-0.00172	-0.00224	-0.00235
80	-0.00238	-0.00235	-0.00231	-0.00208	-0.00198	-0.00208	-0.00231	-0.00235	-0.00238

Table A.2: Single rotor thrust coefficients at "W=-1500 ft/min"

U/V	-80	-60	-40	-20	0	20	40	60	80
-80	-0.00238	-0.00234	-0.00230	-0.00226	-0.00224	-0.00226	-0.00230	-0.00234	-0.00238
-60	-0.00234	-0.00227	-0.00219	-0.00212	-0.00209	-0.00212	-0.00219	-0.00227	-0.00234
-40	-0.00230	-0.00219	-0.00206	-0.00194	-0.00189	-0.00194	-0.00206	-0.00219	-0.00230
-20	-0.00226	-0.00212	-0.00194	-0.00178	-0.00173	-0.00178	-0.00194	-0.00212	-0.00226
0	-0.00224	-0.00209	-0.00189	-0.00173	-0.00171	-0.00173	-0.00189	-0.00209	-0.00224
20	-0.00226	-0.00212	-0.00194	-0.00178	-0.00173	-0.00178	-0.00194	-0.00212	-0.00226
40	-0.00230	-0.00219	-0.00206	-0.00194	-0.00189	-0.00194	-0.00206	-0.00219	-0.00230
60	-0.00234	-0.00227	-0.00219	-0.00212	-0.00209	-0.00212	-0.00219	-0.00227	-0.00234
80	-0.00238	-0.00234	-0.00230	-0.00226	-0.00224	-0.00226	-0.00230	-0.00234	-0.00238

Table A.3: Single rotor thrust coefficients at "W=-1200 ft/min"

U/V	-80	-60	-40	-20	0	20	40	60	80
-80	-0.00238	-0.00233	-0.00228	-0.00224	-0.00222	-0.00224	-0.00228	-0.00233	-0.00238
-60	-0.00233	-0.00225	-0.00216	-0.00208	-0.00204	-0.00208	-0.00216	-0.00225	-0.00233
-40	-0.00228	-0.00216	-0.00201	-0.00187	-0.00182	-0.00187	-0.00201	-0.00216	-0.00228
-20	-0.00224	-0.00208	-0.00187	-0.00171	-0.00167	-0.00171	-0.00187	-0.00208	-0.00224
0	-0.00222	-0.00204	-0.00182	-0.00167	-0.00169	-0.00167	-0.00182	-0.00204	-0.00222
20	-0.00224	-0.00208	-0.00187	-0.00171	-0.00167	-0.00171	-0.00187	-0.00208	-0.00224
40	-0.00228	-0.00216	-0.00201	-0.00187	-0.00182	-0.00187	-0.00201	-0.00216	-0.00228
60	-0.00233	-0.00225	-0.00216	-0.00208	-0.00204	-0.00208	-0.00216	-0.00225	-0.00233
80	-0.00238	-0.00233	-0.00228	-0.00224	-0.00222	-0.00224	-0.00228	-0.00233	-0.00238

Table A.4: Single rotor thrust coefficients at "W=-900 ft/min"

U/V	-80	-60	-40	-20	0	20	40	60	80
-80	-0.00239	-0.00233	-0.00227	-0.00222	-0.00220	-0.00222	-0.00227	-0.00233	-0.00239
-60	-0.00233	-0.00224	-0.00213	-0.00204	-0.00200	-0.00204	-0.00213	-0.00224	-0.00233
-40	-0.00227	-0.00213	-0.00196	-0.00181	-0.00175	-0.00181	-0.00196	-0.00213	-0.00227
-20	-0.00222	-0.00204	-0.00181	-0.00164	-0.00161	-0.00164	-0.00181	-0.00204	-0.00222
0	-0.00220	-0.00200	-0.00175	-0.00161	-0.00167	-0.00161	-0.00175	-0.00200	-0.00220
20	-0.00222	-0.00204	-0.00181	-0.00164	-0.00161	-0.00164	-0.00181	-0.00204	-0.00222
40	-0.00227	-0.00213	-0.00196	-0.00181	-0.00175	-0.00181	-0.00196	-0.00213	-0.00227
60	-0.00233	-0.00224	-0.00213	-0.00204	-0.00200	-0.00204	-0.00213	-0.00224	-0.00233
80	-0.00239	-0.00233	-0.00227	-0.00222	-0.00220	-0.00222	-0.00227	-0.00233	-0.00239

Table A.5: Single rotor thrust coefficients at "W=-600 ft/min"

U/V	-80	-60	-40	-20	0	20	40	60	80
-80	-0.00239	-0.00233	-0.00226	-0.00221	-0.00219	-0.00221	-0.00226	-0.00233	-0.00239
-60	-0.00233	-0.00223	-0.00211	-0.00201	-0.00197	-0.00201	-0.00211	-0.00223	-0.00233
-40	-0.00226	-0.00211	-0.00193	-0.00176	-0.00170	-0.00176	-0.00193	-0.00211	-0.00226
-20	-0.00221	-0.00201	-0.00176	-0.00157	-0.00155	-0.00157	-0.00176	-0.00201	-0.00221
0	-0.00219	-0.00197	-0.00170	-0.00155	-0.00167	-0.00155	-0.00170	-0.00197	-0.00219
20	-0.00221	-0.00201	-0.00176	-0.00157	-0.00155	-0.00157	-0.00176	-0.00201	-0.00221
40	-0.00226	-0.00211	-0.00193	-0.00176	-0.00170	-0.00176	-0.00193	-0.00211	-0.00226
60	-0.00233	-0.00223	-0.00211	-0.00201	-0.00197	-0.00201	-0.00211	-0.00223	-0.00233
80	-0.00239	-0.00233	-0.00226	-0.00221	-0.00219	-0.00221	-0.00226	-0.00233	-0.00239

Table A.6: Single rotor thrust coefficients at "W=-300 ft/min"

U/V	-80	-60	-40	-20	0	20	40	60	80
-80	-0.00240	-0.00233	-0.00226	-0.00220	-0.00218	-0.00220	-0.00226	-0.00233	-0.00240
-60	-0.00233	-0.00222	-0.00210	-0.00199	-0.00195	-0.00199	-0.00210	-0.00222	-0.00233
-40	-0.00226	-0.00210	-0.00190	-0.00172	-0.00165	-0.00172	-0.00190	-0.00210	-0.00226
-20	-0.00220	-0.00199	-0.00172	-0.00151	-0.00149	-0.00151	-0.00172	-0.00199	-0.00220
0	-0.00218	-0.00195	-0.00165	-0.00149	-0.00166	-0.00149	-0.00165	-0.00195	-0.00218
20	-0.00220	-0.00199	-0.00172	-0.00151	-0.00149	-0.00151	-0.00172	-0.00199	-0.00220
40	-0.00226	-0.00210	-0.00190	-0.00172	-0.00165	-0.00172	-0.00190	-0.00210	-0.00226
60	-0.00233	-0.00222	-0.00210	-0.00199	-0.00195	-0.00199	-0.00210	-0.00222	-0.00233
80	-0.00240	-0.00233	-0.00226	-0.00220	-0.00218	-0.00220	-0.00226	-0.00233	-0.00240

Table A.7: Single rotor thrust coefficients at "W=0 ft/min"

U/V	-80	-60	-40	-20	0	20	40	60	80
-80	-0.00242	-0.00234	-0.00227	-0.00220	-0.00218	-0.00220	-0.00227	-0.00234	-0.00242
-60	-0.00234	-0.00223	-0.00209	-0.00198	-0.00193	-0.00198	-0.00209	-0.00223	-0.00234
-40	-0.00227	-0.00209	-0.00188	-0.00168	-0.00160	-0.00168	-0.00188	-0.00209	-0.00227
-20	-0.00220	-0.00198	-0.00168	-0.00145	-0.00143	-0.00145	-0.00168	-0.00198	-0.00220
0	-0.00218	-0.00193	-0.00160	-0.00143	-0.00167	-0.00143	-0.00160	-0.00193	-0.00218
20	-0.00220	-0.00198	-0.00168	-0.00145	-0.00143	-0.00145	-0.00168	-0.00198	-0.00220
40	-0.00227	-0.00209	-0.00188	-0.00168	-0.00160	-0.00168	-0.00188	-0.00209	-0.00227
60	-0.00234	-0.00223	-0.00209	-0.00198	-0.00193	-0.00198	-0.00209	-0.00223	-0.00234
80	-0.00242	-0.00234	-0.00227	-0.00220	-0.00218	-0.00220	-0.00227	-0.00234	-0.00242

Table A.8: Single rotor thrust coefficients at "W=300 ft/min"

U/V	-80	-60	-40	-20	0	20	40	60	80
-80	-0.00244	-0.00236	-0.00228	-0.00221	-0.00218	-0.00221	-0.00228	-0.00236	-0.00244
-60	-0.00236	-0.00223	-0.00209	-0.00196	-0.00191	-0.00196	-0.00209	-0.00223	-0.00236
-40	-0.00228	-0.00209	-0.00185	-0.00164	-0.00156	-0.00164	-0.00185	-0.00209	-0.00228
-20	-0.00221	-0.00196	-0.00164	-0.00139	-0.00138	-0.00139	-0.00164	-0.00196	-0.00221
0	-0.00218	-0.00191	-0.00156	-0.00138	-0.00167	-0.00138	-0.00156	-0.00191	-0.00218
20	-0.00221	-0.00196	-0.00164	-0.00139	-0.00138	-0.00139	-0.00164	-0.00196	-0.00221
40	-0.00228	-0.00209	-0.00185	-0.00164	-0.00156	-0.00164	-0.00185	-0.00209	-0.00228
60	-0.00236	-0.00223	-0.00209	-0.00196	-0.00191	-0.00196	-0.00209	-0.00223	-0.00236
80	-0.00244	-0.00236	-0.00228	-0.00221	-0.00218	-0.00221	-0.00228	-0.00236	-0.00244

Table A.9: Single rotor thrust coefficients at "W=600 ft/min"

U/V	-80	-60	-40	-20	0	20	40	60	80
-80	-0.00248	-0.00239	-0.00229	-0.00222	-0.00219	-0.00222	-0.00229	-0.00239	-0.00248
-60	-0.00239	-0.00225	-0.00209	-0.00195	-0.00190	-0.00195	-0.00209	-0.00225	-0.00239
-40	-0.00229	-0.00209	-0.00184	-0.00161	-0.00152	-0.00161	-0.00184	-0.00209	-0.00229
-20	-0.00222	-0.00195	-0.00161	-0.00134	-0.00133	-0.00134	-0.00161	-0.00195	-0.00222
0	-0.00219	-0.00190	-0.00152	-0.00133	-0.00169	-0.00133	-0.00152	-0.00190	-0.00219
20	-0.00222	-0.00195	-0.00161	-0.00134	-0.00133	-0.00134	-0.00161	-0.00195	-0.00222
40	-0.00229	-0.00209	-0.00184	-0.00161	-0.00152	-0.00161	-0.00184	-0.00209	-0.00229
60	-0.00239	-0.00225	-0.00209	-0.00195	-0.00190	-0.00195	-0.00209	-0.00225	-0.00239
80	-0.00248	-0.00239	-0.00229	-0.00222	-0.00219	-0.00222	-0.00229	-0.00239	-0.00248

Table A.10: Single rotor thrust coefficients at "W=900 ft/min"

U/V	-80	-60	-40	-20	0	20	40	60	80
-80	-0.00252	-0.00243	-0.00233	-0.00225	-0.00222	-0.00225	-0.00233	-0.00243	-0.00252
-60	-0.00243	-0.00228	-0.00211	-0.00197	-0.00191	-0.00197	-0.00211	-0.00228	-0.00243
-40	-0.00233	-0.00211	-0.00184	-0.00159	-0.00149	-0.00159	-0.00184	-0.00211	-0.00233
-20	-0.00225	-0.00197	-0.00159	-0.00130	-0.00129	-0.00130	-0.00159	-0.00197	-0.00225
0	-0.00222	-0.00191	-0.00149	-0.00129	-0.00171	-0.00129	-0.00149	-0.00191	-0.00222
20	-0.00225	-0.00197	-0.00159	-0.00130	-0.00129	-0.00130	-0.00159	-0.00197	-0.00225
40	-0.00233	-0.00211	-0.00184	-0.00159	-0.00149	-0.00159	-0.00184	-0.00211	-0.00233
60	-0.00243	-0.00228	-0.00211	-0.00197	-0.00191	-0.00197	-0.00211	-0.00228	-0.00243
80	-0.00252	-0.00243	-0.00233	-0.00225	-0.00222	-0.00225	-0.00233	-0.00243	-0.00252

Table A.11: Single rotor thrust coefficients at "W=1200 ft/min"

U/V	-80	-60	-40	-20	0	20	40	60	80
-80	-0.00258	-0.00249	-0.00239	-0.00230	-0.00227	-0.00230	-0.00239	-0.00249	-0.00258
-60	-0.00249	-0.00233	-0.00216	-0.00201	-0.00194	-0.00201	-0.00216	-0.00233	-0.00249
-40	-0.00239	-0.00216	-0.00187	-0.00160	-0.00148	-0.00160	-0.00187	-0.00216	-0.00239
-20	-0.00230	-0.00201	-0.00160	-0.00126	-0.00125	-0.00126	-0.00160	-0.00201	-0.00230
0	-0.00227	-0.00194	-0.00148	-0.00125	-0.00173	-0.00125	-0.00148	-0.00194	-0.00227
20	-0.00230	-0.00201	-0.00160	-0.00126	-0.00125	-0.00126	-0.00160	-0.00201	-0.00230
40	-0.00239	-0.00216	-0.00187	-0.00160	-0.00148	-0.00160	-0.00187	-0.00216	-0.00239
60	-0.00249	-0.00233	-0.00216	-0.00201	-0.00194	-0.00201	-0.00216	-0.00233	-0.00249
80	-0.00258	-0.00249	-0.00239	-0.00230	-0.00227	-0.00230	-0.00239	-0.00249	-0.00258

Table A.12: Single rotor thrust coefficients at "W=1500 ft/min"

A.3.3 Torque Tables

U/V	-80	-60	-40	-20	0	20	40	60	80
-80	-0.00025	-0.00026	-0.00027	-0.00027	-0.00027	-0.00027	-0.00027	-0.00026	-0.00025
-60	-0.00026	-0.00027	-0.00026	-0.00028	-0.00028	-0.00028	-0.00026	-0.00027	-0.00026
-40	-0.00027	-0.00026	-0.00029	-0.00029	-0.00029	-0.00029	-0.00029	-0.00026	-0.00027
-20	-0.00027	-0.00028	-0.00029	-0.00030	-0.00031	-0.00030	-0.00029	-0.00028	-0.00027
0	-0.00027	-0.00028	-0.00029	-0.00031	-0.00031	-0.00031	-0.00029	-0.00028	-0.00027
20	-0.00027	-0.00028	-0.00029	-0.00030	-0.00031	-0.00030	-0.00029	-0.00028	-0.00027
40	-0.00027	-0.00026	-0.00029	-0.00029	-0.00029	-0.00029	-0.00029	-0.00026	-0.00027
60	-0.00026	-0.00027	-0.00026	-0.00028	-0.00028	-0.00028	-0.00026	-0.00027	-0.00026
80	-0.00025	-0.00026	-0.00027	-0.00027	-0.00027	-0.00027	-0.00027	-0.00026	-0.00025

Table A.13: Single rotor torque coefficients at "W=-1500 ft/min"

U/V	-80	-60	-40	-20	0	20	40	60	80
-80	-0.00024	-0.00025	-0.00026	-0.00026	-0.00027	-0.00026	-0.00026	-0.00025	-0.00024
-60	-0.00025	-0.00026	-0.00027	-0.00027	-0.00028	-0.00027	-0.00027	-0.00026	-0.00025
-40	-0.00026	-0.00027	-0.00028	-0.00028	-0.00028	-0.00028	-0.00028	-0.00027	-0.00026
-20	-0.00026	-0.00027	-0.00028	-0.00029	-0.00029	-0.00029	-0.00028	-0.00027	-0.00026
0	-0.00027	-0.00028	-0.00028	-0.00029	-0.00030	-0.00029	-0.00028	-0.00028	-0.00027
20	-0.00026	-0.00027	-0.00028	-0.00029	-0.00029	-0.00029	-0.00028	-0.00027	-0.00026
40	-0.00026	-0.00027	-0.00028	-0.00028	-0.00028	-0.00028	-0.00028	-0.00027	-0.00026
60	-0.00025	-0.00026	-0.00027	-0.00027	-0.00028	-0.00027	-0.00027	-0.00026	-0.00025
80	-0.00024	-0.00025	-0.00026	-0.00026	-0.00027	-0.00026	-0.00026	-0.00025	-0.00024

Table A.14: Single rotor torque coefficients at "W=-1200 ft/min"

U/V	-80	-60	-40	-20	0	20	40	60	80
-80	-0.00023	-0.00025	-0.00026	-0.00026	-0.00026	-0.00026	-0.00026	-0.00025	-0.00023
-60	-0.00025	-0.00026	-0.00027	-0.00027	-0.00027	-0.00027	-0.00027	-0.00026	-0.00025
-40	-0.00026	-0.00027	-0.00027	-0.00028	-0.00028	-0.00028	-0.00027	-0.00027	-0.00026
-20	-0.00026	-0.00027	-0.00028	-0.00028	-0.00028	-0.00028	-0.00028	-0.00027	-0.00026
0	-0.00026	-0.00027	-0.00028	-0.00028	-0.00029	-0.00028	-0.00028	-0.00027	-0.00026
20	-0.00026	-0.00027	-0.00028	-0.00028	-0.00028	-0.00028	-0.00028	-0.00027	-0.00026
40	-0.00026	-0.00027	-0.00027	-0.00028	-0.00028	-0.00028	-0.00027	-0.00027	-0.00026
60	-0.00025	-0.00026	-0.00027	-0.00027	-0.00027	-0.00027	-0.00027	-0.00026	-0.00025
80	-0.00023	-0.00025	-0.00026	-0.00026	-0.00026	-0.00026	-0.00026	-0.00025	-0.00023

Table A.15: Single rotor torque coefficients at "W=-900 ft/min"

U/V	-80	-60	-40	-20	0	20	40	60	80
-80	-0.00023	-0.00025	-0.00026	-0.00026	-0.00027	-0.00026	-0.00026	-0.00025	-0.00023
-60	-0.00025	-0.00026	-0.00027	-0.00028	-0.00028	-0.00028	-0.00027	-0.00026	-0.00025
-40	-0.00026	-0.00027	-0.00028	-0.00028	-0.00028	-0.00028	-0.00028	-0.00027	-0.00026
-20	-0.00026	-0.00028	-0.00028	-0.00028	-0.00028	-0.00028	-0.00028	-0.00028	-0.00026
0	-0.00027	-0.00028	-0.00028	-0.00028	-0.00029	-0.00028	-0.00028	-0.00028	-0.00027
20	-0.00026	-0.00028	-0.00028	-0.00028	-0.00028	-0.00028	-0.00028	-0.00028	-0.00026
40	-0.00026	-0.00027	-0.00028	-0.00028	-0.00028	-0.00028	-0.00028	-0.00027	-0.00026
60	-0.00025	-0.00026	-0.00027	-0.00028	-0.00028	-0.00028	-0.00027	-0.00026	-0.00025
80	-0.00023	-0.00025	-0.00026	-0.00026	-0.00027	-0.00026	-0.00026	-0.00025	-0.00023

Table A.16: Single rotor torque coefficients at "W=-600 ft/min"

U/V	-80	-60	-40	-20	0	20	40	60	80
-80	-0.00024	-0.00025	-0.00027	-0.00027	-0.00028	-0.00027	-0.00027	-0.00025	-0.00024
-60	-0.00025	-0.00027	-0.00028	-0.00029	-0.00029	-0.00029	-0.00028	-0.00027	-0.00025
-40	-0.00027	-0.00028	-0.00029	-0.00029	-0.00029	-0.00029	-0.00029	-0.00028	-0.00027
-20	-0.00027	-0.00029	-0.00029	-0.00028	-0.00028	-0.00028	-0.00029	-0.00029	-0.00027
0	-0.00028	-0.00029	-0.00029	-0.00028	-0.00028	-0.00028	-0.00029	-0.00029	-0.00028
20	-0.00027	-0.00029	-0.00029	-0.00028	-0.00028	-0.00028	-0.00029	-0.00029	-0.00027
40	-0.00027	-0.00028	-0.00029	-0.00029	-0.00029	-0.00029	-0.00029	-0.00028	-0.00027
60	-0.00025	-0.00027	-0.00028	-0.00029	-0.00029	-0.00029	-0.00028	-0.00027	-0.00025
80	-0.00024	-0.00025	-0.00027	-0.00027	-0.00028	-0.00027	-0.00027	-0.00025	-0.00024

Table A.17: Single rotor torque coefficients at "W=-300 ft/min"

U/V	-80	-60	-40	-20	0	20	40	60	80
-80	-0.00025	-0.00026	-0.00028	-0.00029	-0.00029	-0.00029	-0.00028	-0.00026	-0.00025
-60	-0.00026	-0.00028	-0.00030	-0.00031	-0.00031	-0.00031	-0.00030	-0.00028	-0.00026
-40	-0.00028	-0.00030	-0.00031	-0.00031	-0.00031	-0.00031	-0.00031	-0.00030	-0.00028
-20	-0.00029	-0.00031	-0.00031	-0.00029	-0.00028	-0.00029	-0.00031	-0.00031	-0.00029
0	-0.00029	-0.00031	-0.00031	-0.00028	-0.00028	-0.00028	-0.00031	-0.00031	-0.00029
20	-0.00029	-0.00031	-0.00031	-0.00029	-0.00028	-0.00029	-0.00031	-0.00031	-0.00029
40	-0.00028	-0.00030	-0.00031	-0.00031	-0.00031	-0.00031	-0.00031	-0.00030	-0.00028
60	-0.00026	-0.00028	-0.00030	-0.00031	-0.00031	-0.00031	-0.00030	-0.00028	-0.00026
80	-0.00025	-0.00026	-0.00028	-0.00029	-0.00029	-0.00029	-0.00028	-0.00026	-0.00025

Table A.18: Single rotor torque coefficients at "W=0 ft/min"

U/V	-80	-60	-40	-20	0	20	40	60	80
-80	-0.00024	-0.00026	-0.00028	-0.00029	-0.00030	-0.00029	-0.00028	-0.00026	-0.00024
-60	-0.00026	-0.00029	-0.00031	-0.00032	-0.00033	-0.00032	-0.00031	-0.00029	-0.00026
-40	-0.00028	-0.00031	-0.00033	-0.00033	-0.00033	-0.00033	-0.00033	-0.00031	-0.00028
-20	-0.00029	-0.00032	-0.00033	-0.00031	-0.00029	-0.00031	-0.00033	-0.00032	-0.00029
0	-0.00030	-0.00033	-0.00033	-0.00029	-0.00028	-0.00029	-0.00033	-0.00033	-0.00030
20	-0.00029	-0.00032	-0.00033	-0.00031	-0.00029	-0.00031	-0.00033	-0.00032	-0.00029
40	-0.00028	-0.00031	-0.00033	-0.00033	-0.00033	-0.00033	-0.00033	-0.00031	-0.00028
60	-0.00026	-0.00029	-0.00031	-0.00032	-0.00033	-0.00032	-0.00031	-0.00029	-0.00026
80	-0.00024	-0.00026	-0.00028	-0.00029	-0.00030	-0.00029	-0.00028	-0.00026	-0.00024

Table A.19: Single rotor torque coefficients at "W=300 ft/min"

U/V	-80	-60	-40	-20	0	20	40	60	80
-80	-0.00026	-0.00029	-0.00031	-0.00032	-0.00033	-0.00032	-0.00031	-0.00029	-0.00026
-60	-0.00029	-0.00032	-0.00034	-0.00036	-0.00036	-0.00036	-0.00034	-0.00032	-0.00029
-40	-0.00031	-0.00034	-0.00036	-0.00037	-0.00036	-0.00037	-0.00036	-0.00034	-0.00031
-20	-0.00032	-0.00036	-0.00037	-0.00034	-0.00031	-0.00034	-0.00037	-0.00036	-0.00032
0	-0.00033	-0.00036	-0.00036	-0.00031	-0.00028	-0.00031	-0.00036	-0.00036	-0.00033
20	-0.00032	-0.00036	-0.00037	-0.00034	-0.00031	-0.00034	-0.00037	-0.00036	-0.00032
40	-0.00031	-0.00034	-0.00036	-0.00037	-0.00036	-0.00037	-0.00036	-0.00034	-0.00031
60	-0.00029	-0.00032	-0.00034	-0.00036	-0.00036	-0.00036	-0.00034	-0.00032	-0.00029
80	-0.00026	-0.00029	-0.00031	-0.00032	-0.00033	-0.00032	-0.00031	-0.00029	-0.00026

Table A.20: Single rotor torque coefficients at "W=600 ft/min"

U/V	-80	-60	-40	-20	0	20	40	60	80
-80	-0.00028	-0.00032	-0.00034	-0.00036	-0.00036	-0.00036	-0.00034	-0.00032	-0.00028
-60	-0.00032	-0.00035	-0.00038	-0.00040	-0.00040	-0.00040	-0.00038	-0.00035	-0.00032
-40	-0.00034	-0.00038	-0.00041	-0.00041	-0.00041	-0.00041	-0.00041	-0.00038	-0.00034
-20	-0.00036	-0.00040	-0.00041	-0.00037	-0.00033	-0.00037	-0.00041	-0.00040	-0.00036
0	-0.00036	-0.00040	-0.00041	-0.00033	-0.00029	-0.00033	-0.00041	-0.00040	-0.00036
20	-0.00036	-0.00040	-0.00041	-0.00037	-0.00033	-0.00037	-0.00041	-0.00040	-0.00036
40	-0.00034	-0.00038	-0.00041	-0.00041	-0.00041	-0.00041	-0.00041	-0.00038	-0.00034
60	-0.00032	-0.00035	-0.00038	-0.00040	-0.00040	-0.00040	-0.00038	-0.00035	-0.00032
80	-0.00028	-0.00032	-0.00034	-0.00036	-0.00036	-0.00036	-0.00034	-0.00032	-0.00028

Table A.21: Single rotor torque coefficients at "W=900 ft/min"

U/V	-80	-60	-40	-20	0	20	40	60	80
-80	-0.00031	-0.00035	-0.00038	-0.00040	-0.00041	-0.00040	-0.00038	-0.00035	-0.00031
-60	-0.00035	-0.00040	-0.00043	-0.00045	-0.00046	-0.00045	-0.00043	-0.00040	-0.00035
-40	-0.00038	-0.00043	-0.00046	-0.00047	-0.00046	-0.00047	-0.00046	-0.00043	-0.00038
-20	-0.00040	-0.00045	-0.00047	-0.00041	-0.00036	-0.00041	-0.00047	-0.00045	-0.00040
0	-0.00041	-0.00046	-0.00046	-0.00036	-0.00029	-0.00036	-0.00046	-0.00046	-0.00041
20	-0.00040	-0.00045	-0.00047	-0.00041	-0.00036	-0.00041	-0.00047	-0.00045	-0.00040
40	-0.00038	-0.00043	-0.00046	-0.00047	-0.00046	-0.00047	-0.00046	-0.00043	-0.00038
60	-0.00035	-0.00040	-0.00043	-0.00045	-0.00046	-0.00045	-0.00043	-0.00040	-0.00035
80	-0.00031	-0.00035	-0.00038	-0.00040	-0.00041	-0.00040	-0.00038	-0.00035	-0.00031

Table A.22: Single rotor torque coefficients at "W=1200 ft/min"

U/V	-80	-60	-40	-20	0	20	40	60	80
-80	-0.00035	-0.00039	-0.00043	-0.00045	-0.00046	-0.00045	-0.00043	-0.00039	-0.00035
-60	-0.00039	-0.00044	-0.00048	-0.00051	-0.00051	-0.00051	-0.00048	-0.00044	-0.00039
-40	-0.00043	-0.00048	-0.00052	-0.00052	-0.00052	-0.00052	-0.00052	-0.00048	-0.00043
-20	-0.00045	-0.00051	-0.00052	-0.00046	-0.00039	-0.00046	-0.00052	-0.00051	-0.00045
0	-0.00046	-0.00051	-0.00052	-0.00039	-0.00029	-0.00039	-0.00052	-0.00051	-0.00046
20	-0.00045	-0.00051	-0.00052	-0.00046	-0.00039	-0.00046	-0.00052	-0.00051	-0.00045
40	-0.00043	-0.00048	-0.00052	-0.00052	-0.00052	-0.00052	-0.00052	-0.00048	-0.00043
60	-0.00039	-0.00044	-0.00048	-0.00051	-0.00051	-0.00051	-0.00048	-0.00044	-0.00039
80	-0.00035	-0.00039	-0.00043	-0.00045	-0.00046	-0.00045	-0.00043	-0.00039	-0.00035

Table A.23: Single rotor torque coefficients at "W=1500 ft/min"

A.4 Calculation of Rotor Rotational Speed References

Desired virtual input reference ($\Omega'_{\mathrm{ref_d}}$) consists of constant values. These values are estimated from the hover trim condition of the eVTOL aircraft. Firstly, rotational speed of a single rotor in steady-state hover condition is calculated. This value is assigned to all elements of "$\Omega_{\mathrm{ref_d}}$" (actual desired rotational speed input) since all rotors share the load equally in hover. Then these values are converted to virtual inputs by using the relation "$\Omega'_{\mathrm{ref}} = \Omega^2_{\mathrm{ref}}$" and final form of the desired virtual input reference is obtained.

The aircraft gross weight is 1000 kg (2205 lbf) from Table A.1 in Section-A.1. Then, required thrust of a single rotor in hover is calculated below.

$$\frac{weight}{20} = \frac{2205}{20} = 110\ lbf$$

Remember that the eVTOL aircraft has 20 rotors.

The corresponding rotational speed value is estimated by using the relation,

$$T = C_T \Omega^2$$

This relation is also used for control allocation matrix in Eq. (2.7) in Chapter-2.2.

Thrust coefficient can be obtained from the tables in Section-A.3.2. The aircraft is stationary in hover, then Table A.7 should be considered where all velocity components are zero. From the table, magnitude of the thrust coefficient ($\mathrm{C_T}$) in hover is "0.00166".

Having obtained all of the parameters required, the rotational speed is calculated as:

$$\Omega = \sqrt{\frac{T}{C_T}} = \sqrt{\frac{110}{0.00166}} = 257.5\ rad/s\ (2459\ RPM)$$

Then, all elements of actual desired input ($\Omega_{\mathrm{ref_d}}$) are set to this value. Finally, desired virtual input reference ($\Omega'_{\mathrm{ref\,d}}$) is obtained as the following:

$$\Omega'_{ref\,d} = \Omega^2_{ref_d} = (257.5)^2 = 66311\ \frac{rad^2}{s^2}$$

where "$\Omega'_{\mathrm{ref\,d}} \in \Re^{20}$" and all of its elements have the same value.

A.5 Mapping of Pilot Controls

Pilot controls are linearly mapped to specific values that are found subjectively by flying the aircraft in the real-time simulation. The main focus is to satisfy sufficient handling qualities during flight. The mapping intervals are tabulated in Table A.24.

Variable	**Input Unit**	**Output Unit**	**Input Interval**	**Output Interval**
$\mathrm{M_x}$	norm	lb.ft	[-1, 1]	[-10000, 10000]
$\mathrm{M_y}$	norm	lb.ft	[-1, 1]	[-10000, 10000]
$\mathrm{M_z}$	norm	lb.ft	[-1, 1]	[-300, 300]
T	norm	lb	[0, 1]	[0, -4000]

Table A.24: Linear mapping of desired input values

A.6 Selection of Weight Matrices

To decide weight matrix elements, the control allocation structure which is expressed in Eq. (2.6) in Chapter-2.2.1 is used. It is expressed below:

$$R\Omega'_{ref} = D$$

This equation is used to determine weight matrices such that the desired matrix "D" must be satisfied by the control solution "Ω'_{ref}" which is calculated from the Blended-Inverse equation (Eq. (2.17)) in Chapter-2.2.2.

For this verification, the following steps are followed respectively:

1) Normalized pilot control input is applied between limits of its interval

2) Desired thrust and moments vector "D" described in Section-A.5 is obtained from the pilot control

3) Control solution (Ω'_{ref}) is calculated from the Blended-Inverse equation (Eq. (2.17))

4) Expected thrust and moment outputs are calculated by using the control allocation equation (Eq. (2.6))

5) Desired thrust and moments vector "D" and the expected values found in item-4 are compared

A related flow chart describing those steps are shown in Fig. A.3. The comparison of item-5 above provides an indication that whether the desired thrust and moments can be generated by the current control solution (Ω'_{ref}) or not. The weight matrix "F" directly affects this result. Therefore, "F" is found by using this comparison such that "Ω'_{ref}" vector become able to generate the desired vector "D".

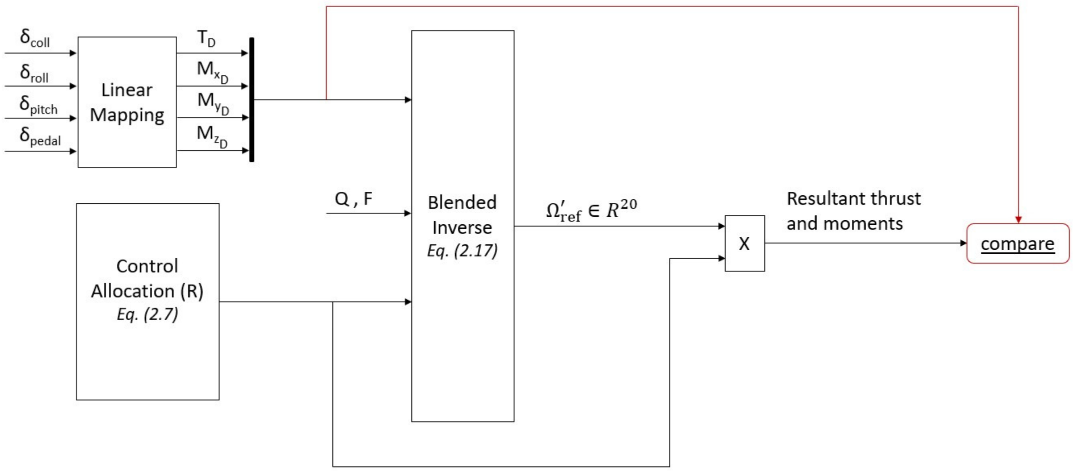

Figure A.3: Flow chart of the output verification

Using the approach explained above, the weight matrix "$F \in \Re^{4\times4}$" is selected as a diagonal matrix such that its diagonal elements are as following:

$$diag_{[F]} = [400 \; 20 \; 20 \; 100000]$$

where the corresponding comparisons are shown in Figs. A.4, A.5, A.6 and A.7.

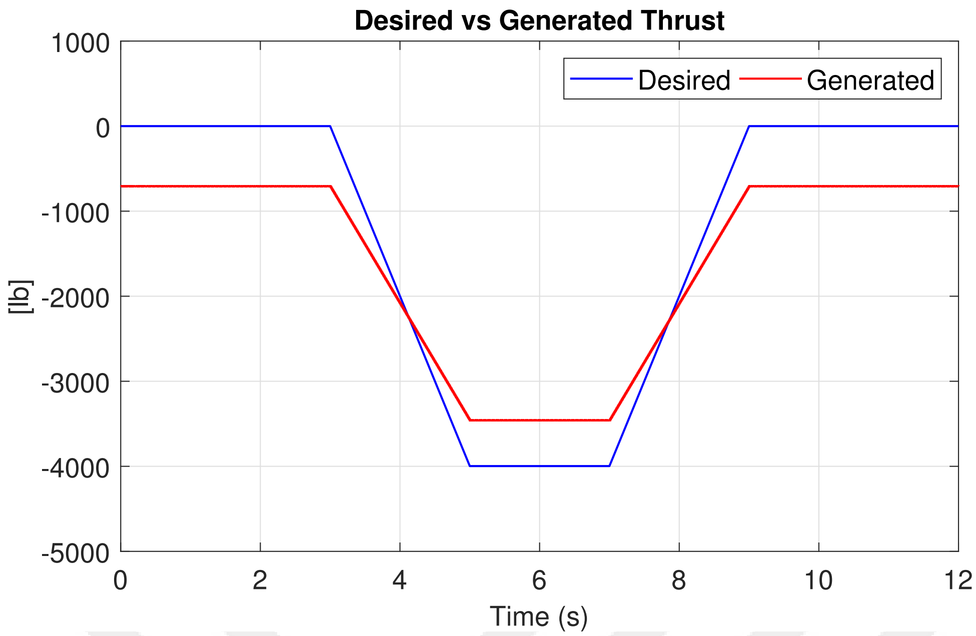

Figure A.4: Desired thrust generation plot

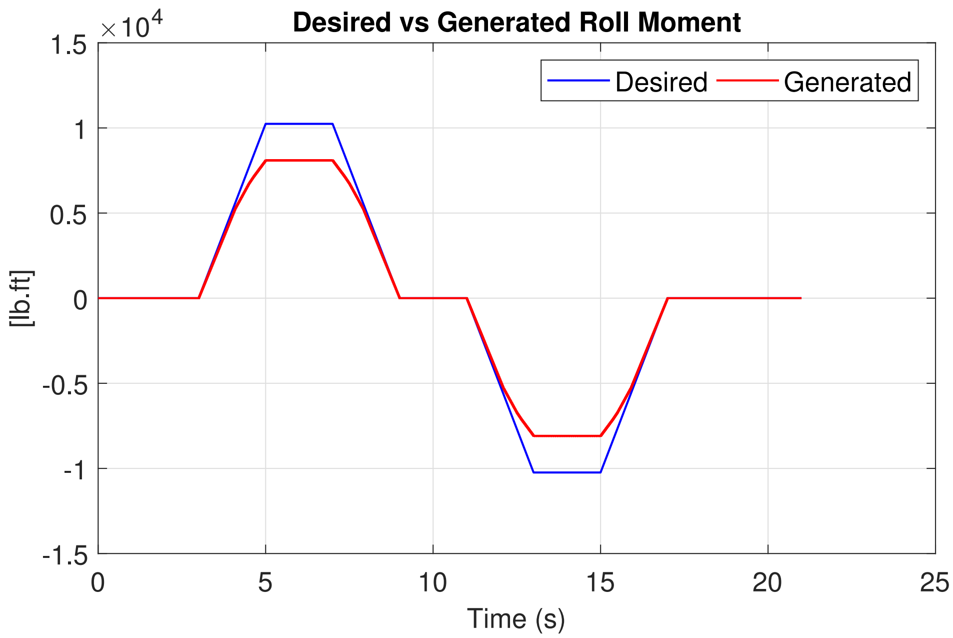

Figure A.5: Desired roll moment generation plot

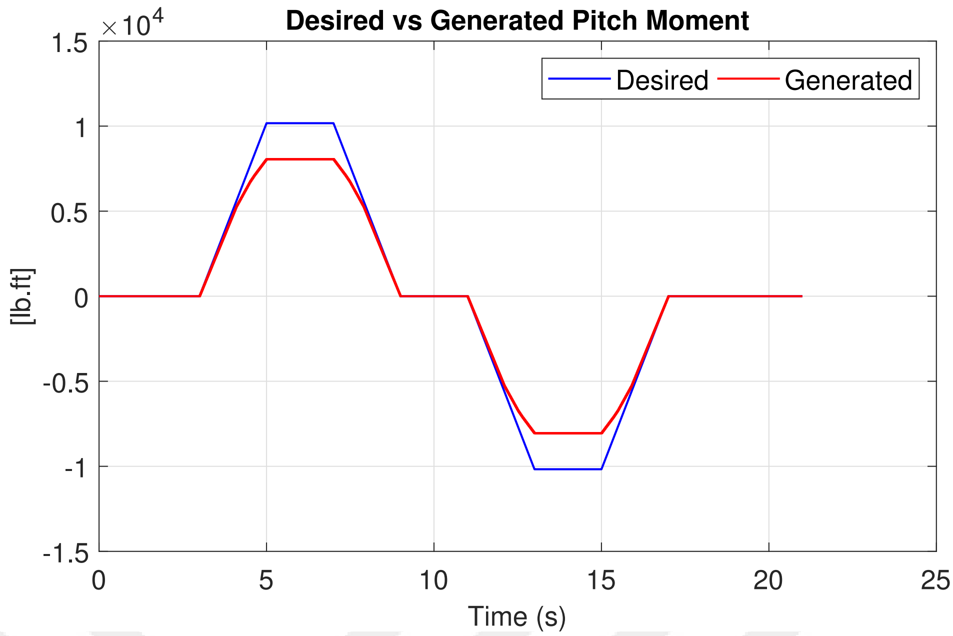

Figure A.6: Desired pitch moment generation plot

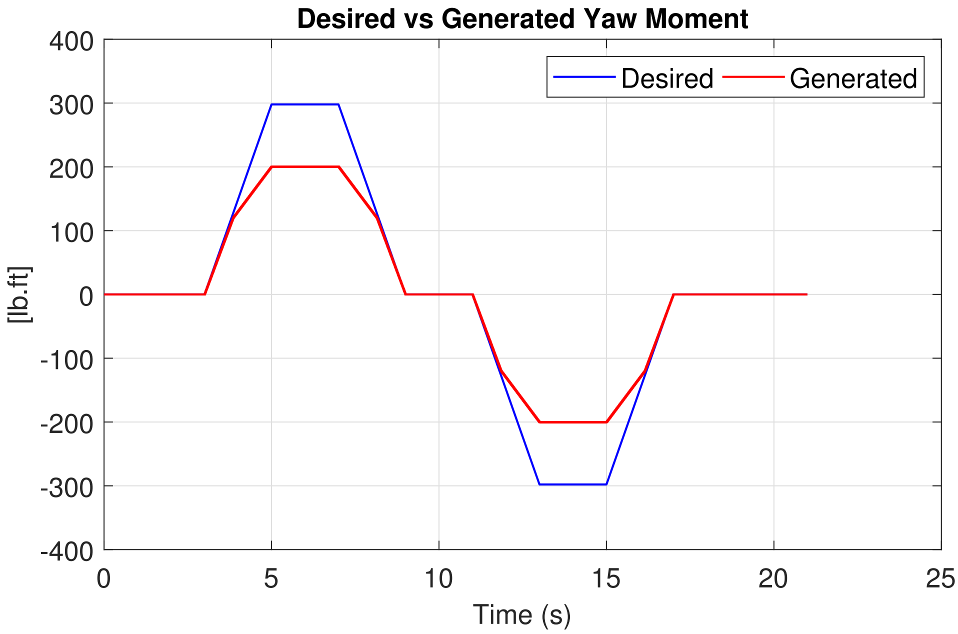

Figure A.7: Desired yaw moment generation plot

From the figures, it can be seen that the desired values are almost satisfied by the Blended-Inverse solution.

The other weight matrix "$Q \in \Re^{20\times20}$" mostly affects the manoeuvrability of the aircraft with pilot controls. Then, it is selected by subjectively flying the aircraft in the simulation environment (see Chapter-3). The final form of the matrix "Q" is selected as a diagonal matrix such that its all diagonal elements consist of "0.01".

$$Q = \begin{bmatrix} 0.01 & 0 & 0 & \cdots & 0 \\ 0 & 0.01 & 0 & \cdots & 0 \\ 0 & 0 & 0.01 & \cdots & 0 \\ \vdots & \vdots & \vdots & \ddots & \vdots \\ 0 & 0 & 0 & 0 & 0.01 \end{bmatrix} \in \Re^{20\times20}$$

A.7 Controller Model Gains

Two sets of controller gains are used with the same structure in Figs. 3.10 and 3.11. One gain set is for the trimmer, and the other set is for conducting simulation tests. Both sets are listed in the following sections.

A.7.1 Vertical Channel

	Trimmer	**Flight Test**
Proportional	0.005	0.003
Integral	0.0005	0.0003
Derivative	0	0.001

Table A.25: PID controller gains of vertical channel

A.7.2 Longitudinal Channel

	Trimmer	**Flight Test**
Proportional	1	1.5
Integral	0.1	0.1

Table A.26: PI gains for generating reference pitch angle

	Trimmer	**Flight Test**
Proportional	0.05	0.075
Integral	0.005	0.005
Derivative	0.1	0.05

Table A.27: PID controller gains of pitch channel

A.7.3 Lateral Channel

	Trimmer	**Flight Test**
Proportional	1	1.3
Integral	0.1	0.1

Table A.28: PI gains for generating reference roll angle

	Trimmer	**Flight Test**
Proportional	0.05	0.05
Integral	0.005	0.001
Derivative	0.1	0.02

Table A.29: PID controller gains of roll channel

A.7.4 Yaw Channel

	Trimmer	**Flight Test**
Proportional	0.05	0.4
Integral	0.005	0.04
Derivative	0.1	0.1

Table A.30: PID controller gains of yaw channel

	Trimmer	**Flight Test**
Proportional	-	0.25
Integral	-	0.05

Table A.31: PI controller gains of turn coordinator

In Table A.31, trimmer gains are not defined because all trim points used in this study are in wings-level condition. Then, turn coordinator is not used in trimming the aircraft. Instead, it is always trimmed to reference heading angle.